

INFORMATION TO USERS

This manuscript has been reproduced from the microfilm master. UMI films the text directly from the original or copy submitted. Thus, some thesis and dissertation copies are in typewriter face, while others may be from any type of computer printer.

The quality of this reproduction is dependent upon the quality of the copy submitted. Broken or indistinct print, colored or poor quality illustrations and photographs, print bleedthrough, substandard margins, and improper alignment can adversely affect reproduction.

In the unlikely event that the author did not send UMI a complete manuscript and there are missing pages, these will be noted. Also, if unauthorized copyright material had to be removed, a note will indicate the deletion.

Oversize materials (e.g., maps, drawings, charts) are reproduced by sectioning the original, beginning at the upper left-hand corner and continuing from left to right in equal sections with small overlaps.

ProQuest Information and Learning
300 North Zeeb Road, Ann Arbor, MI 48106-1346 USA
800-521-0600

UMI[®]

Wing flexibility and design for animal flight

Stacey A. Combes

**A dissertation submitted in partial fulfillment of the
requirements for the degree of**

Doctor of Philosophy

University of Washington

2002

Program Authorized to Offer Degree: Zoology

UMI Number: 3062932

**Copyright 2002 by
Combes, Stacey Anne**

All rights reserved.

UMI[®]

UMI Microform 3062932

**Copyright 2002 by ProQuest Information and Learning Company.
All rights reserved. This microform edition is protected against
unauthorized copying under Title 17, United States Code.**

**ProQuest Information and Learning Company
300 North Zeeb Road
P.O. Box 1346
Ann Arbor, MI 48106-1346**

**©Copyright 2002
Stacey A. Combes**

In presenting this dissertation in partial fulfillment of the requirements for the Doctoral Degree at the University of Washington, I agree that the Library shall make its copies freely available for inspection. I further agree that extensive copying of the dissertation is allowable only for scholarly purposes, consistent with "fair use" as prescribed in the U.S. Copyright Law. Requests for copying or reproduction of this dissertation may be referred to ProQuest Information and Learning, 300 North Zeeb Road, Ann Arbor, MI 48106-1346, to whom the author has granted "the right to reproduce and sell (a) copies of the manuscript in microform and/or (b) printed copies of the manuscript made from microform."

Signature: Stacy Combes

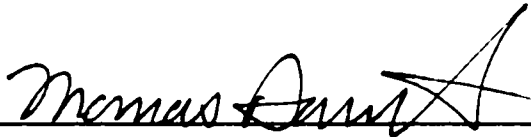
Date: July 12, 2002

University of Washington
Graduate School

This is to certify that I have examined this copy of a doctoral dissertation by
Stacey A. Combes

and have found that it is complete and satisfactory in all respects,
and that any and all revisions required by the final
examining committee have been made.

Chair of Supervisory Committee:

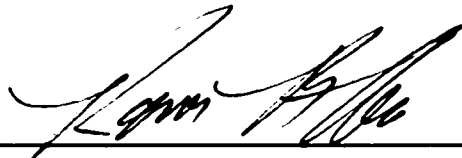


Thomas L. Daniel


Reading Committee:



Thomas L. Daniel



Raymond B. Huey



Daniel Grünbaum

Date: July 12, 2002

University of Washington

Abstract

Wing flexibility and design for animal flight

Stacey A. Combes

**Chair of the Supervisory Committee:
Professor Thomas L. Daniel
Zoology**

The wings of flying animals change shape dramatically during flight, yet the control and effects of these shape changes have received little attention. In Chapter 1, I discuss the potential effects of wing flexibility and dynamic shape changes in flying vertebrates (who can actively control wing shape) and in insects (whose wings deform passively).

In Chapter 2 (Combes and Daniel, 2001), we use an unsteady potential flow analysis to explore how unsteady motion and wing flexion affect flight performance. We compare our model predictions to aquatic flight in the ratfish *Hydrolagus colliei*, and assess the performance of various wing shapes. We find that wing flexibility increases efficiency and interacts with flapping frequency and wing shape to generate local performance optima.

In Chapter 3, I explore how insect wing architecture contributes to the control of wing deformations by measuring flexural stiffness (which incorporates both material and structural features) and quantifying patterns of supporting veins in 16 insect species. I find that average spanwise and chordwise stiffness scale strongly with wing size, and that spanwise stiffness is significantly larger than chordwise stiffness. Independent contrasts

of stiffness residuals are uncorrelated with contrasts of wing venation traits, but a finite element model of a wing reveals that leading edge veins may generate the spanwise-chordwise anisotropy measured in real wings.

In Chapter 4, I estimate spatial variation in flexural stiffness in the wings of a hawkmoth (*Manduca sexta*) and a dragonfly (*Aeshna multicolor*). In both species, stiffness declines sharply (approximately exponentially) from wing base to tip and from the leading to the trailing edge. Finite element models suggest that this pattern of stiffness transfers bending to the edges of the wing.

In Chapter 5, I explore the relative contributions of fluid-dynamic and inertial-elastic forces to passive wing deformations by comparing bending in fresh *Manduca* wings flapped in normal air *versus* helium (15% air density). I find that a substantial reduction in air density produces only slight changes in bending patterns, and that a simple damped finite element model may be able to predict patterns of wing deformation independent of calculations of aerodynamic force production.

TABLE OF CONTENTS

List of Figures.....	ii
List of Tables.....	v
Chapter 1: Introduction to wing flexibility and design for animal flight.....	1
Chapter 2: Shape, flapping and flexion: wing and fin design for forward flight.....	19
Chapter 3: Flexural stiffness in insect wings: Scaling of wing stiffness and the influence of wing venation.....	54
Chapter 4: Flexural stiffness in insect wings: Distribution of wing stiffness and effects on wing bending.....	90
Chapter 5: Contributions of inertial and aerodynamic forces to wing bending in <i>Manduca sexta</i>	139
Bibliography	164
Appendix 1: Derivation of fluid-dynamic equations for Chapter 2.....	173
Appendix 2: Derivation of wing shape equations for Chapter 2.....	176
Appendix 3: Matlab Code for Chapter 3.....	177
Appendix 4: Matlab Code for Chapter 4.....	182
Appendix 5: Matlab Code for Chapter 5.....	217

LIST OF FIGURES

<u>Figure</u>	<u>Page</u>
2.1 A-C	Kinematic variables in the potential flow analysis and measurement of variables in the ratfish, <i>Hydrolagus colliei</i> 45
2.2 A-F	Chord length distributions of theoretical wings and a ratfish pectoral fin 46
2.3 A-B	Performance of theoretical wings generated with the five shape equations <i>versus</i> the proportion of area in the outer one-fifth of the wing..... 47
2.4	Thrust and efficiency <i>versus</i> average chord length for theoretical wings with different shapes, but the same proportion of area in the outer one-fifth of the wing..... 48
2.5 A-F	Performance of theoretical wings at varying flapping frequencies..... 49
2.6 A-B	Performance of theoretical rectangular wings with varying wave speeds 50
2.7 A-D	Thrust and efficiency of a two-dimensional strip and a rectangular wing 51
3.1 A-E	Drawings of forewings from insects used in this study..... 83
3.2 A-B	Positions of force application and apparatus to measure displacement and applied force..... 84
3.3 A-F	Spanwise and chordwise flexural stiffness <i>versus</i> size measurements..... 85

3.4 A-B	Flexural stiffness <i>versus</i> span/chord length in 16 insect species.....	86
3.5	Phylogenetic tree used to calculate independent contrasts.....	87
3.6 A-B	Finite element model of a <i>Manduca sexta</i> wing and results of virtual bending experiments.....	88
4.1 A-C	<i>Manduca sexta</i> wing and calibration slide illuminated with laser lines....	123
4.2 A-D	Proposed distributions of flexural stiffness and predicted <i>versus</i> measured displacement in a <i>Manduca</i> wing.....	124
4.3 A-B	Finite element models of <i>Manduca</i> wings.....	125
4.4	Local flexural stiffness of a single <i>Manduca</i> wing subjected to repeated loads.....	126
4.5 A-D	Local flexural stiffness in wings of <i>Manduca sexta</i> and <i>Aeshna multicolor</i>	127
4.6	Comparison of local flexural stiffness in finite element model (FEM) and real <i>Manduca</i> wings.....	128
4.7 A-B	Results of static loading tests on FEM wings.....	129
4.8 A-B	Sequence of images from flapping FEM wings.....	130
4.9 A-B	Results of bending tests on a finite element model of a cambered plate..	131

4.10	Sketches of <i>Manduca sexta</i> hovering freely while feeding at an artificial flower.....	132
5.1	Apparatus used to test <i>Manduca</i> wing bending in low air density.....	157
5.2 A-E	Frames from high-speed video of a <i>Manduca</i> wing rotating at 26 Hz in low air density.....	158
5.3 A-B	Frames from high-speed video of a <i>Manduca</i> wing rotating in normal air at 26 Hz and 0.5 Hz.....	159
5.4 A-C	Spanwise bending of <i>Manduca</i> wings rotated in normal <i>versus</i> low air density.....	160
5.5 A-C	Chordwise bending of <i>Manduca</i> wings rotated in normal <i>versus</i> low air density.....	161
5.6 A-B	Wing bending in undamped and damped finite element models of a rotating <i>Manduca</i> wing.....	162

LIST OF TABLES

<u>Table</u>		<u>Page</u>
2.1	Kinematic and morphological parameters of ratfish.....	52
2.2	Model results and calculated drag of ratfish.....	53
3.1	Regressions of flexural stiffness <i>versus</i> size measurements.....	89
4.1	One sample sign test on slopes of \overline{EI} vs. strain.....	133
4.2	Morphological measurements of <i>Manduca sexta</i> and <i>Aeshna multicolor</i>	134
4.3	\overline{EI} and flexural stiffness exponents of <i>Manduca sexta</i>	135
4.4	\overline{EI} and flexural stiffness exponents of <i>Aeshna multicolor</i>	136
4.5	Mann-Whitney U-test on male <i>versus</i> female <i>Manduca sexta</i> traits.....	137
4.6	Wilcoxon signed rank test on dorsal <i>versus</i> ventral wing stiffness.....	138
5.1	Measured rotation frequency and amplitude in <i>Manduca</i> wings and brass rod control.....	163

ACKNOWLEDGEMENTS

This work would not have been possible without the generous help and support of many, many people. First and foremost, my amazing advisor Tom Daniel has been a constant source of inspiration, encouragement, bad puns and good wine. He convinced me that I was capable of much more than I thought possible, and has been a giving, selfless friend throughout my years in graduate school. I feel extremely lucky to have ended up at the University of Washington, where I drifted (like so many aimless students before me) into Tom's lab, and where the department feels more like a family than an academic unit.

I would like to thank all of the members of the Department of Zoology – from the brilliant and lively graduate students and post-docs, to the talented and essential staff, to the distinguished yet unpretentious faculty. I have truly enjoyed knowing all of you, and will miss you in the years to come. I owe a special thanks to several faculty members who have contributed substantial wisdom to this project, including Ray Huey, Danny Grünbaum, Joel Kingsolver, and John Edwards. I am also grateful to the members of the Daniel Lab for all their help, ideas, and camaraderie: my predecessors, including Brian Helmuth, Liz Stockwell, Alan Trimble, and Mark Frye, the ever-present Mike Tu, my academic twin (and great friend) Erica Goldman, and the wonderful additions of Kevin Flick, Sanjay Sane, Jordanna Henry, Jamie Theobald, and Michael Dillon.

Finally, I would like to thank my family: my Mom, Dad, sisters Candy and Cheri and brother Kevin, as well as their respective partners and offspring, who have all helped and supported me in so many ways. And last but not least, I would like to thank Doug, who has encouraged me to pursue my dreams while keeping my eyes open to the rest of the world, and whose love and support have kept me going.

DEDICATION

**For my Dad,
who taught me to always go farther,
for my Mom,
who taught me to be happy where I am,
and for Doug,
who made the whole journey worthwhile.**

Chapter 1

Introduction to wing flexibility and design for animal flight

Animal flight is a complex behavior in which animals manipulate air flowing around their wings and process enormous amounts of sensory information to control what is inherently an unstable form of locomotion. Many animals also perform complex aerial maneuvers in pursuit of prey or mates, to escape threats, or to avoid collisions. All of these behaviors involve the integration of neural control, musculoskeletal dynamics, aerodynamic and inertial forces, and the three-dimensional shape of flexible wings. A thorough understanding of animal flight requires knowledge not only of the biological processes and physical forces involved, but also of the interactions between these constituent parts.

Unfortunately, many the biological and physical processes involved in animal flight are dauntingly complex. Neural control of flight involves multiple motor pathways controlling the motions of not only the wings, but also the legs, body and head of an animal (Kammer, 1985; Arbas et al., 1997). Sensory feedback from visual, olfactory and mechanical receptors allows the nervous system to rapidly adjust these motions via muscles and skeletal elements, each of which contains its own morphological, material and dynamic complexities (i.e., Tu and Dickinson, 1994; Trimble, 2001). The motions and three-dimensional shape of flapping wings determine the details of aerodynamic force production; for rapidly flapping wings, a description of these forces is provided by a solution to the full Navier-Stokes equations (for each point in space and time), which

requires numerical methods and is computationally intensive, even for simple problems (i.e., Liu et al., 1998). Finally, the three-dimensional shape of wings (which changes continuously throughout each flight stroke) is determined by a combination of muscular, aerodynamic and inertial-elastic forces, as well as by the structure of the wing itself, including the arrangement and stiffness of supporting and deformable elements (Wootton, 1992).

Although the complexity of each system would seem to preclude a full integrative approach to animal flight, some may be more approachable than previously thought and amenable to simplifications. For example, while many flying animals collect an enormous amount of sensory information each second, certain sensory subsystems often dominate in control processes (Kammer, 1985). Insects that flap their wings up to several hundred times per second may take advantage of the dynamic properties of flight muscles to automatically regulate wing beat amplitude (thus simplifying neural control). Muscles that are stretched further (as when a wing has moved up or down a bit too far) produce more force, moving the wing back into a favorable position (Tu and Daniel, in prep). Even the extremely complex aerodynamics of hovering insect flight appear to be amenable to some simplification; recent work has shown that a revised analytical model (which is far less computationally-intensive than numerical methods) can predict temporal patterns of force production reasonably well for flapping model wings (Sane and Dickinson, 2002).

The control of three-dimensional wing shape and its effects on animal flight performance have received considerably less attention than neural, musculoskeletal and

aerodynamic aspects of flight. Yet, an understanding of dynamic wing shape is crucial to a full understanding of flight, as even simple changes in wing shape (i.e., a slight change in camber, or curvature of the wing) can have dramatic effects on force production (Batchelor, 1967). Many models of animal flight have assumed that the three-dimensional shape of wings does not change during flight, and have thus applied the rules and design principles developed for man-made flight vehicles to animals. In certain cases (such as for gliding birds), these efforts have been successful in explaining the mechanics of animal locomotion and the evolution of morphological traits (for a review, see Spedding, 1992). However, unlike airplane wings, animal wings often change shape dramatically during flight, particularly while flapping. These shape changes involve a combination of active muscular control (at the wing base in insects or throughout the wing in vertebrates) and passive deformations that are affected by flight forces and the structural and material properties of wings.

The biological materials that comprise animal wings are inherently flexible; values of Young's modulus (which describes material stiffness) are generally at least an order of magnitude less for materials such as cuticle and bone as for metals such as steel and aluminum alloys (Wainwright et al., 1982). Nevertheless, biological structures can be quite stiff, if enough material is present and that material is distributed in a way that maximizes structural rigidity (the total bending stiffness of a structure is described by its flexural stiffness (EI), the product of Young's modulus (E) and the second moment of area (I), a measure of how material is distributed in the cross-section of a structure).

However, the elements that support animal wings are often elongated and slender as compared to the same elements in non-aerial relatives (i.e. arm and finger bones of bats vs. other mammals; Kent, 1992). In addition, the diameter and thickness of supporting elements in animal wings generally decreases towards the wing tips. This design may reduce energy expenditure and stresses on the supporting elements during flapping flight by reducing mass in the distal portion of the wing (Papadimitriou et al., 1996, Wootton, 1992), but also leads to increased flexibility by reducing the local second moment of area (Wainwright et al., 1982). Wing flexibility may thus be an inevitable consequence of design constraints on flapping wings; slender wing elements that reduce mass at the tips are beneficial to flight performance, but most biological materials are not particularly stiff unless deposited in appreciable quantities.

However, wing flexibility may prove to be more than an inevitable liability in animal flight. Several studies suggest that flexibility could provide benefits in terms of aerodynamic force production, efficiency, maneuverability or control. Wu (1971) has analyzed the fluid-dynamic performance of a flexible, oscillating strip (analogous to a chordwise section of a wing, running from the leading to the trailing edge), and Daniel (1987) extended this work to find that wing bending may augment aerodynamic performance (thrust production and/or efficiency) in unsteady, flapping flight. The effects of flexibility on maneuverability have been examined in aquatic animals, for which increased body flexibility appears to increase both maneuverability (measured in terms of the space required to complete a turn; Walker, 2000) and agility (angular velocity of turns; Fish, 1999). Finally, the concept that the design of some biological

structures may provide passive control and stability (without the active intervention of the nervous system) has been demonstrated in rapid, rhythmic terrestrial locomotion (Full and Koditschek, 1999; Kubow and Full; 1999), and Sneyd et al. (1982) propose that wing flexibility may have provided analogous passive stability in gliding *Pteranodons*.

Flexibility and planform wing shape

Because animal wings are flexible, they are able to assume a variety of dynamic three-dimensional shapes that are not seen in the fixed wings of airplanes. In addition, the planform shape of animal wings (two-dimensional shape when viewed from above) varies widely in comparison to the planform shape of airplane wings. Most airplane wings are designed to have a high aspect ratio (where wings are long and skinny), as this design reduces induced drag during steady flight, allowing wings to produce more force per area and perform more efficiently than low aspect-ratio (short, blunt) wings (for a review, see Spedding, 1992).

This raises the question of why planform wing shape varies so widely in animal wings. One possibility is that because flapping flight increases the mechanical stresses on wings, very high aspect-ratio wings might be prohibited by the mechanical limits of supporting structures in the wing. In addition, these long, skinny wings may be a hindrance to animals living in complex environments (such as the forest canopy), where animals must maneuver through tight spaces. Finally, traditional aerodynamic predictions of optimal wing shape fail to account for the effects of unsteady fluid dynamics and wing flexibility on aerodynamic performance. Previous work with an

unsteady potential flow analysis that incorporates wing flexibility has suggested that unsteady effects and wing flexion may be important additional factors that affect the performance of various wing shapes (Daniel, 1987).

In Chapter 2, Daniel and I use this unsteady potential flow analysis (Wu, 1971; Daniel, 1987) to investigate the effects of wing flexibility and planform wing shape on fluid-dynamic performance, in an attempt to understand some of the factors driving variability in animal wing design (Combes and Daniel, 2000). In this model, wing flexion is specified (independent of fluid and mechanical forces) by the speed of a bending wave traveling rearward along chordwise strips of the wing. The fluid-dynamic performance of the strips is summed along the length of the wing to determine total performance in terms of thrust and fluid-dynamic efficiency.

To test the model, we examine the underwater flight of the spotted ratfish, *Hydrolagus coliei*. This animal relies entirely on flapping its large, flexible pectoral fins for routine locomotion, and generates fluid-dynamic forces by the same mechanisms as animals flying in air. In addition, the pattern of chordwise bending in the fins is measurable, allowing us to estimate wave speed and use the model to generate performance predictions. We find that the model provides a good estimate of thrust for both a juvenile and an adult ratfish.

We then used the model to assess the performance of a range of theoretical planform wing shapes under varying levels of unsteady motion and wing flexibility. We find that high aspect-ratio wings generate more thrust and perform more efficiently in some cases (as suggested by traditional aerodynamic analyses). However, when flapping

frequency is higher (motion is more unsteady) or more area is distributed to the outer portion of the wing (a feature of wing shape not described by the aspect ratio), these predictions break down. Distinct local peaks in performance appear for certain combinations of wing shape and unsteady motion, and low aspect-ratio wings sometimes perform better than high aspect-ratio wings. In addition, wing flexibility increases overall efficiency and accentuates these local performance optima, interacting with other traits (such as planform shape and flapping frequency) to generate a landscape of evolutionary pressures that could influence morphological and kinematic features in flying animals.

Passive wing bending and the design of insect wings

The results of the potential flow analysis suggest that wing flexibility and the dynamic, three-dimensional shape of wings during flight may have important effects on fluid-dynamic force production. Even in steady flight, subtle changes in the three-dimensional shape of a wing can have an enormous impact on force production. For example, increasing chordwise camber by five degrees can lead to a six-fold increase in lift production (Batchelor, 1967). The potential importance of dynamic wing shape raises the question of how animals control the bending and twisting of their wings during flight.

Flying vertebrates, such as birds and bats, can actively control many aspects of wing shape by muscular contractions that alter the alignment of wing bones, the position of feathers, or the tautness of wing membranes (Kent, 1992). The control of these subtle

movements on the timescale of a single flap involves a complex system of feedback and neural control that has not yet been thoroughly investigated.

An equally intriguing control problem is presented by flying insects, which have far less active control over the three-dimensional shape of their wings. Insect wings are largely passive structures, in which muscular forces applied at the base interact with aerodynamic and inertial forces generated by the wing's motions. The architecture of the wing (vein arrangement, three-dimensional relief, flexion lines, etc.) and the material properties of its elements determine how it will change shape in response to these forces (Wootton, 1992).

In insects, wing flexibility is critical because it enhances force asymmetry between strokes and allows wings to twist and generate force on both strokes during slow flight and hovering (Wootton, 1990a). Insects display huge variability in the arrangement and complexity of supporting veins in their wings. In fact, the arrangement of wing veins can often be used to characterize insect orders and families. Given the phylogenetic changes in the extent of cross-venation, vein thickness, and distribution of veins throughout the wing, one might expect that insect wings would display large mechanical differences that might affect how they bend during flight. Yet, our understanding of how insect wing design affects wing stiffness is limited.

In Chapter 3, I examine the effects of changes in insect wing venation on wing flexibility by measuring the flexural stiffness (EI) and venation pattern of 16 insect species from six orders. I measure overall flexural stiffness in the spanwise and chordwise direction of wings and develop methods to quantify aspects of wing venation

ranging from average vein thickness and complexity of branching to distribution of veins throughout the wing. To control for the effects of phylogeny, I calculate standardized independent contrasts (Felsenstein, 1985) of these measures and examine correlations between the contrasts to assess the functional relationship between wing venation and stiffness.

Although the species examined display enormous variability in wing venation patterns, these differences have surprisingly little effect on overall stiffness. Nearly all of the variability in measured wing stiffness is explained by wing size; spanwise stiffness scales with the cube of wing span and chordwise stiffness scales with the square of maximum chord length. Thus, the scaling of overall flexural stiffness may be an important design feature in insect wings, which has been maintained despite dramatic changes in wing venation.

All species tested also display a large spanwise-chordwise anisotropy, with spanwise stiffness one to two orders of magnitude higher than chordwise stiffness. To investigate the role of wing veins in generating this anisotropy, I created a simple finite element model of the wing of a hawkmoth, *Manduca sexta*. This computational approximation of a real wing allows me to alter design features and perform "virtual" experiments on model wings, which parallel measurements made on real wings.

Manipulations of vein stiffness in the model reveal that the presence of supporting veins, particularly along the leading edge of the wing, can generate the spanwise-chordwise anisotropy measured in real wings. As leading edge veins are present in nearly all insect wings, the observed spanwise-chordwise bending anisotropy

may be a universal trait among insects. This anisotropy would serve to strengthen the wing from bending in the spanwise direction while allowing chordwise bending to generate camber. It may also facilitate spanwise torsion, which is seen in many species during supination (Ennos, 1988; Wootton, 1981).

Distribution of wing stiffness and consequences to wing bending

The fact that overall stiffness and spanwise-chordwise anisotropy appear to be highly conserved in insect wings suggests that wings may be designed not only to minimize detrimental bending, but also to permit beneficial passive deformations during flight. Although changes in three-dimensional wing shape (i.e. camber or waves of bending) can have dramatic effects on aerodynamic force production, few models of insect flight have successfully incorporated passive wing flexibility or examined the effects of flexibility on force production.

One of the difficulties in modeling passive wing flexibility is that forces applied at the wing base lead to bending and twisting that is influenced not only by overall stiffness and gross anatomical features (i.e. flexion or fold lines), but also by the distribution of flexibility throughout the wing (Wootton, 1999). Qualitative trends in the stiffness distribution of insect wings have been noted for some time. Most wings are composed of stiffer, supporting zones near the wing base and leading edge, as well as deformable areas near the edges of the wing (Wootton, 1981), and most insect wing veins taper from base to tip (Wootton, 1992). Yet quantitative measurements of local stiffness

in insect wings are scarce, and no studies to date have demonstrated a reliable method of measuring continuous variation in the bending stiffness of intact insect wings.

In Chapter 4, I develop a method of approximating continuous variation in flexural stiffness along two axes of a wing (in the spanwise and chordwise direction) and measure spatial variation in flexural stiffness in two insects, the hawkmoth *Manduca sexta* and the dragonfly *Aeshna multicolor*. Although these species are distantly related and display large differences in wing venation pattern, I find that wing flexural stiffness declines sharply towards the edges of the wing in both species. This spatial variation can be approximated by an exponential decline in the spanwise and chordwise directions. I also find that the wings of both species behave non-linearly; average flexural stiffness increases as wings are deformed further.

To assess the consequences of the measured stiffness patterns to wing bending, I created two finite element models based on a *Manduca sexta* wing. These models simulate major features of *Manduca* wings and allow a more detailed view of three-dimensional patterns of bending than is possible with real wings. Both models are designed to reproduce the tip or trailing edge deflections measured in real *Manduca* wings subjected to a point force. However, the models differ in the spatial distribution of stiffness throughout the wing (one recreates the exponential stiffness distribution measured in real wings while the other does not). Static and dynamic tests reveal that patterns of bending in the two models differ dramatically. An exponential decline in flexural stiffness (as measured in real wings) localizes bending to the tip and trailing edge of the wing, despite the fact that bending moments are significantly higher near the

base (Ennos, 1989). This serves to maintain essential rigidity in the proximal portions of the wing and transfer bending to the distal edges, where aerodynamic force production is most sensitive to subtle alterations in shape.

Contributions of aerodynamic and inertial forces to passive wing bending

Although finite element models allow one to explore how structural and material properties of wings determine bending in response to theoretical loads, these models do not calculate fluid-dynamic forces and thus cannot predict how real wings bend during flight. Accurately predicting wing deformations during flight requires a knowledge not only of the stiffness distribution of a wing, but also of the forces that act on the wing to cause deformations.

During flight, insect wings generate (and must withstand) fluid-dynamic forces that provide the lift and thrust necessary for flight. Rapid acceleration and deceleration of wings during flapping flight also generates inertial forces related to both the mass of the wings (inertial-elastic effects) and the mass of the fluid being accelerated by the wings (virtual mass effects; see Ellington, 1984d). Fluid-related forces can produce noticeable bending in wings (i.e. bending in the wing tips of gliding birds and airplanes), and have been assumed to be important in producing bending and torsion in flapping insect wings (for example, Ennos, 1988; Ennos and Wootton, 1989). Predicting passive shape changes in insect wings due to fluid forces involves solving a coupled aeroelastic problem; if aerodynamic forces at any given time in the flight stroke cause the wing to change shape, this new shape must be used to calculate the aerodynamic forces in the

next time step, which lead to further shape changes, and so on. In contrast, shape changes caused by the inertia of flapping wings themselves (inertial-elastic effects) could be predicted from the kinematics, mass distribution and stiffness distribution of the wing, prior to calculations of aerodynamic force production.

A variety of theoretical approaches suggest that the inertial-elastic forces produced by flapping wings are at least as large as the fluid-dynamic forces generated by these motions (Ennos, 1988; Ennos, 1989; Daniel and Combes,). Nevertheless, we still do not have a basic understanding of how the mass of a wing and the fluid it moves through contribute to the patterns of bending observed in insect wings. In Chapter 5, I use an experimental approach to examine the relative contributions of inertial-elastic and fluid-dynamic forces to wing bending. I attach fresh *Manduca sexta* wings to an oscillator inside a chamber, rotate them at realistic flight frequencies and amplitudes, and compare bending patterns of wings rotating in normal air *versus* helium (approximately 15% air density); the lower density of helium should substantially reduce the contribution of fluid-dynamic forces to the observed wing deformations.

I find that the overall motions and extent of bending in *Manduca* wings are similar in both normal and low air density, with the exception of higher-frequency components of motion that appear in the wings rotating in helium. A simplified finite element model of a *Manduca* wing (which simulates the measured flexural stiffness distribution, see above) rotated in the same way as real wings produces similar patterns of bending; high-frequency motions are apparent in the model initially, but these motions

disappear when damping is added to the model. These results suggest that fluid damping alone may explain the bending differences seen in real wings.

The overall similarity in *Manduca* wing trajectory and bending magnitude despite an 85% decrease in fluid density indicates that the contribution of aeroelasticity to wing deformations in flying insects may be relatively minor compared to the contribution of inertial-elastic effects. This suggests that developing an integrative model of insect flight that incorporates passive wing flexibility may be easier than previously thought. Given that overall flexural stiffness scales with wing size (Chapter 3) and declines sharply towards the tip and trailing edge of wings (Chapter 4), measurements of mass distribution in a wing should allow one to make a reasonable prediction of the patterns and magnitude of wing deformation during flight with a simple damped finite element model of a wing. This information could then be incorporated into a variety of models of insect flight to understand how passive wing flexibility affects flight performance.

An understanding of how the dynamic, three-dimensional shape of flapping wings contributes to flight performance will be critical in future attempts aimed at integrating the components of animal flight. Studies of wing morphology suggest that some aspects of wing motion and control may occur automatically, without the monitoring or input of the nervous system (for a review, see Wootton, 1990a). Results of this study provide further evidence of smart design; non-linear behavior in insect wings may help prevent excessive deformations, and a sharp decline in flexural stiffness towards the edges of wings may limit bending in core wing regions while enhancing bending in zones critical to aerodynamic control. The future discovery of additional

broad trends and smart-design features will facilitate an integrative view of animal flight; this view may ultimately add to our understanding of how the interplay between morphology and environment leads to diversity in animal design.

Notes to Chapter 1

- Arbas, E. A., Levine, R. B. and Strausfeld, N. J. (1997). Invertebrate nervous systems. In *Handbook of Physiology, Section 13, Comparative Physiology, vol II.* (ed. W. H. Dantzler). New York: Oxford University Press.
- Batchelor, G. K. (1967). *An introduction to fluid dynamics.* Cambridge: Cambridge University Press.
- Combes, S.A. and Daniel, T.L. (2001). Shape, flapping and flexion: Wing and fin design for forward flight. *J. Exp. Biol.* **204**(12), 2073- 2085.
- Daniel, T. L. (1987). Forward flapping flight from flexible fins. *Can J. Zool.* **66**, 630-638.
- Daniel, T. L. and Combes, S. A. (). Flexing wings and fins: bending by inertial or fluid-dynamic forces? *Amer. Zool.*
- Ennos, A. R. (1988). The importance of torsion in the design of insect wings. *J. Exp. Biol.* **140**, 137-160.
- Ennos, A. R. (1989). Inertial and aerodynamic torques on the wings of Diptera in flight. *J. Exp. Biol.* **142**, 87-95.
- Ennos, A. R. and Wootton, R. J. (1989). Functional wing morphology and aerodynamics of *Panorpa germanica* (Insecta: Mecoptera). *J. Exp. Biol.* **143**, 267-284.
- Felsenstein, J. (1985). Phylogenies and the comparative method. *Am. Nat.* **125**, 1-15.
- Fish, F. E. (1999). Performance constraints on the maneuverability of flexible and rigid biological systems. In *Eleventh International Symposium on Unmanned Untethered Submersible Technology*, pp. 394-406. Durham, NH: Autonomous Undersea Systems Institute.
- Full, R. J. and Koditschek, D. E. (1999). Templates and anchors: neuromechanical hypotheses of legged locomotion on land. *J. Exp. Biol.* **202**, 3325-3352.
- Kammer, A. E. (1985). Flying. In *Comprehensive Insect Physiology, Biochemistry and Pharmacology. Vol 5, Nervous system: structure and motor function.* (ed. G. A. Kerkut and L. I. Gilbert). Oxford: Pergamon Press.
- Kent, G. C. (1992). *Comparative anatomy of the vertebrates.* St. Louis, Missouri: Mosby-Year Book, Inc.

Kubow, T. M. and Full, R. J. (1999). The role of the mechanical system in control: a hypothesis of self-stabilization in hexapedal runners. *Phil. Trans. R. Soc. Lond. B* **354**, 849-861.

Liu, H., Ellington, C. P., Kawachi, K., Van Den Berg, C. and Willmott A. P. (1998). A computational fluid dynamic study of hawkmoth hovering. *J. Exp. Biol.* **201**, 461-477.

Papadimitriou, H. M., Swartz, S. M. and Kunz, T. H. (1996). Ontogenetic and anatomic variation in mineralization of the wing skeleton of the Mexican free-tailed bat, *Tadarida brasiliensis*. *J. Zool., Lond.* **240(3)**, 411-426.

Sane, S. P. and Dickinson, M. H. (2002). The aerodynamic effects of wing rotation and a revised quasi-steady model of flapping flight. *J. Exp. Biol.* **205**, 1087-1096.

Sneyd, A. D., Bundock, M. S. and Reid, D. (1982). Possible effects of wing flexibility on the aerodynamics of *Pteranodon*. *Am. Nat.* **120(4)**, 455-477.

Spedding, G. R. (1992). The aerodynamics of flight. In *Advances in Comparative and Environmental Physiology, Vol. 11*. (ed. R. McN. Alexander), pp. 51-111. New York: Springer-Verlag.

Trimble, A. C. (2001). Musculoskeletal control of flight in the hawkmoth *Manduca sexta*. Thesis (Ph.D.), University of Washington.

Tu, M. S. and Daniel, T. L. (in prep). Cardiac-like behavior in an insect flight muscle.

Tu, M. S. and Dickinson, M. H. (1994). Modulation of negative work output from a steering muscle of the blowfly, *Calliphora vicina*. *J. Exp. Biol.* **192**, 207-224.

Wainwright, S. A., Biggs, W. D., Currey, J. D. and Gosline, J. M. (1982). *Mechanical Design in Organisms*. Princeton, New Jersey: Princeton University Press.

Walker, J. A. (2000). Does a rigid body limit maneuverability? *J. Exp. Biol.* **203**, 3391-3396.

Wootton, R. J. (1981). Support and deformability in insect wings. *J. Zool., Lond.* **193**, 447-468.

Wootton, R. J. (1990a). The mechanical design of insect wings. *Scientific American* **Nov**, 114-120.

Wootton, R. J. (1992). Functional morphology of insect wings. *Annu. Rev. Ent.* **37**, 113-140.

Wootton, R. J. (1999). Invertebrate paraxial locomotory appendages: design, deformation and control. *J. Exp. Biol.* **202**, 3333-3345.

Wu, T. Y. (1971). Hydromechanics of swimming propulsion. Part 1. Swimming of a two dimensional flexible plate at variable forward speeds in an inviscid fluid. *J. Fluid Mech.* **46**, 337-355.

Chapter 2

Shape, flapping and flexion: wing and fin design for forward flight

S. A. Combes and T. L. Daniel

The Journal of Experimental Biology 204, 2073-2085 (2001)

Printed in Great Britain © The Company of Biologists Limited 2001

Summary

Both kinematics and morphology are critical determinants of performance in flapping flight. However, the functional consequences of changes in these traits are not yet well understood. Traditional aerodynamic studies of planform shape have suggested that high-aspect-ratio wings generate more force per area and perform more efficiently than low-aspect-ratio wings, but these analyses may neglect critical components of flapping flight such as unsteady fluid dynamics and wing or fin flexion. In this paper, we use an unsteady potential flow analysis that incorporates wing flexion to test predictions of optimal wing shape under varying degrees of unsteady motion and wing flexion. We focus on forward flapping flight and examine the effects of wing/fin morphology and movements on thrust generation and efficiency. We test the model by comparing our predictions with kinematic data derived from the aquatic flight of the ratfish *Hydrolagus colliei*. Our analyses show that aspect ratio and the proportion of area in the outer one-fifth of the wing can characterize wing shape in terms of aero- or hydrodynamic performance. By comparing the performance of wings that vary in these two parameters, we find that traditional predictions

of optimal wing shape are valid only under limited circumstances (when flapping frequency is low, wings are stiff or wings are tapered at the tips). This indicates a complex relationship between locomotor traits and performance and helps explain the diversity of wing kinematics and morphologies observed in nature.

Key words: locomotion, wing shape, flexion, unsteady effect, flapping flight, aquatic flight, swimming, ratfish, *Hydrolagus colliei*

Introduction

Swimming and flying animals generate fluid-dynamic forces by flapping flexible appendages such as wings or fins. The stresses generated by motions of these structures can be resolved into vertical forces that support an animal's weight and horizontal forces that provide thrust for forward motion. Both aerial and aquatic animals that propel themselves with wing-like appendages generate these vertical and horizontal forces. Aerial animals, which must support their weight, generate a larger net upward force than aquatic animals, which often generate vertical forces that cancel over a stroke. Despite such differences, the principles governing fluid flow around a flapping appendage remain the same. The key issues involve understanding how the motion and shape of an appendage determine the timing and magnitude of forces derived from the various fluid stresses.

These structural and kinematic traits determine the locomotor performance of flying and swimming animals. Locomotor performance can have an enormous impact on an animal's survival by providing varying levels of speed, maneuverability and endurance in

escaping from predators, capturing prey or foraging for food. The large variety of wing morphologies and kinematics observed in flying animals (both aerial and aquatic forms) suggests that no single 'optimal' combination of locomotor traits exists, but rather that different performance requirements lead to different combinations of these traits.

Attempts to explain the diversity of locomotor traits in flying and swimming animals require an understanding of the functional consequences of changes in morphology and kinematics. Two features of wing morphology that are likely to affect performance are planform wing shape and wing flexion. Both may be altered by active muscular bending and passive deformation of wings arising from inertial and fluid-dynamic loads. These traits, along with the time-dependent flow phenomena that result from the kinematics of flapping, contribute to crucial details of the flow and, thus, to the magnitude of instantaneous fluid-dynamic stresses on the wing.

Wing planform shape, in particular, has commonly been associated with locomotor performance during steady flight because of the higher induced drag associated with low-aspect-ratio wings ($\text{aspect ratio} = \text{span}^2 / \text{area}$). Low-aspect-ratio wings generally have blunter tips and, thus, may lose more circulation in this region (manifest as tip vortices). This results in a backward tilt to the force vector, or induced drag. Thus, predictions derived from steady-state aerodynamics suggest that long, thin wings (with a high aspect ratio and less induced drag) can produce more force per area and perform more efficiently than low-aspect-ratio wings (for a review, see Spedding, 1992).

These results are, at first glance, disconcerting in that they seem to suggest that selection for locomotor performance would drive wings, as well as fins that generate force

by lift-based mechanisms, to become more similar through time and eliminate the morphological variation seen in nature. This view is often countered with suggestions that low-aspect-ratio wings have, generally, a lower wing loading and thus that the mechanical stresses may be lower. Similarly, there is a notion that exceedingly high-aspect-ratio wings are prohibited by the mechanical limits of the wing and fin structures that support the animal's weight.

In addition, these steady-state predictions of optimal wing shape may change when unsteady motions such as flapping are considered. As flapping frequency increases, the magnitude of bound circulation on the wing and the forces that result from this circulation decrease (because circulation has less time to develop before stroke reversal). Alternatively, accelerational forces rise with increasing unsteadiness. Finally, while not a focus here, novel unsteady mechanisms such as clap-and-fling, leading-edge vortices, wake capture and rotational circulation (e.g. Dickinson et al., 1999; Ellington, 1995; Ellington et al., 1996) will further complicate simple analyses of wing shape.

Moreover, it is important to realize that aspect ratio provides a rather crude description of wing shape in that it reflects only the average chord length (l_{avg}) in wings of the same area. Wings with the same average chord length and total area can have that area distributed quite differently, and their aerodynamic performance can vary widely in response to that shape distribution (Ellington, 1984b).

The functional consequences of wing shape, wing flexion and unsteady motion could most easily be understood by examining changes in the pressure distribution over flapping wings during flight. In the absence of appropriate technology, however, one must

resort to a variety of alternative experimental approaches. Physical measurements of the forces generated during animal flight generally either average the forces over a wingbeat (e.g. wake analysis, Ellington, 1984e; Rayner, 1979) or sum steady forces for each time step of a flap (e.g. quasi-steady analysis, Blake, 1983a; Blake, 1983b; Blake, 1983c; Clark and Bemis, 1979; Ellington, 1984a; Pennycuick, 1972; Webb, 1973; Weis-Fogh, 1975). Other techniques such as flow visualization and simulation via physical or robotic models have been used to test theoretical analyses of flight and to suggest novel mechanisms underlying the fluid dynamics of swimming and flight (Dickinson, 1996; Dickinson et al., 1999; Ellington et al., 1996), but have not yet been used in a broad, comparative context.

Efforts are increasingly focusing on computational methods for solving the Navier–Stokes equations and calculating force production (e.g. Liu et al., 1998, and the immersed elastic boundary method of Peskin, 1995). While these approaches can validate theories of flight and suggest novel mechanisms, they are computationally intensive and thus may restrict the range of variables one can explore. For this reason, a simpler analytical model that accounts for important morphological and kinematic features is a valuable tool that can be used to identify critical features that warrant further examination.

In this paper, we investigate factors that may influence the evolution of flapping wings and fins using an unsteady potential flow analysis and measured kinematics to calculate the forces produced by a flapping wing. This analysis predicts the forces generated by pressure differences across the surface of a wing resulting from acceleration- and circulation-based phenomena. It accounts for unsteady effects such as added-mass forces and the growth of bound circulation. Because the analysis requires that fluid leave

the wing smoothly at the trailing edge (the Kutta condition), it does not predict forces derived from separated flow, attached vortices or fast rotations at stroke reversal. While the model assumes that fluid is inviscid (and therefore does not apply to animals moving at low Reynolds numbers), it is appropriate for a broad range of aerial and aquatic animals in forward, flapping flight.

A critical feature of the analysis is its inclusion of chordwise wing flexion, specified by a rearward traveling wave on the wing. In a flexing wing or fin, the peak of this wave corresponds to the highest point (maximum amplitude) in the stroke, and wave speed represents the speed at which this peak travels from the leading to the trailing edge as the wing bends at stroke reversals. In a flexible wing with no active control, wave speed will be low (because the wing bends considerably at stroke reversals), while in a stiff wing, wave speed will be high because the entire wing reaches the point of stroke reversal at nearly the same time.

Defining flexion by a traveling wave, rather than by flexural stiffness or a spring constant, allows the model to be applied not only to animals whose wings or fins bend passively as a result of inertial forces, but also to those that actively pass waves rearward on their appendages (e.g. skates; see Daniel, 1987). A similar approach has been used by Tong et al. (Tong et al., 1993) to analyze the performance of a variety of caudal fin shapes; these are quite unlike the shapes of the wings and lift-generating pectoral fins that constitute the focus of this study.

We examine underwater flight in the spotted ratfish (*Hydrolagus colliei*) to test the model. This animal relies entirely on flapping its large, flexible pectoral fins for routine

locomotion. We chose the ratfish because it affords a number of advantages. The relatively modest amplitude of fin motions and low reduced frequency at which they operate suggest that the Kutta condition is satisfied. In addition, the presence of a measurable chordwise bending pattern on the fin permits us to examine the consequences of wing deformation.

Fin flexion in the ratfish may be the result of passive and/or active processes. The muscles controlling the pectoral fin do not extend out into the fin rays, but the muscles at the fin base may fire in temporal succession (Bestor, 1993), conferring some degree of active control. Because the model we use describes wing flexion by a physically observed wave speed, it is not necessary to unravel the contributions of active and passive flexion to calculate hydrodynamic forces.

We ask three questions. (i) Can an unsteady potential flow model that incorporates wing flexion reasonably predict performance (measured in terms of power, thrust and efficiency) in forward, flapping flight? (ii) What variables can be used to classify wing shape in terms of locomotor performance? (iii) What is the relative performance of wings with different shapes under varying levels of unsteady motion and wing flexion?

Although traditional aerodynamic analyses find that high-aspect-ratio wings perform better, previous work with the unsteady potential flow analysis has suggested that unsteady effects and wing flexion may be important additional factors that affect the performance of various wing shapes (Daniel, 1987). A better understanding of how these factors interact may provide insight into the functional consequences of the diverse wing morphologies and kinematics seen in nature.

Materials and methods

Calculation of fluid forces

The motion of a flexible, flapping wing can be approximated by a three-dimensional harmonically oscillating surface (Daniel, 1987; Wu, 1971). The motion of this surface is given by the following equation for a wing centered on the origin (for a movie of the motion simulated by this equation, see <http://faculty.washington.edu/danielt/Wingmovies.html>):

$$h(x, z, t) = \xi z \{ [h_o + \varepsilon(x + 1)] \exp[i\omega(t - (x + 1)/c)] \} - [\gamma(x + 1)] \quad (2.1)$$

where the function $h(x, z, t)$ describes the instantaneous location of all points on the wing.

The wing coordinates in the spanwise (x) and chordwise (z) directions are both dimensionless ($-1 \leq x \leq 1$; $0 \leq z \leq 1$); t is time. The amplitude of the leading-edge oscillation at any given point along the span is described by h_o , and linear amplitude variation in the spanwise direction is specified by ξ . The circular frequency of wing oscillation is described by ω ($\omega = 2\pi f$, where f is the flapping frequency); i is $\sqrt{-1}$. A traveling wave of deformation moves rearward at speed c , simulating the bending that results from flapping a flexible structure such as a wing or fin. Linear amplitude variation in the chordwise direction is given by ε , and the mean angle of attack averaged over a stroke is specified by γ .

To compute the fluid forces generated by a flapping wing, we divide the wing into chordwise strips and treat each strip as a harmonically oscillating flexible plate with its motion prescribed by Equation 1. We calculate the fluid forces generated by this segment with a two-dimensional solution to Euler's equation (Daniel, 1987; Wu, 1971), and sum the strips to determine the total fluid forces (Daniel, 1987).

The harmonic motion of flapping wings underlies an important non-dimensional measure of unsteady motion, the reduced frequency parameter ($\sigma = \omega l / U$, where l is a characteristic length, e.g. half chord length, and U is the forward velocity); this parameter describes the amount of vertical oscillation relative to forward steady motion. Because the growth of circulation around the wing is time-dependent (Dickinson, 1996, Dickinson et al., 1999; Ellington, 1995; Fung, 1990), increases in the reduced frequency parameter lead to a reduction in bound circulation and a temporal lag between wing motion and force generation. At the same time, however, this increased unsteadiness generates larger accelerations and inertial forces. Thus, pressures across the wing are not related to the reduced frequency parameter in any simple way.

All these effects are absorbed into four coefficients: the coefficient of power (C_p), which describes the rate at which energy is expended to produce thrust and create vorticity in the wake, the coefficient of energy (C_E), which describes the rate of energy loss to the wake, the coefficient of thrust (C_T), which is defined as the difference between the rates of energy expenditure and energy loss ($C_p - C_E$), and an efficiency parameter (η), defined as the ratio of useful work done (thrust produced) to the power expended (C_T / C_p) (Daniel, 1987; Wu, 1971; Appendix 1).

From these dimensionless coefficients, the power expended by a chordwise strip of the wing can be calculated as:

$$P_{\text{strip},i} = \frac{1}{2} \rho C_{p,i} U^3 S_i \quad (2.2)$$

where ρ is fluid density, S_i is the area of the strip i ($S_i = 2l_i w_i$, where l_i is the half strip length and w_i is the strip width). Similarly, thrust can be calculated for each strip as:

$$T_{\text{strip},i} = \frac{1}{4} \rho C_{T,i} U^2 S_i \quad (2.3)$$

These measures for each strip of the wing, with its unique motions, chord length and area, can be summed and multiplied by 2 (to account for both wings) to give the total power and thrust generated:

$$P_{\text{total}} = 2 \sum_{i=1}^n \left(\frac{1}{4} \rho C_{P,i} U^3 S_i \right) \quad (2.4)$$

$$T_{\text{total}} = 2 \sum_{i=1}^n \left(\frac{1}{4} \rho C_{T,i} U^2 S_i \right) \quad (2.5)$$

where n = the number of strips in each wing.

The Froude efficiency of a strip (η) is defined as:

$$\eta_{\text{strip},i} = \frac{T_{\text{strip},i} U}{P_{\text{strip},i}} = \frac{C_{T,i}}{C_{P,i}} \quad (2.6)$$

and total efficiency of the wing is:

$$\eta_{\text{total}} = \frac{T_{\text{total}} U}{P_{\text{total}}} = \frac{\sum_{i=1}^n \left(\frac{1}{4} \rho C_{T,i} U^2 S_i \right) U}{\sum_{i=1}^n \left(\frac{1}{4} \rho C_{P,i} U^3 S_i \right)} \quad (2.7)$$

Ratfish kinematics and modeling

We collected spotted ratfish (*Hydrolagus colieii*; Lay and Bennett, 1839) by trawling near the San Juan Islands in Puget Sound, Washington, USA, and maintained the fish in a large, covered outdoor tank with a continuous flow of fresh sea water. We filmed the animals swimming at constant velocity in a continuous-flow flume with a working area of 97 cm x 34 cm x 36 cm. Two Hi-8 video cameras filming at 30 frames s⁻¹ recorded simultaneously the lateral view and the dorsal view, which was reflected by a mirror placed

at 45 ° to the top of the flume. We filmed at flow speeds of 0.08–0.15 ms⁻¹, speeds that induced the ratfish to swim but allowed them to maintain position in the flume.

We analyzed the kinematics of two ratfish, a large female and a juvenile, to represent the extremes in size of this species. From the lateral view, we measured fin tip amplitude, flapping frequency and wave speed (Fig. 2.1). We computed tip amplitude (H) by averaging over 21 half-strokes in a continuous sequence for the female and over six half-strokes in two sequences for the juvenile. We measured the period (τ) of a flap and calculated flapping frequency ($f=1/\tau$) in the adult female over 17 complete flaps in two sequences and in the juvenile over 2.5 flaps in one sequence.

We determined wave speed (c) by recording the total time required for a wave peak (bend) to travel from the leading edge (near the fin base) to the trailing edge and dividing this time by the length of the base. We measured wave speed only at the end of the upstroke, as this is when the wave is most visible, and calculated an average wave speed for each fish (over 17 upstrokes in two sequences for the female and four upstrokes in two sequences for the juvenile).

We analyzed chordwise amplitude change (ϵ) in the two fish by comparing the amplitude of the leading and trailing edges at several different spanwise positions (measured in four frames in the female and six frames in the juvenile). In addition, we measured the amplitude of several points on the leading edge and plotted amplitude against spanwise position to determine whether there was any significant spanwise bending.

We measured span (z_0), the total area of one pectoral fin (S_p) and chord length distribution along the span (Fig. 2.2A) in dorsal views of the female and juvenile. From

these measurements, we calculated the aspect ratio of each fish's pectoral fins. We also used span and tip amplitude to calculate the angle (Φ) subtended by the flapping fin (Fig. 2.1C).

We calibrated the measurements made from video images with a grid on the back wall of the flume, and scaled our results in each frame by the distance of the fish from this wall (as revealed by the dorsal view). To avoid edge effects, we did not analyze sequences in which the ratfish was touching the sides or bottom of the flume.

We used the measured parameters in the potential flow model described above (with 10 chordwise strips) and compared the calculated thrust with an estimate of drag on a ratfish body and fins because drag should equal thrust when an animal is swimming at constant velocity. We obtained drag coefficients for a ratfish body ($C_{D,body}=2.54$) and fin ($C_{D,fin}=0.28$) from Sullivan (Sullivan, 1979), who measured forces on submerged ratfish bodies (with fins removed) towed at a fixed velocity and drag on an isolated fin with force transducers in a steady-flow flume.

We used these coefficients to calculate the total drag on the body and both fins of swimming ratfish as:

$$D_{body} = \left(\frac{1}{2}\rho C_{D,body} U^2 S_{cs}\right) \quad (2.8)$$

$$D_{fins} = \left(\frac{1}{2}\rho C_{D,fin} U^2 S_p\right) \quad (2.9)$$

where S_{cs} is the maximum cross-sectional area of the fish's body.

We also calculated the forces produced by a flapping ratfish fin with a wave speed of 100 ms^{-1} to simulate a stiff pectoral fin. Comparing these results with the forces

produced by a fin with the measured wave speed demonstrates the effects of fin flexion on calculated force production.

Generation of theoretical wing shapes

To compare the performance of wings with different planform shapes, we generated a variety of theoretical wings with mathematical equations (see Appendix 2). We divided the wings into 30 chordwise strips and calculated fluid forces generated by the wings when flapping with identical kinematics. By conserving wing area throughout our simulations, we were able to examine changes in performance due purely to the redistribution of area.

We fixed span (as well as area) to create sets of theoretical wings that have the same aspect ratio, but vary in their chord length distribution and in their apparent shape (Fig. 2.2B–F). By using several different equations to generate the wings, we were able to examine the effects of subtle differences in wing shape on flight performance.

Wing shape parameters and relative performance of theoretical wings

Before comparing the performance of theoretical wings, we asked whether wings could be classified by general shape parameters. We focused on two shape parameters: aspect ratio and the proportion of area in the outer part of the wing. Aspect ratio provides a useful description of how long and skinny wings are on average (in wings of the same area, aspect ratio essentially describes the average chord length of the wing, l_{avg} ; average chord length increases as aspect ratio decreases), but aspect ratio does not contain any information about how area is distributed within the wing. The proportion of area in the outer part of

the wing is a simple measure of how area is distributed, but may provide valuable information; in flapping wings where the stroke amplitude increases spanwise, the outer part of the wing undergoes greater accelerations and, thus, may contribute more to unsteady force production.

To determine whether the proportion of area in the outer part of the wing is a useful shape parameter, we examined the relationship between performance (thrust and efficiency) and the amount of area in the outer part of the wing in a variety of wings with fixed area and aspect ratio. We also compared the performance of wings that have similar values of both shape parameters, but slightly different chord length distributions (because they were generated by different equations). If the two shape parameters are sufficient to describe wing shape in terms of aerodynamic performance, these wings should perform similarly. We examined the effects of aspect ratio on performance by changing aspect ratio while the proportion of area in the outer part of the wing remained fixed, and varied flapping frequency and wave speed to determine the effects of unsteady flow and wing flexion on the relative performance of wings with different planform shapes.

Results

Ratfish performance and verification of the fluid model

Both ratfish swam at the same forward velocity, and the aspect ratio and wave speed of their pectoral fins are similar (Table 2.1). The adult ratfish has a larger pectoral fin and flaps with a larger tip amplitude, but the angle subtended by the pectoral fins of the two fish is nearly identical. The juvenile flaps its fins at a higher frequency than the adult, as

predicted by mass/frequency scaling relationships noted in aerial animals. The amplitude of the leading edge increases linearly with spanwise position in both the female and the juvenile ($r^2 > 0.98$), indicating no significant spanwise bending. The amplitude of the trailing edge of the wing was the same as that of the leading edge at several positions spanwise, so chordwise amplitude change was taken to be zero. Because the movement of the leading edge and chordwise bending of the wing are symmetrical on the up- and downstrokes, the mean angle of attack over the stroke is also zero, so the ratfish do not generate any net vertical force.

The potential flow model indicates that both fish swim with approximately the same locomotor efficiency, but that the adult generates more total thrust (Table 2.2). This increased thrust may be due to the larger area of the adult's pectoral fins and to the fact that the thrust coefficient for its fins is larger (1.63 in the adult *versus* 1.18 in the juvenile). The thrust calculated using the model is comparable with predicted drag when the measured wave speeds are used, but the thrust calculated for stiff pectoral fins ($c=100 \text{ ms}^{-1}$) is considerably higher (Table 2.2). While the coefficient used to estimate fin drag was measured in steady flow (and thus may not accurately represent the drag on a flapping, bending fin), fin drag accounted for only approximately 10% of total drag. Thus, even a doubling or tripling of this coefficient will not influence the total drag significantly.

Wing shape parameters

For all wing shapes tested, flapping wings generate more thrust but are less efficient as the proportion of area in the outer part of the wing increases (Fig. 2.3). This relationship

is strongest when performance is plotted against the proportion of area in the outer one-fifth of the wing. The relationship is similar for all four average chord lengths tested, although thrust and efficiency have different asymptotes for each aspect ratio (Fig. 2.3).

Wings with different shapes but the same amount of area in the outer one-fifth of the wing generate the same amount of thrust and perform with nearly identical efficiency over a range of different average chord lengths (Fig. 2.4). Thus, aspect ratio and the proportion of area in the outer one-fifth of a wing are sufficient to describe a wing in terms of aerodynamic performance, regardless of the specific details of wing shape.

It should be noted that only wings in which the maximum chord length occurs within the inner one-third of the wing span converge onto the curves in Fig. 2.3. The performance of wings that continue to increase in chord length past this point diverges from these curves. For the present analyses, we used only wings with the maximum chord located within the inner one-third of the wing.

Relative performance of theoretical wings

High-aspect-ratio wings generate more thrust and are generally more efficient than low-aspect-ratio wings (Fig. 2.3A,B). Wings with more area distributed to the outer portion of the wing also generate more thrust, but are less efficient than wings with less area in the outer portion (Fig. 2.3A,B).

As flapping frequency rises, thrust production increases and efficiency generally decreases (Fig. 2.5), although at higher frequencies and in wings with more area at the tip, efficiency rises and falls with increasing average chord length (Fig. 2.5D,F). As a result,

low-aspect-ratio wings can perform more efficiently than some higher-aspect-ratio wings (in this case, increasing their efficiency by several per cent). In addition, low-aspect-ratio wings flapping at higher frequencies not only can produce more thrust but can also sometimes perform more efficiently than if they were flapping at lower frequencies.

Wings with high wave speeds (e.g. stiffer wings) generate more thrust (Fig. 2.6A), but are less efficient than those with lower wave speeds (Fig. 2.6B). In wings with lower wave speeds, efficiency rises and falls by several per cent with increasing average chord length, again showing that low-aspect-ratio wings can be more efficient than high-aspect-ratio wings. The locations of the efficiency peaks (e.g. the locally optimal average chord length) vary with wave speed.

Discussion

Ratfish performance and shape parameters

The potential flow analysis applied to ratfish swimming provides a good estimate of thrust and demonstrates the importance of considering wing and fin flexion in models of animal flight and swimming (because thrust production is overestimated when the fin is assumed to be stiff). Our analyses based on theoretical wing shapes show that aspect ratio and the proportion of area distributed to the outer one-fifth of the wing are sufficient to characterize wing shape in terms of performance in forward, flapping flight. Thus, aero- and hydrodynamic force generation in forward flight appear to be relatively insensitive to subtle differences in planform wing shape.

While the analyses provide insight into the effects of wing shape on flight performance, the two-dimensional assumption of the fluid-dynamic model places limitations on some of the results. Because the model is essentially a summation of two-dimensional force calculations on strips running from the leading to the trailing edge, spanwise flow is not included. Without this three-dimensional flow, the model cannot predict the effects of tip vortices, which contribute induced drag and influence overall force production. In addition, strong spanwise flow, which may occur at high flapping frequencies, would alter both the overall direction and magnitude of forces and the direction of traveling waves on the wings.

Low-aspect-ratio wings are expected to have larger tip vortices and stronger spanwise flow, so the two-dimensional assumption may become more problematic as average chord length increases (aspect ratio declines). Higher induced drag on these wings will decrease both thrust and efficiency. Including induced drag would affect the values calculated by the model, but will not change the result that multiple peaks in efficiency arise from the interaction between planform shape, unsteady motion and wing or fin flexion.

Interestingly, the impact of induced drag will depend on the reduced frequency parameter. As the reduced frequency parameter increases, bound circulation is expected to decrease because there is not enough time for bound circulation to develop fully before stroke reversal. Thus, induced drag, which is caused by the shedding of bound circulation, will have less of an effect on performance.

Similarly, the predicted values of thrust and efficiency will change when wings are flapped with a non-zero angle of attack (as in aerial flyers that need to support their weight).

However, flapping flight with a non-zero mean angle of attack still produces multiple peaks in both efficiency and the thrust coefficient (see Daniel, 1987), although the locations of these peaks may be different from those shown in the figures.

Because the model includes the Kutta condition (in which flow must leave the wing smoothly at the trailing edge), the performance of wings or fins that move with extremely high angles of attack, large amplitudes, high reduced frequency parameters or fast rotations at stroke reversal (motions causing separated flow) cannot be predicted.

Relative performance of wings

We find that thrust and efficiency generally increase in wings with lower average chord lengths (higher aspect ratios), similar to what has been predicted by traditional aerodynamics. However, when flapping frequency is higher and more area is distributed to the outer portion of the wing, efficiency rises and falls with increasing average chord length, causing these predictions to break down and suggesting that local performance optima exist.

Both higher flapping frequencies and more area in the outer one-fifth of the wing lead to an increase in the reduced frequency parameter ($\sigma = \omega l / U$) in the outer portion of the wing, a region that contributes strongly to unsteady force production. The effects of this change on thrust production and efficiency can most easily be understood by examining the non-dimensional power and thrust produced by an oscillating strip. As strip length increases (increasing σ), the non-dimensional power and thrust increase initially and then

fall into a decaying oscillation (Fig. 2.7A). Efficiency shows a similar, but complementary, pattern (Fig. 2.7B), demonstrating a trade-off between thrust and efficiency.

These oscillatory behaviors can be explained by the unsteady fluid dynamics inherent in forward, flapping flight. As wing motion becomes more unsteady (for example, as flapping frequency or chord length increases), forces arising from the inertial components of fluid motion increase, causing a rise in inertial thrust production. However, as the reduced frequency parameter increases, the time available for bound circulation to develop decreases, and at some point bound circulation will begin to fall below its full value, causing a decline in total thrust production. As the reduced frequency continues to rise, multiple waves form on the wing and further complicate force production.

While the performance of non-dimensional strips indicates a trade-off between thrust and efficiency, this relationship changes when the strips of a wing are given a finite area and summed. In even the simplest case of rectangular wings (with all strips of equal chord length), the relationship between thrust production and average chord length is not the same as the relationship between non-dimensional thrust production and strip length. While non-dimensional thrust initially rises with increasing chord length and then oscillates as chord length increases further (Fig. 2.7A), total thrust production by rectangular wings falls continuously as average chord length is increased (Fig. 2.7C).

This decrease in thrust production can be explained by the fact that, as the average chord length of the wings increases (aspect ratio decreases) with area held constant, more of the wing area is distributed near the base of the wing (because span is decreased). Parts of the wing that are closer to the base undergo smaller accelerations and produce relatively less

unsteady, inertial force. Distributing more wing area close to the base (as in low-aspect-ratio wings) therefore results in lower total force production and outweighs the non-dimensional predictions of optimal chord length. In contrast, whole-wing efficiency retains the oscillatory behavior seen in individual strips because efficiency is the ratio of thrust to power; the area terms in the power and thrust equations cancel, and efficiency is determined by the ratio of coefficients, as in the non-dimensional case (Fig. 2.7D).

The reversal of the relationship between non-dimensional thrust production and strip length when performance is summed over the whole wing changes the non-dimensional prediction of a trade-off between thrust and efficiency into the familiar result that high-aspect-ratio wings generate more thrust and are more efficient than low-aspect-ratio wings. This relationship proves to be more complex, however, in several cases. When the reduced frequency parameter is raised by increasing flapping frequency, oscillations in efficiency become more apparent, and wings with high average chord lengths (low-aspect-ratio wings) can perform more efficiently than those with lower average chord lengths. Distributing more area to the outer portion of the wing (even when average chord length remains the same) produces the same effect. In addition, flapping low-aspect-ratio wings at higher frequencies can actually increase both thrust production and efficiency in some cases.

As wave speed decreases, efficiency again rises and falls with increasing average chord length. The overriding effect of decreases in wave speed (e.g. more flexible fins) is to increase efficiency and decrease thrust. But, at lower wave speeds, the local optima in efficiency become more significant, giving some low-aspect-ratio wings a selective

advantage over higher-aspect-ratio wings. In addition, the locations of these optima (the average chord lengths that perform best) depend on the wave speed, providing a landscape of evolutionary pressures that could influence various morphological and kinematic features.

Concluding remarks

Our analysis points to several important issues that should be considered in aerodynamic models of flapping flight. First, it reinforces the growing understanding that unsteady effects must be incorporated into models of swimming and flight. Traditional aerodynamic predictions concerning the relative performance of different wing shapes were upheld in this analysis only when the flapping frequency was low or the wing had a relatively tapered tip (a small proportion of area in the outer one-fifth of the wing).

Second, the analysis demonstrates the importance of considering wing flexion in models of flight. While there may be cases where wing flexion is less important (e.g. at lower Reynolds numbers), we find that the thrust generated by a wide range of wings with differing aspect ratios and area distributions will be overestimated and the efficiency underestimated if wings are assumed to be rigid. Furthermore, unsteady effects combined with wing flexion clearly complicate efficiency calculations for flapping wings.

Most importantly, the results point to one possible source of the diversity of wing morphologies and kinematics that exist in nature. The repeated rising and falling of efficiency with increasing chord length suggests that multiple local performance optima exist that may exert subtle selective pressures on the kinematics and morphology of flying

and swimming animals. While the predicted changes in efficiency may seem small (Fig. 2.5D,F, Fig. 2.6B), an increase in efficiency of a few per cent could, in fact, be critical for animals in many different situations. For example, animals with low energy reserves or those that regularly travel long distances could gain a large selective advantage if an increase in efficiency allowed them to travel slightly further or decrease their weight by using less fuel than their competitors. In addition, the magnitude of these local optima will vary with different combinations of morphological and kinematic parameters.

The interactions between flight variables (such as wing shape, reduced frequency parameter and wing flexion) show that animals can change many different aspects of kinematics or morphology to reach local peaks in performance. Of course, these selective pressures will interact with many others, such as physical constraints on wing morphology and the interaction between appendage size and maneuverability in complex habitats, to influence the suite of characters that any given animal will display.

The potential importance of wing flexion raises the question of how animals control the bending of their wings and fins during flight. Many vertebrate flyers and swimmers control the bending and flexing of their wings or fins at least partially by muscular activity; the control of these subtle movements on the timescale of a single flap must involve a complex system of feedback and neural control.

Animals with little or no muscular control of wing or fin flexion, such as insects, present an equally interesting challenge. How do these animals control the pattern and timing of the wing deformations that affect flight performance? In animals with little muscular control of wing bending, the evolution of wing shape and the passive flexibility of

wings may be linked, and this evolution may be related to the flight style and kinematics of each animal.

Although our analyses focus on planform shape as a determinant of flight performance, the results illustrate that no single feature of flight kinematics or morphology can be studied in isolation. Planform shape, unsteady fluid effects and wing flexion interact in a complex way during flapping flight. In addition, we have not yet explored the effects of unsteady flight mechanisms involving separated flow on the evolution of wing design. However, this study suggests that there are other general patterns in the functional consequences of wing shape that may clarify the relationship between wing morphology, kinematics and flight performance.

Acknowledgements

The authors would like to thank M. Robinson, J. Jensen, B. Miller, and K. Liem for their assistance in capturing and filming the ratfish. E. Goldman and M. Tu provided helpful input on drafts of the paper. D. Grunbaum provided invaluable advice on fluid dynamics issues. This work was supported by NSF grant IBN-9511681 to T.L.D., an NSF graduate fellowship to S.A.C, a Friday Harbor Laboratories summer scholarship to S.A.C., and the John D. and Catherine T. MacArthur Foundation.

Notes to Chapter 2

- Bestor, C. J. (1993). Pectoral fin locomotion in the spotted ratfish, *Hydrolagus coliei*. *Friday Harbor Laboratories Fisheries 565 course papers*, 1-17.
- Blake, R. W. (1983a). *Fish Locomotion*. London: Cambridge University Press.
- Blake, R. W. (1983b). Hovering performance of a negatively buoyant fish. *Can. J. Zool.* **61**, 2629-2630.
- Blake, R. W. (1983c). Median and paired fin propulsion. In *Fish Biomechanics*. (ed. P. W. Webb and D. Weihs), pp. 214-217. New York: Frederick A. Praeger Inc.
- Clark, B. D. and Bemis, W. (1979). Kinematics of swimming of penguins at the Detroit Zoo. *J. Zool.* **188**, 411-428.
- Daniel, T. L. (1987). Forward flapping flight from flexible fins. *Can. J. Zool.* **66**, 630-638.
- Dickinson, M. H. (1996). Unsteady mechanisms of force generation in aquatic and aerial locomotion. *Amer. Zool.* **36**, 537-554.
- Dickinson, M. H., Lehmann, F. -O., and Sane, S. P. (1999). Wing rotation and the aerodynamic basis of insect flight. *Science* **184**, 1954-1960.
- Ellington, C. P. (1984a). The aerodynamics of hovering insect flight. Part I: The quasi-steady analysis. *Phil. Trans. R. Soc. Lond. B* **305**, 1-15.
- Ellington, C. P. (1984b). The aerodynamics of hovering insect flight. Part II: Morphological parameters. *Phil. Trans. R. Soc. Lond. B* **305**, 16-40.
- Ellington, C. P. (1984e). The aerodynamics of hovering insect flight. Part V: A vortex theory. *Phil. Trans. R. Soc. Lond. B* **305**, 115-144.
- Ellington, C. P. (1995). Unsteady aerodynamics of insect flight. In *Biological Fluid Dynamics* (ed. C. P. Ellington and T. J. Pedley), pp. 109-129. Cambridge, U.K.: The Company of Biologists Limited.
- Ellington, C. P., Van Den Berg, C., Willmott, A. P. and Thomas, A. L. R. (1996). Leading-edge vortices in insect flight. *Nature* **384**, 626-630.
- Fung, Y. C. (1990). *Biomechanics: Motion, Flow, Stress, and Growth*. New York: Springer-Verlag.

Lighthill, M. J. (1975). *Mathematical Biofluidynamics*. Philadelphia: Society for Industrial Applied Mathematics.

Liu, H., Ellington, C. P., Kawachi, K., Van Den Berg, C. and Willmott A. P. (1998). A computational fluid dynamic study of hawkmoth hovering. *J. Exp. Biol* **201**, 461-477.

Pennyquick, C. J. (1972). *Animal Flight*. London: Edward Arnold (Publishers) Ltd.

Peskin, C. S. (1995). A general method for the computer simulations of biological systems interacting with fluids. In *Biological Fluid Dynamics* (ed. C. P. Ellington and T. J. Pedley), pp. 265-275. Cambridge, U.K.: The Company of Biologists Limited.

Rayner, J. M. V. (1979). A new approach to animal flight mechanics. *J. Exp. Biol.* **80**, 17-54.

Sullivan, K. (1979). Mechanical aspects of swimming in the ratfish, *Hydrolagus colliei*. *Friday Harbor Laboratories Biomechanics (Zool. 533b) course papers*, 1-28.

Timoshenko, S., Young, D. H. and Weaver Jr., W. (1974). *Vibration Problems in Engineering*. New York: John Wiley & Sons.

Tong, B.-J., Zhuang, L.-X. and Cheng, J.-Y. (1993). The hydrodynamic analysis of fish propulsion performance and its morphological adaptation. *Sadhana* **18** (3&4), 719-728.

Webb, P. W. (1973). Kinematics of pectoral fin propulsion in *Cymatogaster aggregata*. *J. Exp. Biol.* **59**, 697-710.

Weis-Fogh, T. (1975). Flapping flight and power in birds and insects, conventional and novel mechanisms. In *Swimming and Flying in Nature*. (ed. T. Y. Wu, C. J. Brokaw and C. J. Brennen), pp. 729-762. New York: Plenum Press.

Wu, T. Y. (1971). Hydromechanics of swimming propulsion. Part 1. Swimming of a two dimensional flexible plate at variable forward speeds in an inviscid fluid. *J. Fluid Mech.* **46**, 337-355.

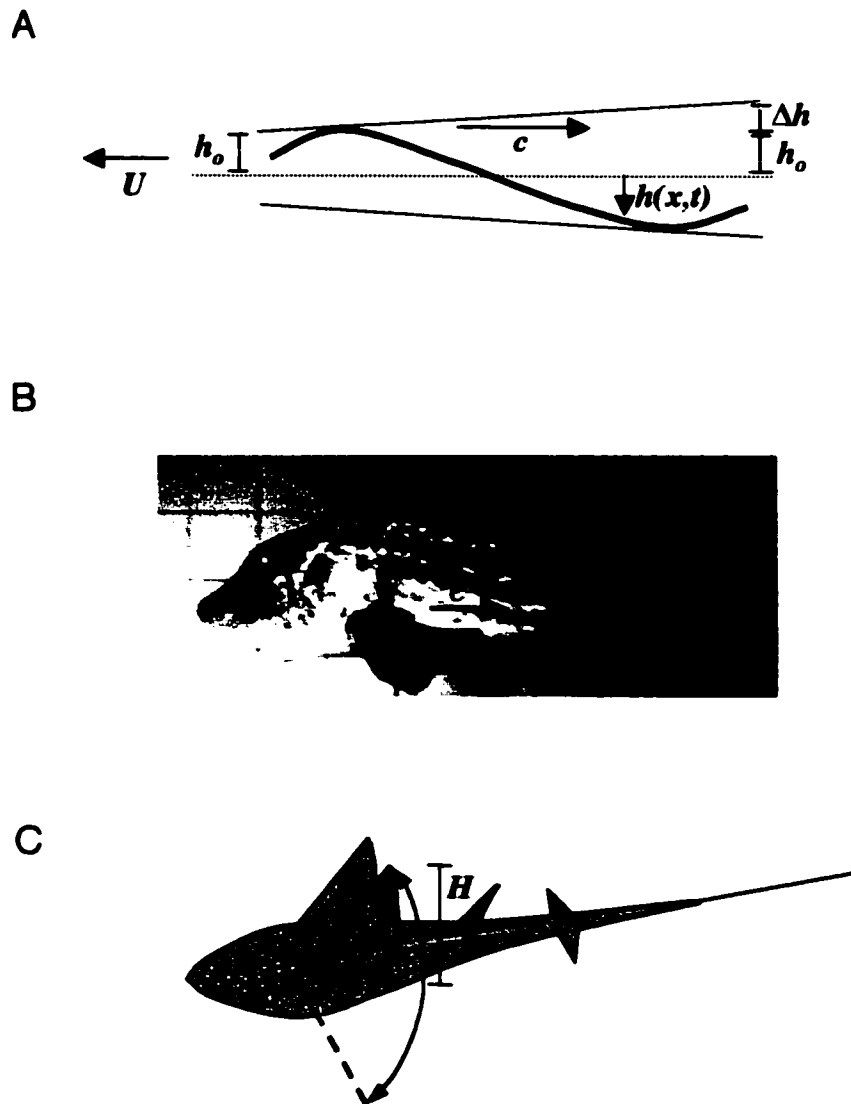


Fig. 2.1. Kinematic variables in the potential flow analysis and measurement of variables in the ratfish, *Hydrolagus coliei*. A) Two-dimensional strip oscillating with amplitude h_o and moving forward at velocity U while a wave passes rearward at velocity c . The amplitude changes from the leading to the trailing edge by a factor ϵ , the ratio of Δh to h_o . The instantaneous location of a point (x) on the strip is described by $h(x,t)$, where t is time. (B) A ratfish with a wave (highlighted) traveling backwards on its pectoral fin at wave speed c . (C) Diagram of a ratfish illustrating the angle (Φ) subtended by a flapping fin and tip amplitude (H).

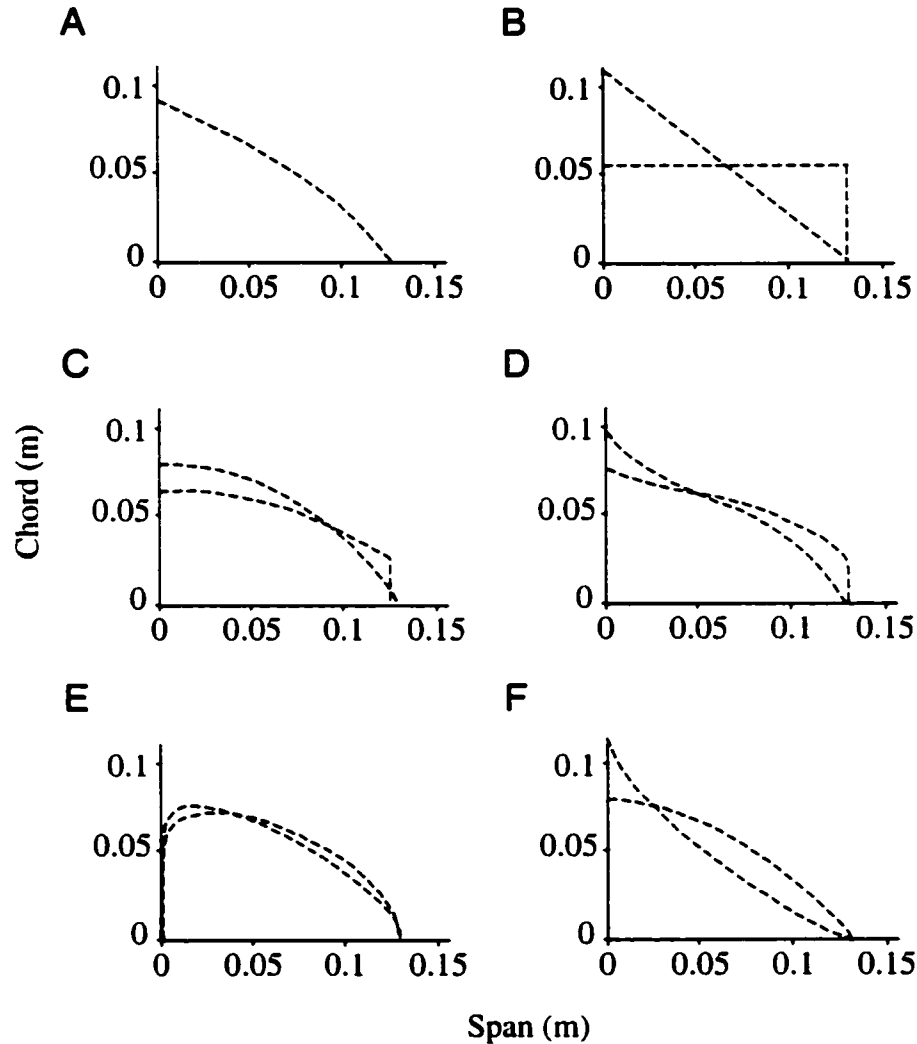


Fig. 2.2. Chord length distributions of theoretical wings and a ratfish pectoral fin. (A) Chord length distribution of the pectoral fin of the adult ratfish. Total area is 0.0069 m^2 ; aspect ratio is 2.2. (B) Sample chord length distributions generated with a 1st-degree polynomial. (C) Chord length distributions generated with a 2nd-degree polynomial. (D) Chord length distributions generated with a 3rd-degree polynomial. (E) Chord length distributions generated with a beta distribution. (F) Chord length distributions generated with an exponential function. Chord length distributions in B-F represent wings of the same aspect ratio (2.5) and area (0.0069 m^2). See Appendix 2 for mathematical equations used to generate the theoretical wings.

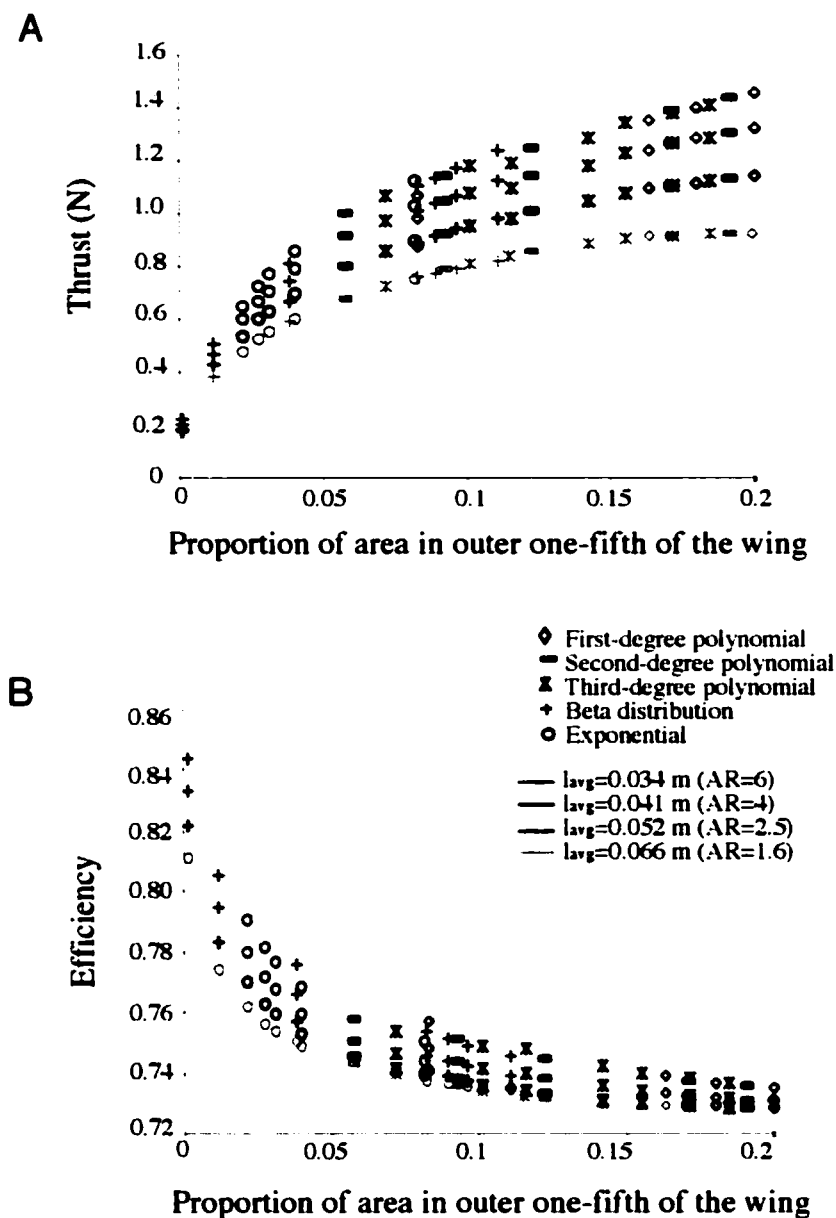


Fig. 2.3. Performance of theoretical wings generated with the five shape equations *versus* the proportion of area in the outer one-fifth of the wing. Each point represents the performance of one theoretical wing shape. The area of each wing tested is 0.0069 m^2 (multiplied by 2 to give the total performance of an animal). $U=0.15 \text{ ms}^{-1}$, $c=0.3 \text{ s}^{-1}$, $H=0.058 \text{ m}$ and $f=2.27 \text{ s}^{-1}$. Wing area was fixed, and span was adjusted to create wings with the four specified aspect ratios (AR). (A) Thrust *versus* the proportion of area in the outer one-fifth of the wing. (B) Efficiency *versus* the proportion of area in the outer one-fifth of the wing. U , velocity; c , wave speed; H , fin tip amplitude; f , flapping frequency; l_{avg} , average chord length

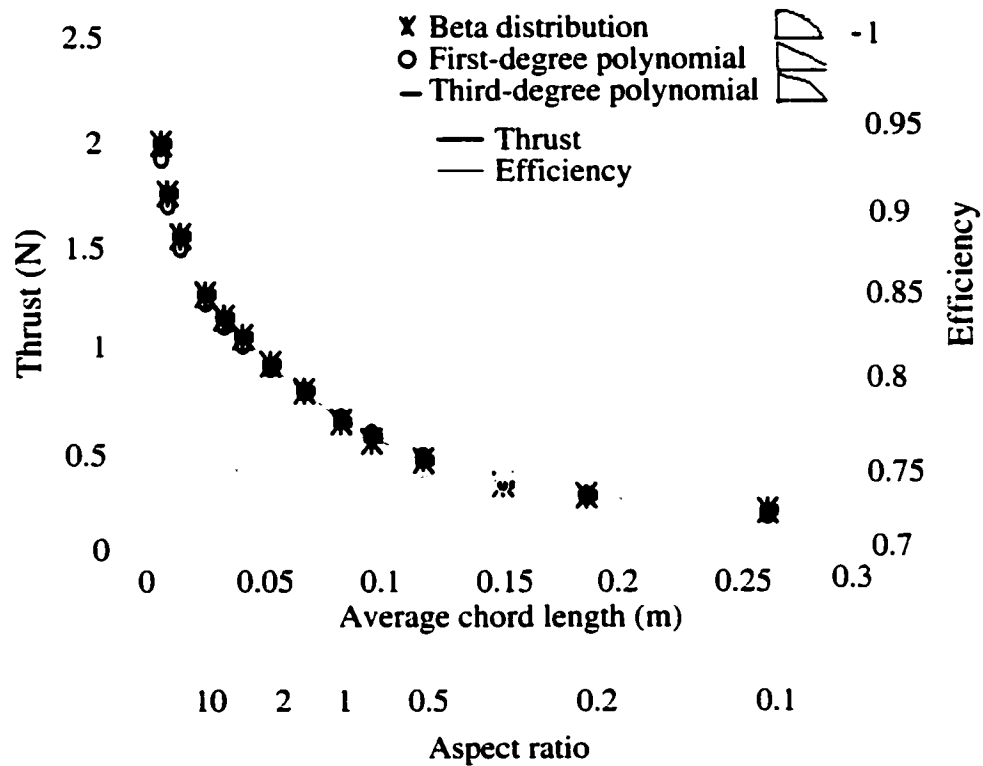


Fig. 2.4. Thrust and efficiency *versus* average chord length for theoretical wings with different shapes, but the same proportion of area in the outer one-fifth of the wing. Wings were generated with three different shape equations: a beta distribution, a first-degree polynomial and a third-degree polynomial. All wings have 9% of area in the outer one-fifth of the wing. Chord length distributions are also shown. $Sp=0.0069 \text{ m}^2$, $U=0.15 \text{ ms}^{-1}$, $c=0.3 \text{ ms}^{-1}$, $H=0.058 \text{ m}$ and $f=2.27 \text{ s}^{-1}$. Sp , total area of one pectoral fin;

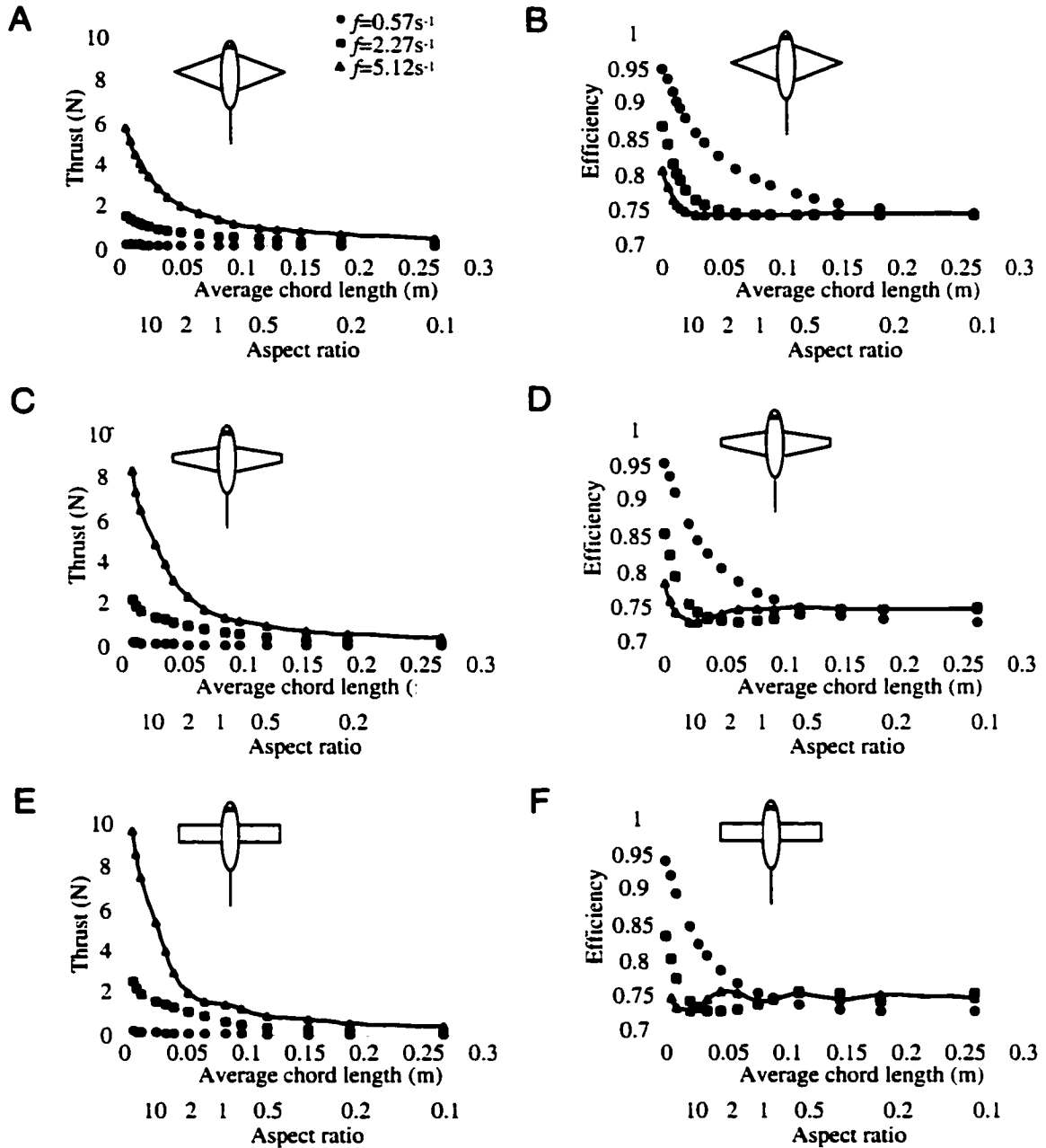


Fig. 2.5. Performance of theoretical wings at varying flapping frequencies. $Sp=0.0069$ m^2 , $U=0.15$ ms^{-1} , $c=0.3$ ms^{-1} , and $H=0.058$ m . All wings were generated with first-degree polynomials. (A,B) Thrust and efficiency *versus* average chord length for triangular wings that have 4% of the wing area in the outer one-fifth of the wing. (C,D) Thrust and efficiency *versus* average chord length for wings that have 12% of the wing area in the outer one-fifth of the wing. (E,F) Thrust and efficiency *versus* average chord length for rectangular wings that have 20% of the wing area in the outer one-fifth of the wing. Sp , total area of one pectoral fin; U , velocity; c , wave speed; H , fin tip amplitude; f , flapping frequency.

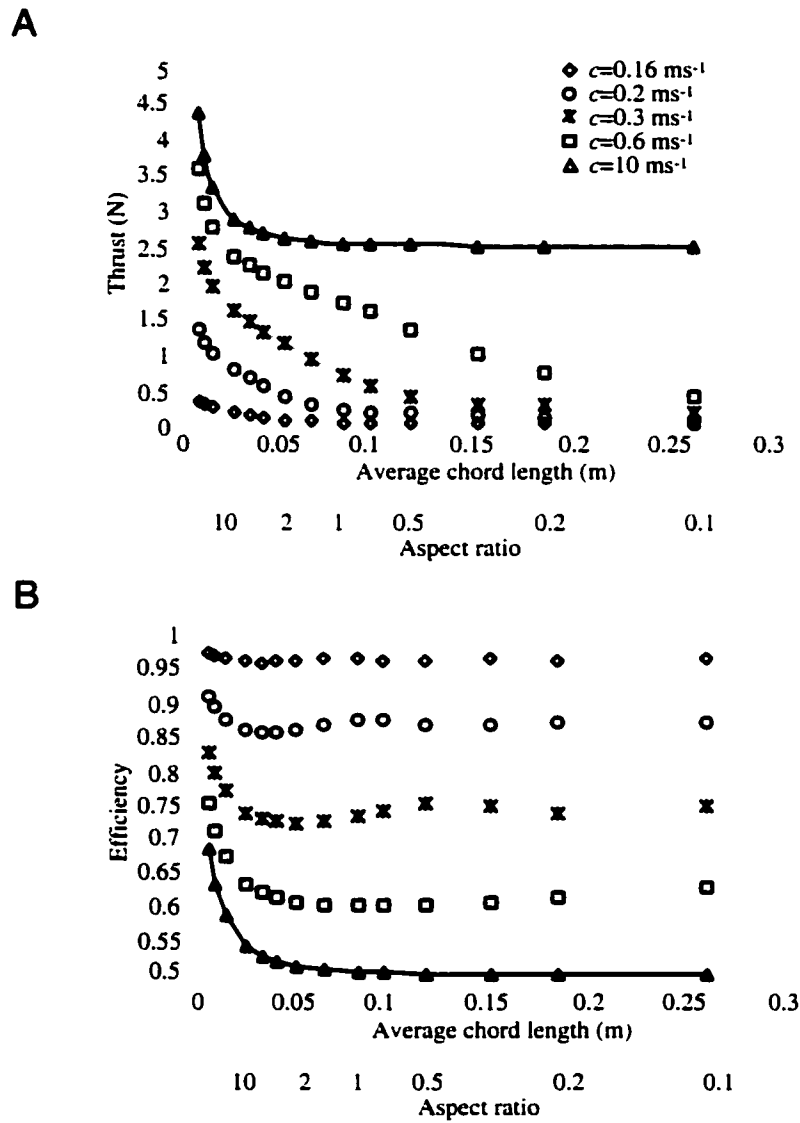


Fig. 2.6. Performance of theoretical rectangular wings with varying wave speeds. Wings were generated with a first-degree polynomial (20% of the wing area in the outer one-fifth). $Sp=0.0069 \text{ m}^2$, $U=0.15 \text{ ms}^{-1}$, $H=0.058 \text{ m}$ and $f=2.27\text{s}^{-1}$. (A) Thrust *versus* average chord length. (B) Efficiency *versus* average chord length. Sp , total area of one pectoral fin; U , velocity; c , wave speed; H , tin tip amplitude; f , flapping frequency.

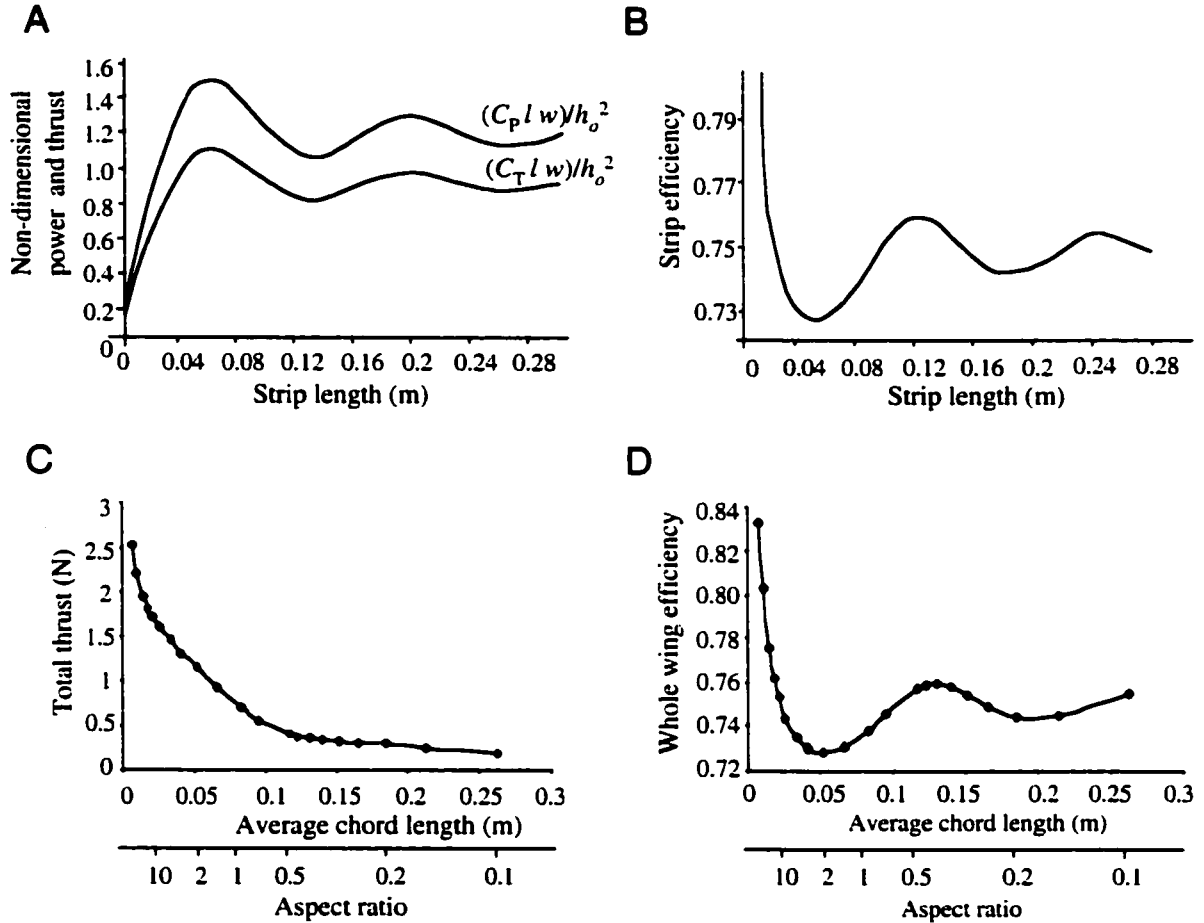


Fig. 2.7. Thrust and efficiency of a two-dimensional strip and a rectangular wing. (A) Non-dimensional power and thrust *versus* strip length. Non-dimensional power and thrust are calculated by multiplying the power or thrust coefficient by strip length and unit width ($w = 1$) and dividing by amplitude squared. (B) Efficiency *versus* strip length. (C) Total thrust produced *versus* average chord length for rectangular wings. (D) Whole-wing efficiency *versus* average chord length for rectangular wings. Each point in parts c and d represents the performance of a single wing with the given average chord length. For all graphs, $U=0.15 \text{ ms}^{-1}$, $c=0.3 \text{ ms}^{-1}$, $H=0.058 \text{ m}$ and $f=2.27\text{s}^{-1}$. U , velocity; c , wave speed; H , fin tip amplitude; f , flapping frequency; C_p , power coefficient; C_T , thrust coefficient; h_o , amplitude; l , strip length.

Table 2.1. Kinematic and morphological parameters of ratfish. Kinematic variables measured from the lateral view of a swimming ratfish include the forward velocity (U), tip amplitude (H), flapping frequency (f), and wave speed (c) (see Fig. 2.1). Chordwise amplitude change (ϵ) was measured by comparing the amplitudes of the leading and trailing edges at several points spanwise. The mean angle of attack (γ) was taken to be zero because the kinematics and bending of the fin are symmetric when averaged over a stroke. Span (z_0) and the area of one fin (S_p) were measured from the dorsal view of the ratfish and were used to calculate aspect ratio (AR). Span and tip amplitude were used to calculate the angle subtended by the fin (Φ). The cross section of the body at its widest point was assumed to be an oval, and the cross-sectional area (S_{cs}) was calculated from measurements of maximum body width (from the dorsal view) and depth (from the lateral view).

	Adult	Juvenile
Forward velocity, U (ms^{-1})	0.15	0.15
Tip amplitude, H (m)	0.058	0.033
Flapping frequency, f (s^{-1})	1.1	1.6
Wave speed, c (ms^{-1})	0.302	0.306
Chordwise amplitude change, ϵ	0	0
Mean angle of attack, γ (degrees)	0	0
Span, z_0 (m)	0.124	0.068
Angle subtended by fin, Φ (degrees)	27.1	28.1
Fin area, S_p (m^2)	0.0069	0.0022
Aspect ratio, $\text{AR}(z_0^2/S_p)$	2.2	2.1
Body cross-sectional area, S_{cs} (m^2)	0.00551	0.00157

Table 2.2. Model results and calculated drag of ratfish. The results of the fluid-dynamic model for power output, thrust and efficiency of the female and juvenile ratfish are shown together with the results when a wave speed of 100 ms^{-1} is used.

*For comparison, the calculated drag (based on measured coefficients and kinematic variables) for the body plus fins is displayed..

	Female	Juvenile
Flexible fin (measured wave speeds):		
Power (W)	0.05	0.01
Efficiency	0.77	0.78
Thrust (N)	0.26	0.06
Drag _{body + fins} (N)*	0.18	0.05
Stiff fin ($c=100 \text{ ms}^{-1}$):		
Power (W)	0.12	0.03
Efficiency	0.58	0.60
Thrust (N)	0.47	0.11
Drag _{body + fins} (N)*	0.18	0.05

Chapter 3

Flexural stiffness in insect wings:

Scaling of wing stiffness and the influence of wing venation

Summary

Insect wings deform passively during flight in response to aerodynamic and inertial forces generated by flapping. These deformations are controlled largely by the architecture of the wing (arrangement of veins, three-dimensional relief, and stiffness of veins and membrane). The pattern of supporting veins in wings varies widely among insect orders and families (Wootton, 1990a), but the functional significance of phylogenetic trends in wing venation remains unknown. Although our understanding of the functional wing morphology of a few species (i.e. dragonflies and locusts) is very good and qualitative information about wing morphology is widespread, quantitative measurements of wing stiffness for a broad range of species are lacking. This study addresses the relationship between venation pattern and wing flexibility by measuring flexural stiffness (in both the spanwise and chordwise direction) and quantifying wing venation in 16 insect species from six orders. These measurements reveal that spanwise stiffness scales strongly with the cube of wing span, whereas chordwise stiffness scales with the square of chord length. In addition, spanwise stiffness is generally 1 to 2 orders of magnitude greater than chordwise stiffness. Standardized independent contrasts of wing venation and stiffness traits reveal a significant relationship between the residuals of spanwise and chordwise stiffness (with the effects of wing size and phylogeny

removed), but venation characters are uncorrelated with wing stiffness. A finite element model of a hawkmoth wing demonstrates that leading edge veins are necessary and sufficient to generate the spanwise-chordwise anisotropy measured in real wings.

Key words: insect flight, wing flexibility, flexural stiffness, insect wing veins, independent contrasts, finite element model

Introduction

The forces produced during flight depend on both the motion of a wing and its three-dimensional shape. Whereas airplane wings are built of materials that minimize unsteady passive shape changes and allow only controlled movements, animal wings are composed of biological materials that are often inherently flexible.

Flying vertebrates, such as birds and bats, can actively control many aspects of wing shape by muscular contractions that alter the alignment of wing bones, the position of feathers, or the tautness of wing membranes. However, the elements that make up vertebrate wings are still subject to large strains (in bird bones, Biewener and Dial, 1995; in bat bones, Swartz et al., 1992; in bird feathers, Corning and Biewener, 1998) and can bend appreciably during flight.

Flying insects have far less active control over the three-dimensional shape of their wings, as insect flight muscles are restricted to the wing base. Contractions of these muscles determine the kinematics of the wing and exert some control over the angle of attack at the leading edge. In some cases, these muscles may influence the relative

positions of hinged areas of the wing (Wootton, 1992). However, insect wings are largely passive structures, in which muscular forces transmitted by the wing base interact with aerodynamic and inertial forces generated by the wing's motions. The architecture of the wing (vein arrangement, three-dimensional relief, flexion lines, etc.) and the material properties of its elements determine how the wing will change shape in response to these forces (Wootton, 1992).

In insects, wing flexibility enhances the force asymmetry between strokes that leads to thrust generation, and is necessary for wings to twist and generate force on both strokes in slow flight and hovering (Wootton, 1990a). In addition, the dramatic bending and twisting seen in many insect wings during flight (Wootton, 1990a) may affect air flow and the direction and magnitude of aerodynamic force production. The remarkable flight performance of insects suggests that their wing architecture permits beneficial passive deformations while minimizing detrimental bending, yet our understanding of how insect wing design affects flexibility is limited.

Insect wing veins act as the primary supporting structures in wings. These hollow tubes are sclerotized (or hardened), appear to contain chitin (Smith et al., 2000), and may be filled with hemolymph, although the effect of hydraulic pressure on vein stiffness is unknown (Wootton, 1981). The arrangement of veins and complexity of vein branching varies widely among insects. Venation pattern can often be used to characterize insect orders and families, and displays an overall phylogenetic trend in which large numbers of cross-veins (present in fossil wings and odonates) are lost and the main wing support shifts anteriorly in more derived species (Wootton, 1990a).

Several studies have demonstrated the functional significance of vein arrangements in insect wings. For example, the pleated, grid-like arrangement of leading edge veins in dragonfly wings helps strengthen the wing to spanwise bending (Newman and Wootton, 1986; Wootton, 1991), posteriorly-curved veins in flies generate chordwise camber when a force is applied to the wing (Ennos, 1988), and the fan-like distribution of veins in the locust hindwing causes the wing margin to bend downwards when the wing is extended (Wootton, 1995; Wootton et al., 2000; Herbert et al., 2000). However, beyond these specialized mechanisms, the functional significance of the enormous differences in overall venation pattern in insect wings (see Fig. 3.1 for a small sample of these differences) remains unclear. Given the phylogenetic changes in the extent of cross-venation, vein thickness, and distribution of veins throughout the wing, one might expect that insect wings would display large mechanical differences that affect how they bend during flight. On the other hand, differences in venation pattern may reflect alternative designs that provide insect wings with similar overall mechanical and bending properties while allowing veins to be rearranged for other reasons.

Quantitative measurements of wing stiffness that would allow us to distinguish between these hypotheses remain limited to a small number of studies in which point forces were applied to isolated wing sections (in dragonflies, Newman and Wootton, 1986; in locusts, Wootton et al., 2000), or at the center of pressure to promote torsion (in flies, Ennos, 1988; in butterflies, Wootton, 1993). Steppan (2000) measured bending stiffness in dried butterfly wings, and Smith et al. (2000) completed the first reliable measurements of material stiffness (Young's modulus) of insect wing membrane from

locust hindwings. Although each of these studies provides insight into the functional wing morphology of the insects examined, the measurements are difficult to compare in a broader context because of variations in technique.

To assess the relationship between insect wing venation and wing flexibility, this study examines the flexural stiffness (EI) and venation pattern of 16 insect species from six orders. Flexural stiffness is a composite measure of the overall bending stiffness of the wing, and reflects both the stiffness of the wing material itself (Young's modulus, E) as well as that arising from the wing's cross-sectional structure (second moment of area, I). Because insect wings bend spanwise (from wing base to wing tip) and chordwise (from leading to trailing edge) during flight, I measure flexural stiffness in both directions.

Correlations between venation pattern and wing flexural stiffness may arise either from a functional relationship between these traits or simply as a result of the shared phylogenetic history of the species studied. To remove the effects of phylogeny from this study, I calculate standardized independent contrasts (Felsenstein, 1985; Garland et al., 1999) of quantitative measures of wing venation and flexural stiffness, and examine the correlations between these contrasts to assess the relationship between wing venation and stiffness.

Finally, I construct a simplified finite element model of the wing of a hawkmoth (*Manduca sexta*) and perform numerical experiments in which I change the stiffness of various wing veins and measure the resulting flexural stiffness of the whole wing. This

modeling approach allows me to examine the functional significance of various wing veins in generating the patterns of flexural stiffness observed in real wings.

Materials and Methods

Insect collection and handling

To measure wing stiffness, I chose 16 species from six orders. I avoided insects with wings that are extensively pleated (such as the hindwings of locusts or grasshoppers), as determining how far to extend these wings for measurement was difficult. I used insects from the following orders: Odonata - two dragonfly species, *Aeshna multicolor* and *Pachydiplax longipennis*, and two damselfly species, *Lestes* spp. and *Ischnura* spp.; Isoptera - one termite species, *Zootermopsis angusticollis*; Neuroptera - one lacewing species, *Hemerobius* spp.; Hymenoptera - two wasp species, *Sceliphron* spp. and *Pepsis* spp., and one bee species, *Bombus* spp.; Diptera - four fly species from different families, *Tipula* spp., *Villa* spp., *Eristalis* spp., and *Calliphora* spp.; Lepidoptera - two butterfly species, *Ochlodes sylvanoides* and *Pieris rapae*, and one hawkmoth species, *Manduca sexta*.

I collected most insects on the University of Washington campus or adjacent Montlake Fill in Seattle, Washington between July and October 1999. *Zootermopsis angusticollis* and *Hemerobius* spp. were collected in residential areas of Seattle. I collected *Pepsis* spp. in the foothills of the Sierra Nevada mountains in central California in August 1999. *Manduca sexta* are raised in a colony at the University of Washington, and I obtained *Pieris rapae* from the Kingsolver lab at the University of Washington. I

measured spanwise and chordwise stiffness in 2-10 individuals of each species, depending on availability.

After collecting insects, I placed them in a humidified container at 4°C. Within one week of capture, I further anaesthetized an insect by placing it in the freezer for 1 to 5 minutes, recorded its weight, and removed one forewing. I measured stiffness on the forewings because all of the species tested had either larger forewings or fore- and hindwings of similar size. I then placed the insect back in the refrigerator, photographed the wing for shape measurements, and measured the stiffness of the wing (which rapidly warms to room temperature). I concluded these measurements within one hour of removing the wing from the insect (during which time the stiffness of the wing does not change appreciably, according to trials). After completing measurements on the first wing, I re-anaesthetized the insect and repeated the process for the other forewing, measuring stiffness in the opposing direction.

Wing stiffness measurements

I measured stiffness of wings by applying a point force to bend the wing in either the spanwise or chordwise direction, and using the measured force and wing displacement to calculate flexural stiffness (EI) with a simple beam equation. I glued wings to glass slides with cyanoacrylate glue and baking soda, at either the wing base (for spanwise measurements) or the leading edge (for chordwise measurements), using a minimal amount of the wing for attachment (no more than 3 mm; see Fig. 3.2A).

I fixed the slide to the left side of the apparatus shown in Figure 3.2B and adjusted the right arm so that the pin coming down from the flexible beam contacted the wing on its dorsal surface. I measured spanwise stiffness at 70% of wing span (because the pin slipped from the wing if it was placed too close to the edge) and applied the point force on or just behind the leading edge veins so that the entire wing bent in the spanwise direction, with minimal torsion (see Fig. 3.2A). I performed chordwise measurements approximately halfway between the wing base and tip, and applied the point force at 70% of the wing chord (Fig 3.2A). I lowered the right side of the apparatus with a micrometer to load the wing at four different force magnitudes, measuring force and displacement and returning to the zero (unloaded) position between each measurement (Fig 3.2B). I then flipped the slide over and repeated the measurements, loading the wing from the ventral side.

Next, I removed the slide and measured the distance from the point of attachment to the point where the force was applied to determine the effective beam length (L). I calculated EI over this distance as (Gordon, 1978):

$$EI = FL^3 / 3\delta \quad (3.1)$$

where F is applied force and δ is wing displacement. This equation provides a measure of the flexural stiffness over the entire beam length, and assumes that the beam is homogeneous (see Discussion for an analysis of this assumption). Because the equation applies only to small displacements ($\delta < 0.05 L$), I removed any measurements where the wing displacement exceeded this limit (comparing this magnitude of displacement to actual deflections experienced during flight is difficult, as measurements of wing

deflections during flight are extremely rare; see Song et al., 2001). I averaged the repeated measurements on each side into a single dorsal and a single ventral value and tested for a significant difference ($p < 0.05$) between dorsal and ventral values with a Wilcoxon signed rank test.

I plotted spanwise and chordwise stiffness against several measures of wing and body size: wing span and maximum chord length (measured in NIH Image), wing area (measured in Matlab; see below), and body mass. I also combined these measures using principal components analysis (in Statview 5.0.1) into a measure of overall size (including all four variables) and a measure of wing size (including wing span, chord and area).

To check calibrations and verify the apparatus, I measured force and displacement of a rectangular glass coverslip (a homogeneous beam of linearly elastic material, approximately the same stiffness as the largest wings measured) at three different lengths (with 3, 4, and 4.85 cm of the slide extending past the point of attachment). I then calculated EI for each length, measured the thickness and width of the coverslip, and calculated I , the second moment of area as (Gordon, 1978):

$$I = wt^3/12 \quad (3.2)$$

where w is width and t is thickness. Finally, I compared the resulting value of E , Young's modulus, with known values for glass.

Wing shape and venation measurements

From photographs of each wing, I created a black silhouette in Photoshop and then used NIH Image to measure wing span, chord, and planform area. For one wing of each species, I created a precise drawing of the wing veins using Photoshop (Fig. 3.1). In Lepidopterans, I removed the scales from the wings to visualize the veins. I counted the number of vein intersections in each wing as a measure of the complexity of vein branching. I also imported black and white images of the wing silhouette and veins into Matlab and determined the proportion of planform wing area occupied by veins (vein density) as the area of wing veins divided by the area of the silhouette (Appendix 3).

I determined average vein thickness by finding the total length of veins in the wing and dividing vein area by vein length. To calculate vein length, I used Matlab to create a skeletonized image of the veins, in which the veins are only one pixel wide. In this image matrix, vein pixels are represented by ones and non-vein pixels by zeros. I determined the total length of all veins in the wing by manipulating the image matrix; moving the matrix one pixel to the right and multiplying the original matrix by this shifted matrix cancels out any vein pixels that do not have a neighbor to their right. I took the sum of this new matrix to determine how many vein pixels have horizontal neighbors. I repeated this process for vertical neighbors by moving the original matrix down one pixel, and for diagonal neighbors by moving the matrix down and right, then down and left (Appendix 3). To determine total vein length, I multiplied the number of horizontal and vertical neighbors by the length of a pixel side, and multiplied the number of diagonal neighbors by the length of a pixel diagonal (pixel length times the square root

of 2). Finally, I divided vein area by total vein length to determine average vein thickness, and divided this by wing span to scale for overall wing size.

I measured two characteristics related to the leading edge of the wing: the proportion of veins in the leading edge and the density of veins in the leading edge. I defined the leading edge visually, by looking for a cohesive unit of veins running spanwise along the leading edge. For most species, I included all veins anterior to a particular radial vein (R in termite, R_1 in odonates, lacewing, *Villa*, and *Eristalis*, $R_{2,3}$ in *Manduca* and *Calliphora*, R_3 in *Tipula*, and R_4 in butterflies; nomenclature from Borror et al., 1989). For bees and wasps, I included the costal and subcostal veins (Borror et al., 1989) in the leading edge. I imported drawings of these leading edge veins and the silhouette of the wing area they surround into Matlab. I then calculated the proportion of veins in the leading edge as the leading edge vein area divided by total vein area, and calculated leading edge vein density as the area of leading edge veins divided by the area of the leading edge silhouette (Appendix 3).

Phylogenetic analysis of correlated characters

Because the species tested share a phylogenetic history, some characters (i.e. wing venation or stiffness) may be correlated in closely related groups simply because these species share a common ancestor that possessed these characters, and not because the characters are related in any functional way. The species used in this study cannot be treated as independent data points for statistical analysis, but the contrasts (or

differences) between traits in adjacent groups can be used, because the changes in these groups occurred independently (Felsenstein, 1985; Garland et al., 1999).

For example, the four odonate species (top four species in Fig. 3.5) cannot be treated as fully independent, but the contrast between traits in the dragonflies (*Aeshna* and *Pachydiplax*) is independent from the contrast between traits in the damselflies (*Lestes* and *Ischnura*), because these changes occurred independently. Once these contrasts are calculated, one can take the difference between these as another independent contrast. In this way, $(n-1)$ independent contrasts can be found for a trait measured in n different species. After dividing each contrast by its standard deviation, the standardized contrasts of one trait can be plotted against those of another trait to see if a relationship exists between the two when the effect of phylogeny has been removed (Felsenstein, 1985; Garland et al., 1999).

To analyze relationships between wing venation and stiffness data in a phylogenetic context, I used the Phenotypic Diversity Analysis Programs (PDAP), version 6.0, developed by Garland, Midford, Jones, Dickerman, and Diaz-Uriarte. This program originally accompanied Garland et al. (1993), and contains modifications made in Garland et al. (1999) and Garland and Ives (2000). The program allows one to construct a phylogenetic tree and enter tip values for traits; it then calculates independent contrasts and performs various diagnostics on the output.

Some aspects of the phylogenetic relationships of the pterygotes (winged insects) are under debate, and the divergence times of groups and families are far from certain. However, I constructed a phylogeny of the species used in this study by combining the

available information, and in some cases averaging or choosing midpoints between estimates of branching times (Fig. 3.5). To determine how sensitive the analysis is to branch length, I also calculated independent contrasts using arbitrary branch lengths (see Pagel, 1992), in which all internode branches are equal to one, but the tips of the tree are contemporaneous (line up with one another). I tested for correlations between contrasts in JMP 4 on a Macintosh computer.

Finite Element Modeling

To explore how wing veins contribute to the flexural stiffness of a wing, I used MSC Marc/Mentat 2001 to create a finite element model of the *Manduca* wing shown in Fig. 3.1. The model is composed of 345 thin shell elements of uniform thickness (110 μm), and mimics the planform projection of a *Manduca* wing (with no three-dimensional camber; see Chapter 4 for a discussion of the effects of wing camber on stiffness).

The model can be subjected to virtual static bending tests that mimic the tests performed on actual wings; the base is fixed with zero displacement or rotation, and a point force is applied to the wing tip (Fig. 3.6A). The model provides the tip displacement expected due to the point force (and given the material properties of the wing). I used the applied force, predicted displacement, and wing span to calculate spanwise EI for the model wing as above (Eq. 3.1). Similarly, I fixed the model wing at the leading edge and applied a point force at the trailing edge to calculate chordwise flexural stiffness.

I adjusted the Young's modulus (E), or material stiffness, of the vein elements separately from the material stiffness of the membrane elements to test the effect of the veins on overall flexural stiffness. Because the veins are flat and of the same thickness as the membrane, increasing Young's modulus mimics the increased second moment of area (I) of a tubular vein (which can be over three orders of magnitude larger than for a flat plate), as well as accounting for changes in thickness and material stiffness between wing veins and membrane.

In all simulations, I set the Young's modulus of the wing membrane at $1 \times 10^7 \text{ Nm}^{-2}$. The actual Young's modulus of *Manduca* wing membranes is unknown (the only reliable measurements of Young's modulus in insect wing membranes were performed in locust hindwings and vary widely within the wing; see Smith et al., 2000). However, for the current argument, the actual value of this parameter is less critical than the difference between vein and membrane elements. In the first set of simulations, I chose the modulus of all the vein elements to also be $1 \times 10^7 \text{ Nm}^{-2}$ (thus the wing essentially had no veins in these simulations). I then increased the modulus of the veins by orders of magnitude up to $1 \times 10^{14} \text{ Nm}^{-2}$, while membrane stiffness remained at $1 \times 10^7 \text{ Nm}^{-2}$. Finally, to test the effect of the leading edge veins alone, I increased the stiffness of just the leading edge veins (in pink, Fig. 3.5A) by orders of magnitude to $1 \times 10^{14} \text{ Nm}^{-2}$, while leaving the modulus of the membrane and the rest of the veins at $1 \times 10^7 \text{ Nm}^{-2}$.

Results

Stiffness Measurements

The glass slide has a second moment of inertia (I) of $6.75 \times 10^{-15} \text{ m}^4$. Dividing the measured values of EI by I gives a value for E of 7.3×10^{10} , 6.9×10^{10} , and $7.5 \times 10^{10} \text{ Nm}^{-2}$ for the slide at lengths of 3, 4, and 4.85 cm, respectively. These values are very close to the reported Young's modulus of ordinary glass, $7 \times 10^{10} \text{ N/m}^2$ (Gordon, 1978).

The measurements performed in this study do not reveal a significant dorsal-ventral difference in spanwise or chordwise stiffness in any species tested (Wilcoxon signed rank test, $p < 0.05$). In addition, neither side of the wing was consistently stiffer than the other. I therefore averaged dorsal and ventral measurements of EI in each direction.

The resulting flexural stiffness values are significantly correlated with all size variables; spanwise stiffness is most strongly correlated with wing span, whereas chordwise stiffness is most strongly correlated with chord length (Table 3.1, Fig. 3.3). The first principal component of overall size accounted for 89% of the variance in the traits (with loadings of 0.952, 0.952, 0.985 and 0.876 for wing span, chord, area and body mass, respectively). The first principal component of wing size accounted for 95% of the variance in wing size traits (with loadings of 0.965, 0.959 and 0.998 for wing span, chord and area, respectively). Although the correlations between flexural stiffness and these principal components measures are significant, the relationships with individual traits (spanwise stiffness/wing span and chordwise stiffness/chord length) are stronger, so I chose to use the latter relationships for further analysis.

Wing flexural stiffness of individuals within a species also appears to be related to wing size; these relationships were not tested due to small sample sizes, but are apparent in Fig. 3.4 (note that the slopes of the size regressions are similar if species averages are used instead of individuals; see Fig. 3.4). Finally, measurements of flexural stiffness reveal a large structural anisotropy in all of the insect wings tested, with spanwise flexural stiffness approximately 1 to 2 orders of magnitude greater than chordwise flexural stiffness (Fig. 3.3).

Phylogenetic Analysis of Correlated Characters

By calculating standardized independent contrasts of log-transformed spanwise stiffness, wing span, chordwise stiffness, and chord length, the effect of phylogeny can be removed from the regressions between wing stiffness and size. The relationships between the contrasts of wing stiffness and span/chord length are significant, and the slopes remain nearly the same as in the original data (span: $y = 3.04x$, $r^2 = 0.96$; chord: $y = 2.02x$, $r^2 = 0.96$). The residuals from these relationships can be used as an estimate of wing stiffness with the effect of size (and phylogeny) removed (for examples of similar uses in correcting for body size, see Garland and Janis, 1993, and Rezende et al., 2002).

Plotting these stiffness residuals against standardized independent contrasts of wing venation characters reveals no significant relationships between flexural stiffness and wing venation pattern. However, the residual of spanwise stiffness is positively correlated with the residual of chordwise stiffness ($r^2 = 0.37$, $p = 0.016$). In addition, several contrasts of vein characters are correlated with each other: as vein thickness/span

increases, the number of vein intersections (log-transformed) decreases ($r^2 = 0.28$, $p = 0.045$) and the density of veins in the leading edge increases ($r^2 = 0.64$, $p = 0.0003$). These correlated changes in wing venation are apparent visually in Fig. 3.1. When Pagei's (1992) arbitrary branch lengths are used, all relationships remains the same, with the exception of the correlation between vein thickness/span and the number of vein intersections, which is no longer significant ($r^2 = 0.06$, $p = 0.37$).

Finite Element Modeling

Virtual static bending tests on the finite element wing reveal that chordwise stiffness is higher than spanwise stiffness when membrane and vein moduli are the same (when no veins are present) (Fig. 3.6B). As the vein modulus increases, both spanwise and chordwise stiffness increase, but spanwise stiffness increases more rapidly. By the time the vein modulus is two orders of magnitude higher than the membrane modulus, spanwise stiffness has surpassed chordwise stiffness. When only the leading edge vein modulus is increased, spanwise stiffness shows an almost identical increase, while chordwise stiffness does not change appreciably from the veinless model (Fig. 3.6B).

Discussion

During flight, the wings of many insects undergo dramatic deformations, over which the insect has little active control (Wootton, 1990a). These large deformations are likely to affect flight performance, and appear to be controlled primarily by the structure of the wing, including the arrangement of supporting veins (Wootton, 1990a). Although

insect wings display enormous variation and phylogenetic trends in the arrangement of veins, this study reveals that vein arrangement has surprisingly little effect on average wing stiffness. However, all species tested display a large anisotropy between spanwise and chordwise stiffness, and stiffness in both directions scales strongly with wing size, even when the effects of phylogeny are controlled. Size scaling appears to be the dominant factor determining average flexural stiffness in insect wings; however, several factors that may underlie this trend should be considered before exploring the implications of the scaling relationships.

Scaling of Wing Stiffness

Because independent contrasts of wing size and stiffness traits were used, the observed relationships are unlikely to be the result of common ancestry. Furthermore, the constant EI measured in a glass slide at a range of lengths (Fig. 3.4) indicates that the scaling is not due to a systematic measurement error.

However, the assumption in Eq. 1 that flexural stiffness is homogeneous across a wing could potentially lead to a systematic error in the reported values. If flexural stiffness is not constant, but varies along the wing span or chord, the reported values of EI represent some weighted integration of EI along the length measured. If this integral varies systematically as beam length increases, it could account for part of the size scaling in the data.

To assess the likelihood of this explanation, I performed a numerical experiment to explore the effects of integrating various simple functions (that represent how stiffness

might vary in the wing) over increasing beam length. I proposed that the spatial pattern of stiffness in the spanwise or chordwise direction might be approximated by either a linear, exponential, or second-degree polynomial equation:

$$EI(x) = mx + b \quad (3.3)$$

$$EI(x) = c * \text{Exp}^{ax} \quad (3.4)$$

$$EI(x) = px^2 + qx + r \quad (3.5)$$

For each proposed distribution, I integrated along the beam length from the point of attachment (x_0) to the point of force application (x_{\max}):

$$\overline{EI} = \frac{1}{(x_{\max} - x_0)} \int_{x_0}^{x_{\max}} EI(x) dx \quad (3.6)$$

I explored the effect of integrating along lengths ranging from 0.001 to 0.04 m (the range of beam lengths used in calculating EI of insect wings). Over this scale of lengths, \overline{EI} increases or decreases (depending on the parameters varied), but rarely changes by more than 50%, a very small change compared to the variation in EI (over three orders of magnitude) observed in insect wings over this length scale.

The scaling of flexural stiffness has been examined previously in dried butterfly wings (Steppan, 2000) and in the primary flight feathers of birds (Worcester, 1996). Both studies found that flexural stiffness increases with size. The authors compared the observed scaling relationships with the theory of geometric similarity (see Alexander et al., 1979), where structures maintain a similar shape regardless of size, as well as with the theory of elastic similarity (see McMahon, 1973), in which loaded structures maintain a similar angular deflection regardless of size.

Neither study (Steppan, 2000; Worcester, 1996) found scaling patterns that could be explained by geometric similarity. The scaling of insect wing stiffness observed in this study appears to agree with these conclusions. The exponents of the relationship between insect wing stiffness and body mass (0.91 spanwise and 0.61 chordwise; see Table 3.1) are far from the expected value of 1.67 proposed by Worcester (1996) for geometric similarity, and the exponents of the relationship between wing stiffness and wing area (1.50 spanwise and 0.99 chordwise; see Table 3.1) are also far from the expected value of 2.0 proposed by Steppan (2000). Because the slopes are smaller than expected by geometric similarity, insect wing stiffness appears to display negative allometry. Thus larger insects have relatively more flexible wings than smaller ones, a relationship similar to that found in the primary flight feathers of birds (Worcester, 1996).

If the scaling of wing stiffness provides functional, rather than geometric similarity across a range of body sizes, displacement divided by length should remain constant, as in elastic similarity (McMahon, 1973). If we take tip displacement divided by wing span (or trailing edge displacement divided by chord length) as a rough measure of strain or curvature in the wing, we can rearrange Eq. 3.1 as:

$$\delta / L = FL^2 / EI \quad (3.7)$$

Spanwise stiffness scales approximately with L^3 and chordwise stiffness with L^2 . This suggests that in the chordwise direction, δ / L is proportional to force, regardless of the chord length of the wing. In the spanwise direction, δ / L is proportional to F / L , so spanwise curvature would be smaller in large wings for a given force.

To assess whether δ/L remains constant in flying insects over a range of sizes, we need to know how the forces on flapping insect wings scale with size. If we assume that the primary forces on an insect's wings are aerodynamic, then force is proportional to body mass. However, several studies have suggested that the inertial forces generated by flapping wings are considerably larger than the aerodynamic forces generated (Zanker and Gotz, 1990; Ennos, 1989; Daniel and Combes, in prep), and therefore inertial forces may be more important in determining wing deformations. A generalized scaling argument for inertial force in insect wings is difficult to derive because wingbeat frequency does not scale strongly with size in the insects studied here. However, smaller insects often have significantly higher wingbeat frequencies, so the ratio of inertial to aerodynamic forces on their wings may be as high or higher than in larger insects (Daniel and Combes, in prep; see Chapter 5).

Effects of wing venation on stiffness

The measurements of flexural stiffness reveal a strong spanwise-chordwise anisotropy, with spanwise stiffness 1 to 2 orders of magnitude higher than chordwise stiffness in all species tested (Fig. 3.3). Because spanwise stiffness increases as L^3 and chordwise stiffness only as L^2 , this anisotropy is generally bigger in larger-winged insects (Fig. 3.3).

The finite element model of a *Manduca* wing reveals that the basic planform geometry (or outline) of the wing would lead to similar spanwise and chordwise bending

stiffness if no veins were present (Fig 3.6B). The leading edge veins clearly play a crucial role in increasing spanwise stiffness to generate anisotropy (Fig. 3.6B).

Clustered or thickened veins in the leading edge of the wing are common in nearly all insects (see Fig. 3.1); even insects that have lost all other wing veins (such as some hymenopterans and small flies) possess a leading edge vein. This suggests that spanwise-chordwise anisotropy may be a universal trait among insects. This anisotropy would serve to strengthen the wing from bending in the spanwise direction while allowing chordwise bending to generate camber. It may also facilitate spanwise torsion, which is seen in many species during supination (Ennos, 1988; Wootton, 1981).

Although the measurements of wing venation reflect phylogenetic changes in the arrangement of veins, surprisingly none of the vein characters is correlated with the residuals of flexural stiffness. The only significant relationship between measured traits (beyond size scaling) is a correlation between the contrasts of the spanwise and chordwise stiffness residuals. This correlation indicates that some insects have wings that are generally stiffer (in both directions) than expected for their size, while others have wings that are more flexible than expected. The residuals from the original data reveal that species that are strong, versatile fliers (able to hover and fly forward at a range of speeds), such as dragonflies, *Manduca*, flies (except for the crane fly), and bumblebees, all have wings that are stiffer than expected for their size. Damselflies, crane flies, and lacewings have more flexible wings than expected, while butterflies and wasps are intermediate.

Despite this relationship between stiffness residuals, the residuals themselves are quite small. Wing size alone seems to largely determine average flexural stiffness, accounting for over 90% of the measured variability (Fig. 3.4). This scaling of overall stiffness, as well as the anisotropy between spanwise and chordwise stiffness, have persisted despite dramatic changes in wing venation, and thus may be important design features in insect wings.

The functional significance of the correlated changes in venation (such as loss of cross veins and increased vein thickness) remains unclear. Perhaps more derived groups of insects have simply evolved a venation pattern that allows them to maintain the essential scaling of wing stiffness in a more economical way (i.e., using less vein material), or perhaps the venation patterns are related to something entirely different, such as the distribution of sensory receptors on the wing (Kammer, 1985).

Alternatively, venation pattern may in fact affect wing stiffness, but in ways that could not be detected in this study. For example, venation pattern may not affect overall stiffness, but could influence how stiffness varies along the wing (see Chapter 4). In addition, the stiffness measurements in this study exclude the outer 30% of the wing, which is likely to be the most flexible region. Differences in wing stiffness between insects with veins that extend to and delineate the trailing edge (such as odonates; see Fig 3.1) and insects with primarily unsupported membrane in the trailing edge (such as hymenopterans) would most likely be found in this region.

Subtle details of vein configuration can also have dramatic effects on how insect wings function in a more dynamic context. For example, the angle at which veins branch

from the leading edge spar can affect the degree of chordwise camber generated by torsion at the leading edge of fly wings (Ennos, 1988). Thin, curved veins in the troughs of locust hindwing fans seem to be designed to buckle under strain to depress the trailing edge of the wing (Wootton, 1995; Wootton et al., 2000). And during flight, wings often bend in numerous directions at once; bending in the chordwise direction during flight, for example, would be likely to stiffen the wing in the spanwise direction beyond the static values measured in this study.

Concluding remarks

This study reveals two major findings: overall flexural stiffness is strongly correlated with wing length, and spanwise stiffness is significantly larger than chordwise stiffness. Remarkably, these patterns in wing design persist despite large changes in venation. Leading edge veins, which are present in nearly all insect wings, appear to be important in generating the observed spanwise-chordwise anisotropy.

The next step in adding to our quantitative knowledge of functional wing morphology is to determine how wing stiffness varies throughout an insect wing, and how such patterns differ between species. Armed with this more detailed information, we may come to understand how common features of insect wing design control passive deformations in flapping wings, and ultimately how these deformations interact with and affect force generation and flight performance.

Acknowledgements

I would like to thank T. Daniel for his assistance and support in all aspects of this project. R. Sugg graciously assisted in identifying the insects used in the study. D. O'Carroll, T. Morse, and J. Kingsolver provided insects, and D. Combes assisted in collecting and transporting the California spiderwasps. T. Garland provided the program for calculating independent contrasts, as well as helpful advice on its use. D. Grunbaum and R. Huey contributed useful comments on both the project and drafts of the paper. This work was supported by NSF grant 66-1822 to T. Daniel, the John D. and Catherine T. MacArthur Foundation, an NSF graduate fellowship to S. Combes, and an ARCS fellowship to S. Combes.

Notes to Chapter 3

Alexander, R. McN., Jayes, A. S., Maloiy, G. M. O., and Wathuta, E. M. (1979). Allometry of the limb bones of mammals from shrews (*Sorex*) to elephant (*Loxodonta*). *J. Zool., Lond.* **189**, 305-314.

Benton, M. J. (editor) (1993). *The Fossil Record 2*. London: Chapman & Hall, 845 pp. <http://palaeo.gly.bris.ac.uk/frwhole/FR2.html>

Biewener, A. A. and Dial, K. P. (1995). In vivo strain in the humerus of pigeons (*Columba livia*). *J. Morph.* **225**(1), 61-75.

Borror, D. J., Triplehorn, C. A., and Johnson, N. F. (1989). *An Introduction to the Study of Insects*, 6th ed. Fort Worth, TX: Harcourt Brace College Publishers.

Corning, W. R. and Biewener, A. A. (1998). In vivo strains in pigeon flight feather shafts: Implications for structural design. *J. Exp. Biol.* **201** (22), 3057-3065.

Daniel, T. L. and Combes, S. A. (in prep). Flexing wings and fins: bending by inertial or fluid-dynamic forces? *Amer. Zool.*

Ennos, A. R. (1988). The importance of torsion in the design of insect wings. *J. Exp. Biol.* **140**, 137-160.

Ennos, A. R. (1989). Inertial and aerodynamic torques on the wings of Diptera in flight. *J. Exp. Biol.* **142**, 87-95.

Felsenstein, J. (1985). Phylogenies and the comparative method. *Am. Nat.* **125**, 1-15.

Garland, T., Jr., Dickerman, A. W., Janis, C. M., and Jones, J.A. (1993). Phylogenetic analysis of covariance by computer simulation. *Syst. Biol.* **42**, 265-292.

Garland, T., Jr., Midford, P. E., and Ives, A. R. (1999). An introduction to phylogenetically based statistical methods, with a new method for confidence intervals on ancestral states. *Amer. Zool.* **39**, 374-388.

Garland, T., Jr., and Ives, A. R. (2000). Using the past to predict the present: Confidence intervals for regression equations in phylogenetic comparative methods. *Am. Nat.* **155**, 346-364.

Garland, T., Jr., and Janis, C. M. (1993). Does metatarsal/femur ratio predict maximal running speed in cursorial mammals? *J. Zool., Lond.* **229**, 133-151.

Gordon, J.E. (1978). *Structures: or Why Things Don't Fall Down*. New York: Penguin Books.

Herbert, R. C., Young, P. G., Smith, C. W., Wootton, R. J., and Evans, K. E. (2000). The hind wing of the desert locust (*Schistocerca gregaria* Forskål). III. A finite element analysis of a deployable structure. *J. Exp. Biol.* **203**, 2945-2955.

Kammer, A. E. (1985). Flying. In *Comprehensive Insect Physiology, Biochemistry and Pharmacology. Vol 5, Nervous system: structure and motor function*. (ed. G. A. Kerkut and L. I. Gilbert). Oxford: Pergamon Press.

Kristensen, N. P. (1991). Phylogeny of extant hexapods. In *The Insects of Australia: A textbook for students and research workers*, 2nd ed., Vol. 1, pp. 125-140. Ithaca, NY: Cornell University Press.

Kukalova-Peck, J. (1991). Fossil history and the evolution of hexapod structures. In *The Insects of Australia: A textbook for students and research workers*, 2nd ed., Vol. 1, pp. 141-179. Ithaca, NY: Cornell University Press.

Maddison, D. R. (1995a). Hymenoptera. In *The Tree of Life Web Project*, (ed. D. R. Maddison and K.-S. Schultz). <http://tolweb.org/tree/phylogeny.html>

Maddison, D. R. (1995b). Lepidoptera. In *The Tree of Life Web Project*, (ed. D. R. Maddison and K.-S. Schultz). <http://tolweb.org/tree/phylogeny.html>

McMahon, T. A. (1973). Size and shape in biology. *Science* **179**: 1201-1204.

Newman, D. J. S. and Wootton, R. J. (1986). An approach to the mechanics of pleating in dragonfly wings. *J. Exp. Biol.* **125**, 361-372.

Pagel, M. D. (1992). A method for the analysis of comparative data. *J. Theor. Biol.* **164**, 194-205.

Rezende, E. L., Swanson, D. L., Novoa, F. F., and Bozinovic, F. (2002). Passerines versus nonpasserines: so far, no statistical differences in the scaling of avian energetics. *J. Exp. Biol.* **205**, 101-107.

Smith, C. W., Herbert, R., Wootton, R. J., and Evans, K. E. (2000). The hind wing of the desert locust (*Schistocerca gregaria* Forskål). II. Mechanical properties and functioning of the membrane. *J. Exp. Biol.* **203**, 2933-2943.

Song, D., Wang, H., Zeng, L., and Yin, C. (2001). Measuring the camber deformation of a dragonfly wing using projected comb fringe. *Review of Scientific Instruments* **72(5)**, 2450-2454.

Steppan, S. J. (2000). Flexural stiffness patterns of butterfly wings (Papilionoidea). *J. Res. Lepid.* **35**, 61-77.

Swartz, S. M., Bennett, M. B., and Carrier, D. R. (1992). Wing bone stresses in free flying bats and the evolution of skeletal design for flight. *Nature* **359** (6397), 726-729.

Trueman, J. W. H. and Rowe, R. J. (2001). Odonata. In *The Tree of Life Web Project*, (ed. D. R. Maddison and K.-S. Schultz). <http://tolweb.org/tree/phylogeny.html>

Whiting, M. F., Carpenter, J. C., Wheeler, Q. D., and Wheeler, W. C. (1997). The Strepsiptera problem: Phylogeny of the holometabolous insect orders inferred from 18s and 28s ribosomal DNA sequences and morphology. *Syst. Biol.* **46**(1), 1-68.

Wiegmann, B. M. and Yeates, D. K. (1996). Diptera. In *The Tree of Life Web Project*, (ed. D. R. Maddison and K.-S. Schultz). <http://tolweb.org/tree/phylogeny.html>

Wootton, R. J. (1981). Support and deformability in insect wings. *J. Zool., Lond.* **193**, 447-468.

Wootton, R. J. (1990a). The mechanical design of insect wings. *Scientific American* **Nov**, 114-120.

Wootton, R. J. (1990b). Major insect radiations. In *Major Evolutionary Radiations* (ed. P. D. Taylor and G. P. Larwood), Systematics Association Special Volume No. 42, pp. 187-208. Oxford: Clarendon Press.

Wootton, R. J. (1991). The functional morphology of the wings of Odonata. *Adv. Odonatol.* **5**, 153-169.

Wootton, R. J. (1992). Functional morphology of insect wings. *Annu. Rev. Ent.* **37**, 113-140.

Wootton, R. J. (1993). Leading edge section and asymmetric twisting in the wings of flying butterflies (Insecta, Papilionoidea). *J. Exp. Biol.* **180**, 105-117.

Wootton, R. J. (1995). Geometry and mechanics of insect hindwing fans: a modelling approach. *Proc. R. Soc. Lond. B* **262**, 181-187.

Wootton, R. J., Evans, K. E., Herbert, R., and Smith, C. W. (2000). The hind wing of the desert locust (*Schistocerca gregaria* Forskål). I. Functional morphology and mode of operation. *J. Exp. Biol.* **203**, 2921-2931.

Worcester, S. E. (1996). The scaling of the size and stiffness of primary flight feathers. *J. Zool., Lond.* **239**, 609-624.

Zanker, J. M. and Gotz, K. G. (1990). The wing beat of *Drosophila melanogaster*. II. Dynamics. *Phil. Trans. R. Soc. Lond. B* **327**, 19-44.

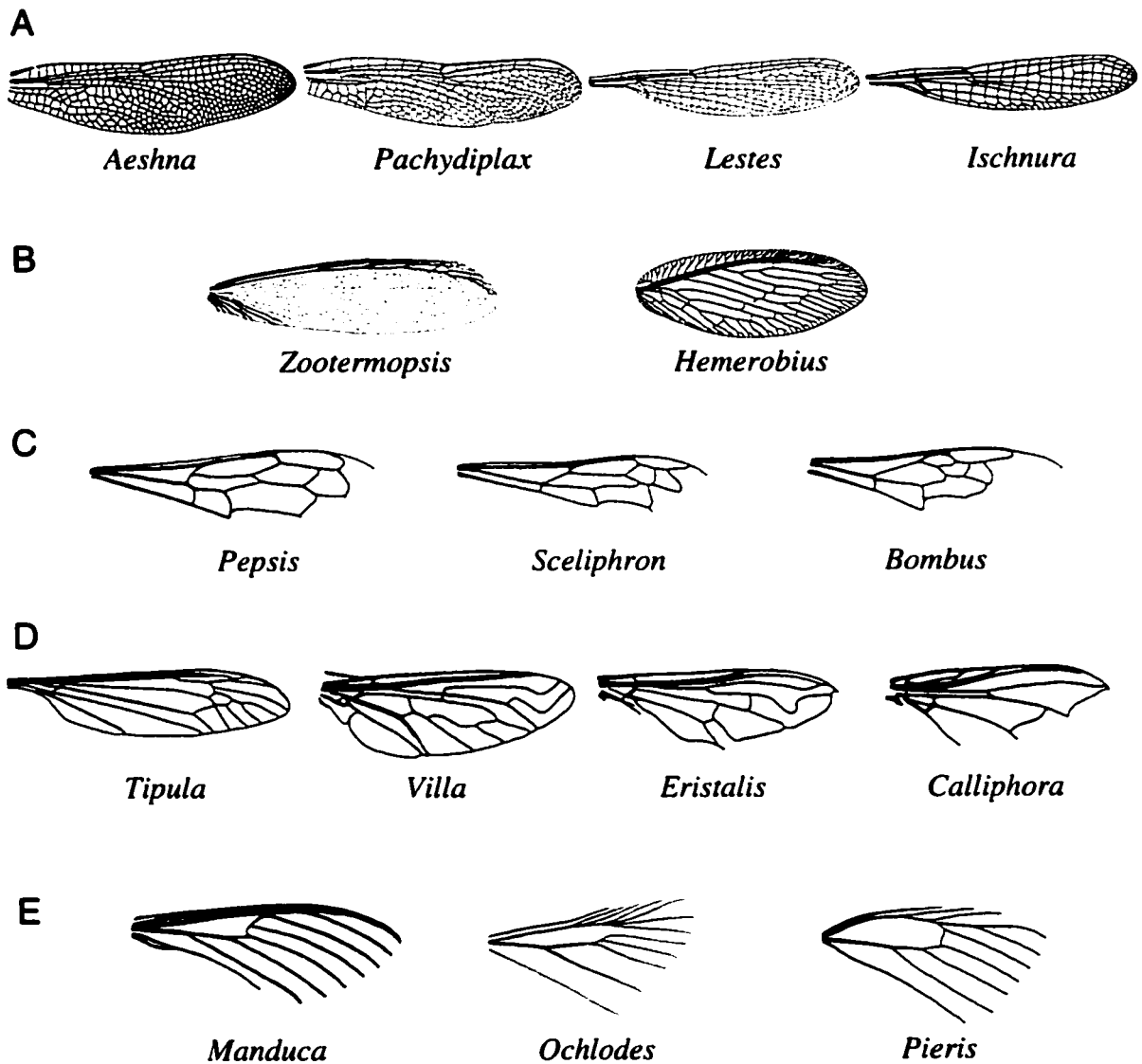


Fig. 3.1. Drawings of forewings from insects used in this study. Veins are drawn at actual thickness; wings are not shown to scale. (A) Order Odonata. (B) Orders Isoptera (*Zootermopsis*) and Neuroptera (*Hemerobius*). (C) Order Hymenoptera. (D) Order Diptera. (E) Order Lepidoptera

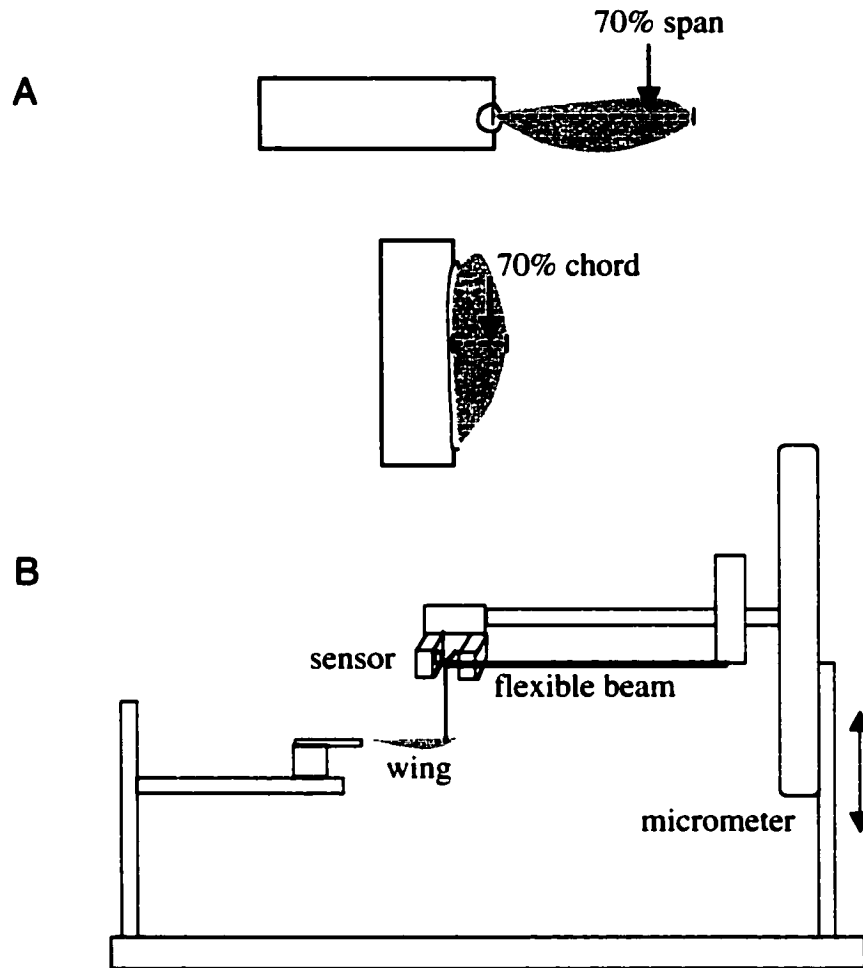


Fig. 3.2. Positions of force application and apparatus to measure displacement and applied force. (A) Fresh wings are fixed to slides with cyanoacrylate glue at either the wing base or leading edge. For spanwise measurements, a point force is applied near the leading edge at approximately 70% wing span (upper panel). For chordwise measurements, a point force is applied (midway between the wing base and tip) at approximately 70% chord length (lower panel). (B) To measure force and displacement, slides are attached to the left side of the apparatus and the right arm is lowered with a micrometer, contacting the wing with a pin attached to a flexible beam. In response, the wing moves down and the flexible beam moves up. A sensor across from an LED light source tracks the movement of the flexible beam and encodes this movement as a voltage change (collected by a MacLab 400 and displayed in Chart 3.5.7 on a Macintosh computer). After calibrating for beam stiffness, this voltage change indicates the force required to move the beam up (and the wing down). The displacement of the wing is the difference between total downward motion of the micrometer and upward motion of the beam.

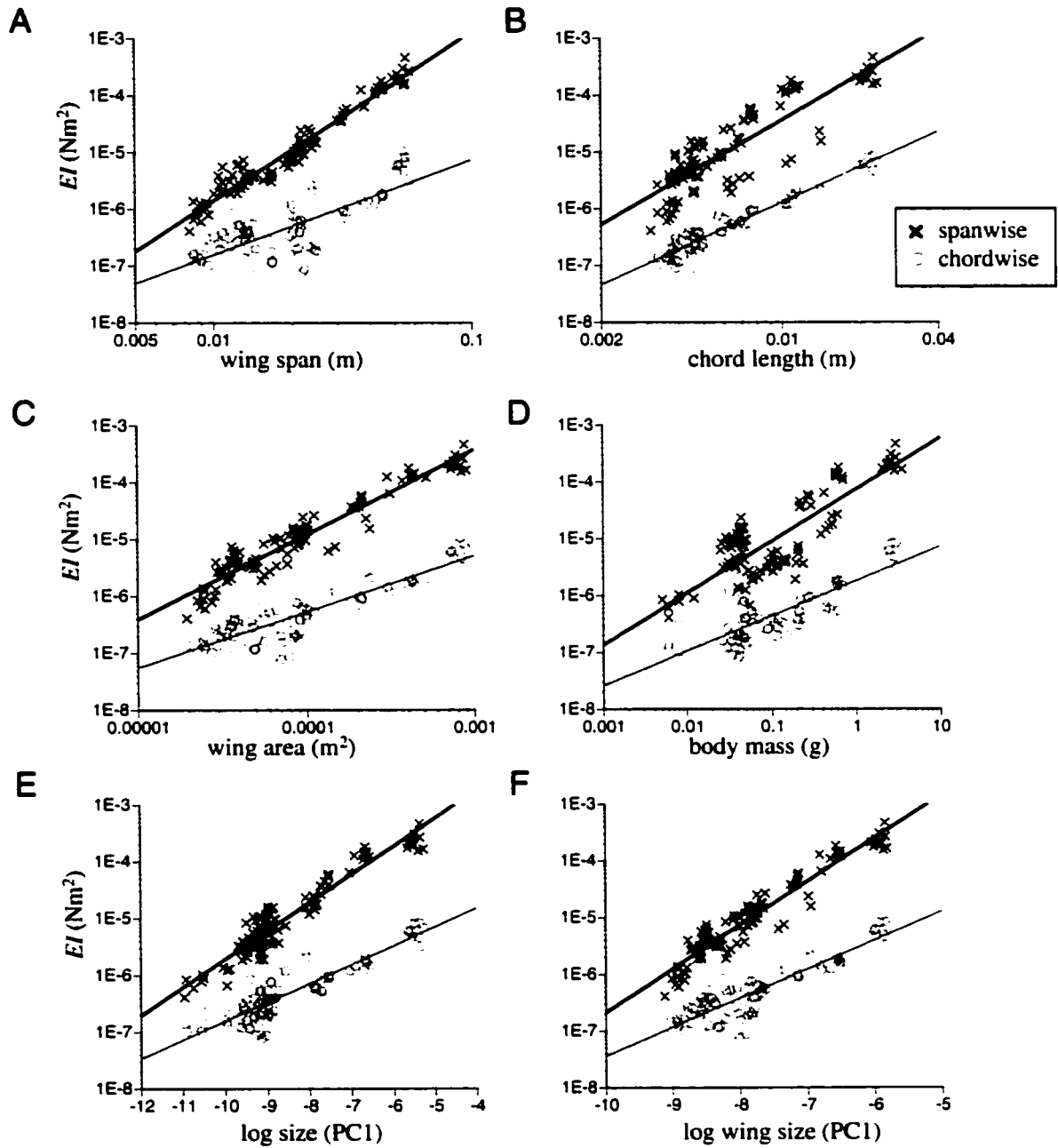


Fig. 3.3. Spanwise and chordwise flexural stiffness *versus* size measurements. Stiffness is measured from the wing base (or leading edge) to 70% of wing span (or chord length). See Table 3.1 for regressions. (A) Flexural stiffness *versus* wing span. (B) Flexural stiffness *versus* chord length. (C) Flexural stiffness *versus* wing area. (D) Flexural stiffness *versus* body mass. (E) Flexural stiffness *versus* size (1st principal component of span, chord and area). (F) Flexural stiffness *versus* wing size (1st principal component of span, chord, area and body mass).

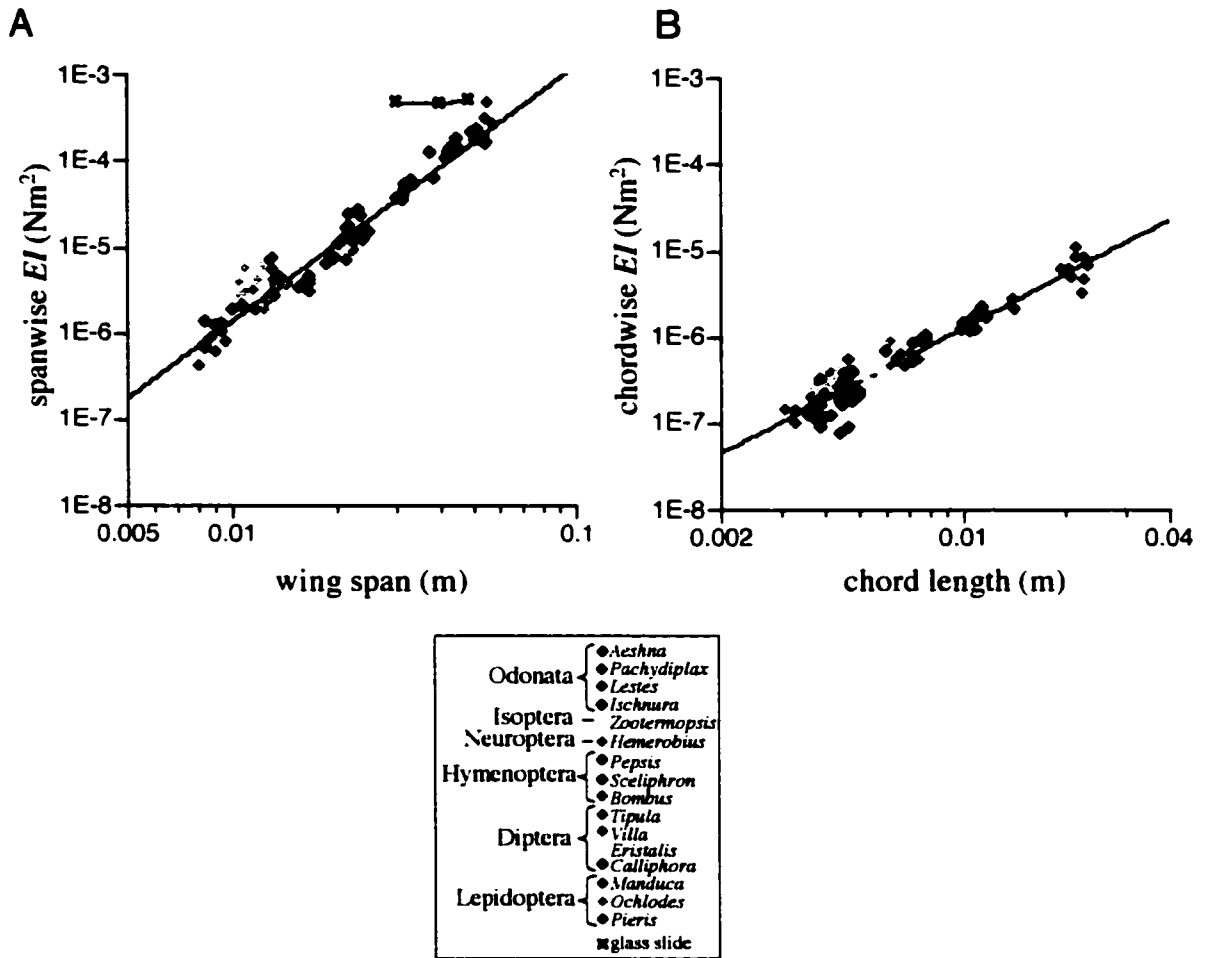


Fig. 3.4. Flexural stiffness *versus* span/chord length in 16 insect species. Individuals of each species are plotted in the same color. Axes are on a logarithmic scale. (A) Spanwise stiffness *versus* wing span; for log-log transformed data, $y = 2.97x + 0.08$, $r^2 = 0.95$ (using species averages, $y = 2.93x + 0.03$, $r^2 = 0.96$). Measured flexural stiffness of a glass coverslip (at varying lengths) is shown in black. (B) Chordwise stiffness *versus* chord length; for log-log transformed data $y = 2.08x - 1.73$, $r^2 = 0.91$ (using species averages, $y = 2.01x - 1.8$, $r^2 = 0.96$).

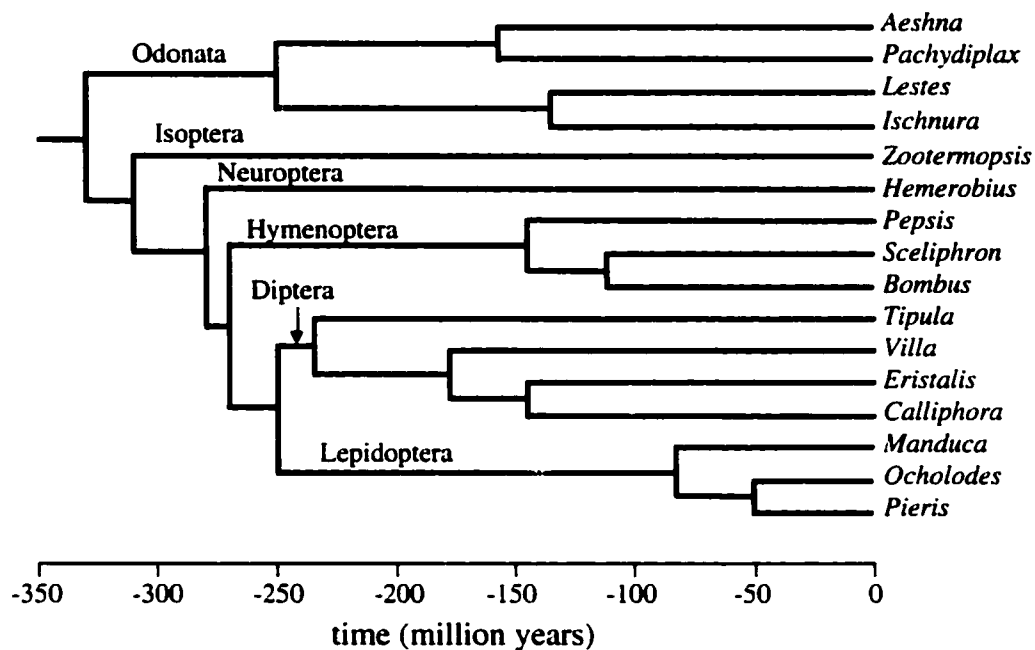


Fig. 3.5. Phylogenetic tree used to calculate independent contrasts. Genera used in this study are in italics; orders are listed at their branching points. Branching of the orders is derived from Kristensen (1991), Kukalova-Peck (1991), and Whiting et al. (1997). Divergence dates of the orders are based on fossil evidence from Kukalova-Peck (1991) and Wootton (1990b). Branching patterns within the following orders are taken from the Tree of Life Web Project: Odonata (Trueman and Rowe, 2001); Hymenoptera (Maddison, 1995a); Lepidoptera (Maddison, 1995b), and Diptera (Wiegmann and Yeates, 1996). Divergence dates within orders are based on fossil evidence (Benton, 1993).

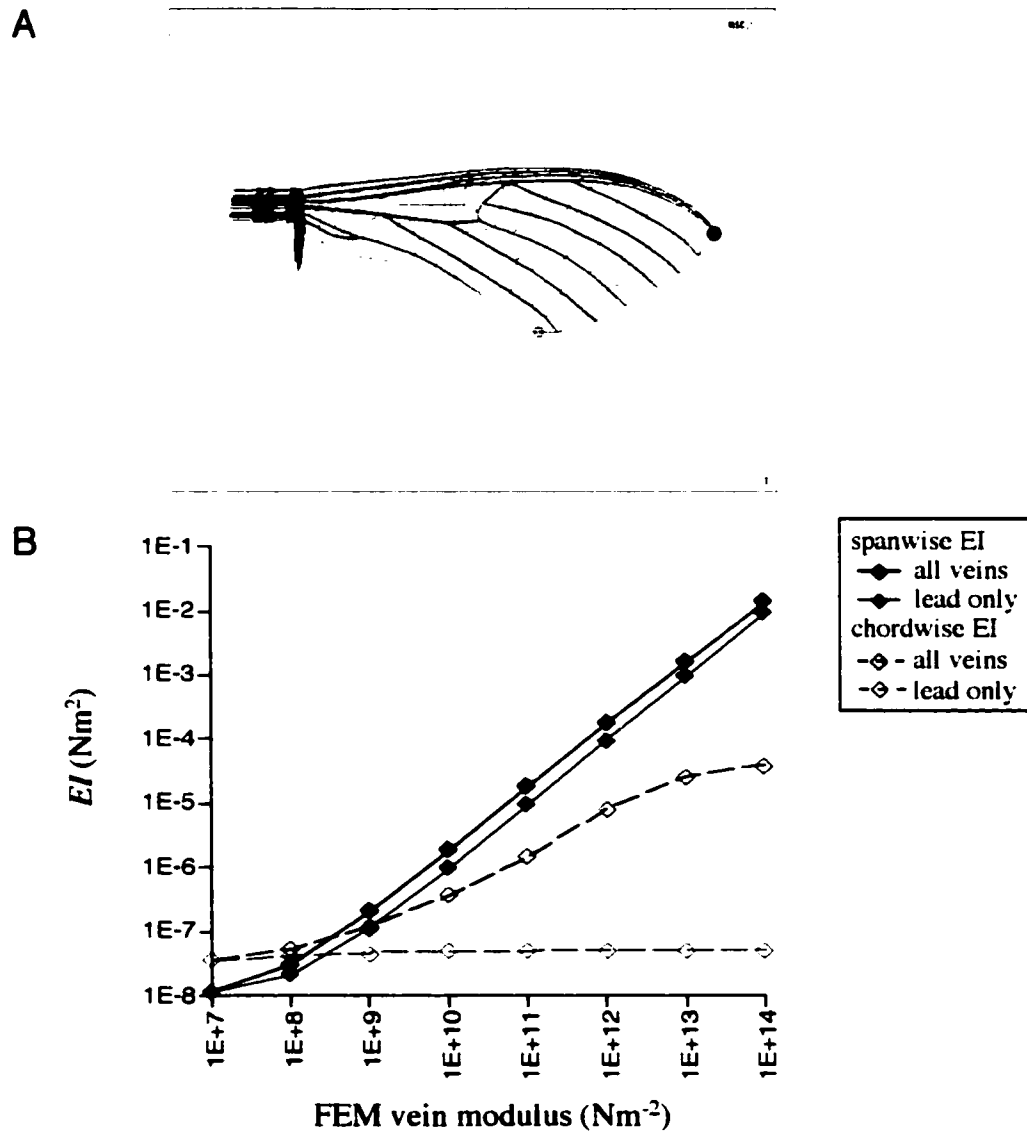


Fig. 3.5. Finite element model of a *Manduca sexta* wing and results of virtual bending experiments. (A) Finite element model (FEM) with leading edge vein elements in pink, other vein elements in green, and membrane elements in yellow. For calculations of spanwise flexural stiffness, the wing is fixed at the base (with no displacement or rotation, blue arrows) and a point force is applied to the tip (blue dot). For calculations of chordwise flexural stiffness, the wing is fixed at the leading edge and a point force is applied to the trailing edge (orange dot). (B) Wing flexural stiffness (calculated from applied force and wing displacement) versus Young's modulus of vein elements. In all simulations, the modulus of the wing membrane is $1 \times 10^7 \text{ Nm}^{-2}$. Trials in which the modulus of all wing veins is increased are in green; trials in which only the leading edge vein modulus is increased (while the other veins remain at $1 \times 10^7 \text{ Nm}^{-2}$) are in pink.

Table 3.1. Regressions of flexural stiffness *versus* size measurements. Regressions are calculated from measurements of individual insects from 16 species (n = 96). All regressions are significant, with p-values < 0.0001.

	log spanwise EI	r ²	log chordwise EI	r ²
log wing span	$y = 2.97x + 0.08$	0.95	$y = 1.68x - 3.45$	0.60
log wing chord	$y = 2.64x + 0.84$	0.74	$y = 2.08x - 1.73$	0.91
log wing area	$y = 1.50x + 1.07$	0.92	$y = 0.99x - 2.32$	0.79
log body mass	$y = 0.91x - 4.13$	0.70	$y = 0.61x - 5.74$	0.63
log size (PC1)	$y = 0.50x - 0.75$	0.92	$y = 0.33x - 3.49$	0.81
log wing size (PC1)	$y = 0.77x + 1.02$	0.92	$y = 0.51x - 2.33$	0.80

Chapter 4

Flexural stiffness in insect wings:

Distribution of wing stiffness and effects on wing bending

Summary

The dynamic, three-dimensional shape of flapping insect wings may influence many aspects of flight performance. Insect wing deformations during flight are largely passive, and are controlled primarily by the architecture and material properties of the wing. Although many details of wing structure are well understood, the distribution of flexural stiffness in insect wings and its effect on wing bending is unknown. In this study, I develop a method to estimate variation in flexural stiffness in both the spanwise and chordwise direction of insect wings. I measure displacement along the wing and model stiffness variation as a simple mathematical function capable of approximating the measured displacement. I use this method to estimate stiffness variation in the hawkmoth, *Manduca sexta*, and in the dragonfly, *Aeshna multicolor*. In both species, stiffness declines sharply from wing base to tip and from the leading to the trailing edge; this variation can be approximated by an exponential decline. Moreover, the wings of both species display non-linear behavior, in which stiffness increases as the applied force rises. A dramatic dorsal/ventral asymmetry in wing stiffness is present in *M. sexta*, but absent in *A. multicolor*. In addition, male and female *M. sexta* display significant differences in chordwise stiffness. Finite element models based on the wings of *M. sexta* demonstrate that the sharp decline in spanwise and chordwise flexural stiffness preserves

rigidity in proximal regions of the wing, while transferring bending to the edges, where aerodynamic force production is most sensitive to subtle shape changes.

Key words: insect flight, wing flexibility, flexural stiffness, stiffness distribution, *Manduca sexta*, *Aeshna multicolor*, finite element model

Introduction

During flapping flight, insects wings accelerate and decelerate masses of air, generating the forces necessary to support an insect's weight and to perform complex maneuvers. At the same time, these ultralight airfoils (generally only 0.5-3% of body mass; Ellington, 1984b) must withstand the forces imposed on them by the surrounding air, as well as the inertial forces caused by accelerating and decelerating their own mass up to several hundred times per second.

Insect wings perform these roles extremely successfully, despite the fact that they are largely passive structures (Wootton, 1992), with no muscular control past the wing base. Although they are strengthened by a network of tubular veins, the wings of many species deform noticeably during flight, especially during slow flight and hovering (Willmott and Ellington, 1997a). These dynamic changes in the three-dimensional shape of wings could potentially affect many aspects of force production, yet few models of insect flight have successfully incorporated passive wing flexibility or examined the effects of flexibility on force production.

In the past two decades, models of insect flight, both mathematical (Ellington, 1984a; Wilkin and Williams, 1993; Smith et al., 1996; Sane and Dickinson, 2002) and physical (Ellington et al., 1996; Dickinson et al., 1999; Birch and Dickinson, 2001), have contributed enormously to our understanding of basic mechanisms of force production, despite assuming that insect wings are rigid structures. Some aspects of wing flexibility have been mimicked in models by altering the relative positions of wing regions (i.e. altering fore and hindwing position to generate camber, Liu et al., 1998, or varying angle of attack at the leading edge to generate spanwise torsion, Vest and Katz, 1996) or by modeling deformations as harmonic waves (Wu, 1971; Daniel, 1987; Combes and Daniel, 2001). Each of these approaches provides unique insights into the mechanisms of force generation during flight, but they often neglect one or more critical components of wing deflection (i.e., spanwise bending, chordwise bending, or torsion), which can have large effects on aerodynamic force production (for example, increasing chordwise camber by only five degrees can lead to a six-fold increase in lift production; Batchelor, 1967).

The dynamic, three-dimensional shape of flapping wings could be reproduced by measuring the precise locations of multiple parts of the wing during a stroke and specifying these coordinates in a model wing. However, a simpler and more robust approach would be to construct a model wing that deforms passively; once constructed, this type of model could be used not only to reproduce the motions of a flying insect, but also to experiment with kinematics and loading regimes that are not seen in nature.

Smith (1996) simulated the aerodynamics of flapping flight in the hawkmoth, *Manduca sexta*, by using an unsteady aerodynamic panel method coupled with a finite element model of the wings that accounts for wing flexibility. This finite element model incorporated varying wing thickness and accurately reproduced the center of mass and radius of gyration for a *Manduca* wing. However, the model neglected several features of vein structure and was not able to predict force production as well as a model wing in which the coordinates of the entire wing were specified in advance.

One of the difficulties in modeling passive wing flexibility is that forces applied at the wing base lead to bending and twisting that are influenced not only by overall stiffness and gross anatomical features (i.e. flexion or fold lines), but also by the distribution of flexibility throughout the wing (Wootton, 1999). Extremely detailed finite element models of insect wings (incorporating vein configuration, three-dimensional relief, and variations in vein radius, vein wall thickness, and membrane thickness) can sometimes reproduce the distribution of bending stiffness in real wings by accounting for the precise wing structure and material properties of the wing. These types of models have been used to study the behavior of wings subjected to steady loads (Kesel et al., 1998) or undergoing transient motions (Herbert et al., 2000). However, measuring and duplicating the precise geometry of wing veins and membranes is time-consuming. In addition, many models assume that the elastic modulus of the wing (E , stiffness of wing material) is equivalent to that of insect chitin and constant throughout the wing (Smith, 1996; Kesel et al., 1998), but recent measurements reveal that E varies by almost two orders of magnitude in the membrane regions of the locust hindwing (Smith et al., 2000).

The extent of variation in the elastic modulus of wing veins is unknown, and the assumption that wings are composed solely of chitin is no longer valid, as other proteins such as resilin have been found in the wing vein joints of many species (Gorb, 1999; Haas et al., 2000a; Haas et al., 2000b).

Highly detailed finite element models of insect wings will undoubtedly continue to add to our understanding of functional morphology and specific wing mechanisms in pivotal, well-studied species. At the same time, a more general understanding of how overall stiffness (due to both architecture and material properties) varies throughout insect wings would allow essential components of passive flexibility to be included in models of insect flight, and would facilitate comparative studies of wing stiffness that may help explain broad evolutionary trends in insect wing design (see Chapter 3).

Qualitative trends of how overall stiffness varies throughout insect wings have been noted for some time. Most wings have relatively stiff, supporting zones near the wing base and leading edge, and relatively deformable areas near the edges of the wing (Wootton, 1981). Insect wing veins taper in diameter from base to tip (Wootton, 1992), and the presumed reduction in stiffness this taper provides could potentially serve many purposes, including reducing the inertial load at wing tips (thus reducing energy expenditure and stress at the wing base) and allowing wing tips to buckle and rebound from collisions without damage (Wootton, 1992). In fact, a wing that is stiff at the base and more flexible at the tip would seem perfectly suited to withstand the bending torques (which decline sharply from base to tip) generated by flapping (Ennos, 1989).

Whereas qualitative information about wing stiffness distributions is available for a wide range of species, quantitative measurements of local stiffness in insect wings are scarce. Stepan (2000) measured profiles of flexural stiffness (EI , the product of Young's modulus and the second moment of area) in dried butterfly wings by applying a load at several locations along the length. He found that stiffness declines towards the wing tip, as expected, and also measured an unexpected decline in stiffness near the wing base (a region that he explains may be more prone to measurement errors). Wootton et al. (2000) measured average flexural stiffness in three different zones of the locust hindwing by cutting the wing apart, and Smith et al. (2000) measured variation in Young's modulus in membranes of the locust hindwing. Yet no studies to date have demonstrated a reliable method of measuring continuous variation in the bending stiffness of intact insect wings.

In this study, I develop a method of approximating continuous variation in flexural stiffness along two axes of the wing (in the spanwise and chordwise direction). I focus on variation in flexural stiffness (EI) rather than Young's modulus (E), because flexural stiffness provides an overall measure of how the wing will bend in response to an applied load, without unraveling the contributions of complex geometry or variation in material stiffness that lead to this behavior.

I measure variation in flexural stiffness in two insects, the hawkmoth *Manduca sexta* and the dragonfly *Aeshna multicolor*. These insects have wings of similar size, and are both agile fliers, capable of hovering as well as fast, forward flight. However, they are very distantly related and display large differences in wing shape and venation

pattern (see Chapter 3) that might underlie differences in the distribution of stiffness in their wings. In addition, the wing structure and flight performance of both hawkmoths and dragonflies has been extensively analyzed and modeled (for example, Kesel et al., 1998; Liu et al., 1998; Smith, 1996; Soms and Luttges, 1985; Sunada et al., 1998; Wakeling and Ellington 1997a,b,c; Wilkin and Williams, 1993; Willmott and Ellington, 1997a,b; Wootton, 1991).

To assess the spatial pattern of flexural stiffness in wings, I first develop a method to measure displacement (due to a point force) along the wing in the spanwise and chordwise directions. Next, I propose various alternatives for how stiffness might vary along the wing (represented by simple mathematical functions) and predict the pattern of displacement that a loaded wing with these theoretical stiffness distributions would display. Finally, I find the stiffness distribution that produces a pattern of displacement most similar to the pattern of displacement measured in a real wing. I use this method to estimate the stiffness distribution of the wing to forces applied from both the dorsal and the ventral side of the wing, as dorsal/ventral asymmetry has been noted in previous studies (Ennos, 1988; Stepan, 2000; Wootton, 1993; Wootton et al., 2000)

Finally, I create two finite element models of insect wings, using *Manduca sexta* as a model. Rather than realistically reproducing the structure and behavior of *Manduca* wings, these generalized models provide a method of assessing the consequences of stiffness distributions to wing bending. I attempt to capture major elements of wing structure in the models (i.e. vein position and flexural stiffness distribution) while avoiding detailed structural features, such as variation in wing thickness and three-

dimensional relief. I use these models to assess the effects of flexural stiffness distribution on wings subjected to both static and dynamic loads.

Materials and Methods

Insect collection and handling

For measurements of wing stiffness, I used hawkmoths (*Manduca sexta*) from a colony at the University of Washington and collected dragonflies (*Aeshna multicolor*) on the campus of the University of Washington. I measured wing stiffness on hawkmoths immediately after removing them from the colony, and on dragonflies within 2 to 3 days of capture (during which time I stored them in a humidified chamber at 4°C). Before removing wings, I anaesthetized insects by placing them in the freezer for 1 to 5 minutes, then weighed the entire insect, removed one wing at the base, and placed the insect back in the refrigerator. I weighed the wing and attached it to a glass slide with cyanoacrylate glue and baking soda, at either the wing base (for spanwise measurements) or the leading edge (for chordwise measurements), using a minimal amount of the wing for attachment (no more than 2 mm). I completed all measurements on a wing within one hour of removing the wing from the insect (during which time the stiffness of the wing does not change appreciably).

After measuring stiffness of the first wing, I retrieved the insect from the refrigerator, removed another wing, and repeated the procedure. In each hawkmoth, I measured spanwise stiffness on one forewing and chordwise stiffness on the other. I did not measure the stiffness of the hindwings, which are much smaller and overlap with the

forewings to varying degrees during flight. In dragonflies (which have independent fore- and hindwings of similar size), I measured spanwise stiffness on one forewing and one hindwing, and chordwise stiffness on the other forewing and hindwing.

Measurement of wing stiffness: force and static wing deformations

I measured continuous displacement of wings in the spanwise direction along a line running from the wing base to the tip, and in the chordwise direction along a line running from the leading edge to the trailing edge (approximately midway between the base and tip). I first attached a slide with a wing projecting from it to the left side of the apparatus shown in Fig. 3.2 (see Chapter 3) and lowered the right arm of the apparatus until the pin contacted the tip or trailing edge of the wing on its dorsal surface. I applied a small drop of cyanoacrylate glue with a 30-gauge syringe to prevent the pin from sliding off the edge of the wing, and illuminated the wing with a laser split into sheets of light. The sheets of light appear as lines on the wing, and can be adjusted so that one line illuminates a strip of the wing from the base to the tip (as in Fig. 4.1A) or from the leading to the trailing edge (intersecting the pin).

Before applying the point force, I photographed wings with a Nikon Coolpix 900 angled approximately 45° from the surface of the wing, using the "fine" quality setting (resolution of 2048 x 1536 pixels). I photographed wings with overhead lights on and with lights off (so only the laser lines were visible; Fig 4.1A). I then lowered the right arm of the apparatus to apply a point force to the tip or trailing edge of the wing; when this force is applied, the laser lines follow the surface of the wing, shifting their

position in proportion to the displacement of the wing downwards (Fig. 4.1B). After applying the point force, I photographed the loaded wing with lights on and lights off, while an LED sensor on the apparatus encoded the applied force and displacement of the wing at the tip or trailing edge as a voltage change (see Fig. 3.2).

In early trials, I found that wing displacement is not a linear function of applied force, so I measured displacement at several different loads, returning to the unloaded position to photograph the wing before applying each new load. I checked the repeatability of displacement measurements on the wings of a hawkmoth (in both the spanwise and chordwise direction) by applying five different loads to the dorsal surface of the wing and repeating each load three times (applying loads in random order).

For all other hawkmoth and dragonfly wings, I measured displacement on the dorsal surface of the wing at four different loads, gently removed the glued pin from the edge of the wing (without tearing the wing membrane), flipped the slide over, and measured displacement on the ventral side of the wing at four different loads. Dorsal stiffness in this study describes the stiffness of the wing in response to loading on the dorsal surface (resulting in a dorsally convex surface; see Stepan, 2000), which is equivalent to ventral flexion in other studies (Ennos and Wootton, 1989; Wootton, 1981; Wootton, 1992).

Before moving the camera, I photographed a 2-mm grid in the position the wing occupied to provide a spatial calibration. I also photographed a series of slides glued together to form steps of known height; with laser lines projecting down the steps, this image provides a calibration for how far the line in the image shifts given a known

change in the height of the object (Fig 4.1C). Finally, I photographed the wing on a white background from above and measured wing area, span, and maximum chord length in NIH Image. For *Manduca sexta* (whose wing morphology may depend on gender; Willmott and Ellington, 1997b), I also calculated aspect ratio ($\text{span}^2/\text{area}$) of the forewings and wing loading (body mass divided by the area of both forewings).

I calculated the applied force for each loading (see Fig 3.2) and found continuous displacement along a laser line by analyzing the unloaded and loaded images of the wing. I converted the images to grayscale and used a Matlab program (Appendix 4) to find the center of the horizontal laser line running from wing base to tip or leading to trailing edge (Fig. 4.1A,B); this program finds the center of the line one pixel at a time by sampling the intensity of a column of pixels surrounding the line and applying a Gaussian least squares fit to find the peak of the intensity gradient, which is taken to be the center of the line at that position (method developed by A. Trimble, see Appendix 4).

The laser lines begin at the same position in the two images (near the point of attachment to the slide), but the line in the loaded image is shorter (in the x -direction) than the line in the unloaded image (Fig. 4.1B). To be sure that I was comparing the same points on the unloaded and loaded wing, I used the lighted images to find the edge of the wing in each image (dotted lines in Fig. 4.1B), and used this position as the end point for sampling the lines.

Finally, I used Matlab to filter noise from the line position data and splined the unloaded and loaded data to an equal number of points for comparison (Appendix 4). I found the difference in line position between the two data sets ($y(x)$) and converted this

difference to actual wing displacement ($\delta(x)$) with a factor derived from analysis of the calibration image (Fig. 4.1C, Appendix 4).

Measurement of wing stiffness: calculation of local flexural stiffness

To calculate local flexural stiffness, I treated each wing as a heterogeneous, two-dimensional beam in the spanwise (or chordwise) direction, and used a continuous beam equation to estimate stiffness along this axis. With the beam attached at one side and a point force applied at the other end, flexural stiffness at any point along the beam is the moment at that position divided by the local curvature (or the 2nd derivative of displacement):

$$EI(x) = \frac{M(x)}{d^2\delta / dx^2} \quad (4.1)$$

where $M(x)$ is the moment at position x along the beam and δ is the displacement (in the z-direction) at position x . If we assume that the point force is applied at an angle approximately 90° from the beam, then the moment is the product of the applied force and the distance between the point of force application and position x on the beam:

$$EI(x) = \frac{F(L-x)}{d^2\delta / dx^2} \quad (4.2)$$

where F is the applied force and L is the total length of the beam.

Although continuous displacement ($\delta(x)$) is known from analyzing the wing images, differentiating these data to solve Eq. 4.2 may lead to an erroneous solution. If the displacement data is differentiated over a very small interval, individual pixel noise in

the images overwhelms the solution; as the interval is increased, the solution for EI continues to change, and there is no objective justification for choosing one interval size over another.

To avoid these problems, I solved the equation in reverse; I posed a functional distribution for $EI(x)$, calculated the expected displacement ($\delta(x)$), and used a simplex minimization program to adjust the coefficients of the functional EI distribution to minimize the difference between predicted and measured wing displacement.

I proposed that stiffness in the spanwise or chordwise direction might be constant, or that its spatial pattern might be approximated by a linear, exponential, or 2nd-degree polynomial equation:

$$EI(x) = d \quad (4.3)$$

$$EI(x) = mx + b \quad (4.4)$$

$$EI(x) = c \cdot \exp^{ax} \quad (4.5)$$

$$EI(x) = px^2 + qx + r \quad (4.6)$$

Each of the proposed EI distributions (Eq. 4.3-4.6) can be inserted into the following equation to find the expected displacement along the span or chord given an applied moment ($F(L-x)$):

$$\delta(x) = \int_0^L \left[\int_0^x \frac{F(L-x')}{EI(x')} dx' \right] dx \quad (4.7)$$

I used a simplex minimization program in Matlab that tests various values of the coefficients (for example, m and b in Eq. 4.4) to find the specific EI distribution (for each

equation type) that most successfully predicts wing displacement along the span or chord (Fig. 4.2).

To verify the method of measuring local flexural stiffness, I measured $\delta(x)$ for a rectangular glass coverslip, which is made of homogeneous material and has a known Young's modulus (E) and second moment of area (I). I attached the coverslip to a glass slide at one end, dusted its surface lightly with baking soda (to visualize the laser line), and used the same apparatus as above to apply a point force to the opposite end. I photographed the unloaded and loaded coverslip, used the Matlab code to find displacement along the length, and used simplex minimization to solve for the distribution of flexural stiffness.

While the spatial variation in flexural stiffness along a wing provides valuable information about wing structure, average flexural stiffness in the spanwise and chordwise directions may also be useful for comparisons between individuals and species. To calculate average flexural stiffness (\overline{EI}) of a wing, I integrated the continuous distribution $EI(x)$:

$$\overline{EI} = \frac{1}{(x_{\max} - x_o)} \int_{x_o}^{x_{\max}} EI(x) dx \quad (4.8)$$

where x_o is the starting point (near the base or leading edge) and x_{\max} is the end point of data collection.

As mentioned previously, the relationship between applied force and wing displacement in hawkmoth and dragonfly wings appears to be non-linear. Because of this, estimated wing stiffness varies with wing strain (approximated by tip or trailing

edge displacement divided by span or chord length). To test whether wing stiffness varies in a predictable, directional manner with increasing loads (which would suggest non-linear behavior), I plotted \overline{EI} against strain (with dorsal, ventral, spanwise and chordwise measurements plotted separately for each individual). I fitted a line to each relationship and used a non-parametric one sample sign test in Statview to determine if the slopes (from all individuals) of each relationship are significantly different from zero, the slope expected for a linear wing in which stiffness is independent of strain.

Comparisons of wing stiffness

Determining the relationship between wing stiffness and strain also allowed me to standardize stiffness measurements, facilitating comparisons between individuals. Because I did not know the applied force or displacement of wings until after experiments were completed, I was unable to perform the bending experiments at set levels of strain or applied force. However, I was able to later determine the stiffness distribution and average stiffness of all wings at the same level of strain by calculating the slopes of the relationships between wing distribution coefficients and strain.

For both the spanwise and chordwise direction, I standardized measurements at a strain that fell within the range of values measured on wings. Spanwise strain (tip displacement divided by wing span) varied from 0.014 to 0.07 in *Manduca sexta*, and from 0.018 to 0.086 in *Aeshna multicolor*. I chose to calculate spanwise wing stiffness at a strain of 0.05 for comparison. In the chordwise direction, strain varied from 0.034 to

0.176 in *Manduca sexta* and from 0.031 to 0.161 in *Aeshna multicolor*. I chose to compare wings at a chordwise strain of 0.08.

In *Manduca sexta*, I collected spanwise data from 9 males and 4 females, and chordwise data from 10 males and 9 females. In *Aeshna multicolor*, I used only males, but tested both fore and hindwings (which have different morphologies), so I examined stiffness separately in the two sets of wings. I collected spanwise and chordwise data on both fore and hindwings from 8 individuals.

Within each group, I tested for differences between the dorsal and ventral side of the wing with a Wilcoxon signed rank test. I also tested for differences between male and female *Manduca sexta* with a Mann-Whitney U-test.

Static finite element modeling

To investigate how the distribution of stiffness in a wing affects bending, I constructed two finite element models based on a *Manduca sexta* wing using MSC Marc/Mentat 2001. Both models are created from a planform image of a male *Manduca* wing and consist of 345 thin shell elements (with a mixture of 3- and 4-node elements) representing the veins and membrane of the wing.

The models are composed of flat elements with a uniform thickness of 110 μm (an approximation of average wing stiffness). In one of the models, I assigned all vein elements a single (homogeneous) material stiffness (E , Young's modulus), and all membrane elements a different homogeneous material stiffness (Fig.4.3A). I performed virtual bending experiments similar to those performed on real *Manduca* wings; I fixed

the nodes at the base of the wing (with no displacement or rotation), applied a point force to the tip of the wing, and recorded the calculated tip displacement. Similarly, to measure displacement in the chordwise direction, I fixed the wing at the leading edge and applied a point force to the trailing edge. I then adjusted vein and membrane stiffness so that the tip and trailing edge displacements due to a given force were similar to displacements seen in real wings (final membrane and vein moduli are $2 \times 10^7 \text{ Nm}^{-2}$ and $2 \times 10^{11} \text{ Nm}^{-2}$, respectively).

In the other model, I mimicked the pattern of flexural stiffness measured in *Manduca* wings (Fig. 4.3B). A declining exponential function provides the best approximation of local flexural stiffness in both the spanwise and chordwise direction of *Manduca* wings (see Results). I therefore applied declining values of Young's modulus to the model wing in 12 strips oriented diagonally (so that stiffness declines in both the spanwise and chordwise direction; see Fig. 4.3B). Within each strip, the vein elements are several orders of magnitude stiffer than the membrane elements (to preserve spanwise-chordwise anisotropy - see Chapter 3). As in the model with homogeneous vein and membrane stiffness, I adjusted the moduli until calculated tip and trailing edge displacement matched values measured in real wings (Young's modulus varies from $2.86 \times 10^{12} \text{ Nm}^{-2}$ at the base to $1.65 \times 10^{10} \text{ Nm}^{-2}$ at the tip in vein elements, and from $9.85 \times 10^8 \text{ Nm}^{-2}$ to $5.71 \times 10^6 \text{ Nm}^{-2}$ in membrane elements).

Because the two finite element models share the same geometry and exhibit the same overall bending performance (tip and trailing edge displacement are nearly identical for a given load), they provide an ideal opportunity to investigate the effects of

stiffness distribution on patterns of bending. To determine the spanwise stiffness distribution of the model wings, I fixed each wing at its base and applied a point force at the tip. I recorded the displacement of 18 nodes aligned from the base of the wing to the tip and used this information to estimate stiffness distribution with the Matlab simplex minimization program (in the same way that I used continuous wing displacement to estimate stiffness distribution in real wings). I determined chordwise stiffness distribution similarly, by fixing each wing at the leading edge (from the base to approximately $2/3$ wing span), applying a point force at the trailing edge, and recording displacement at 18 nodes between the leading and trailing edge.

To determine how these different stiffness distributions affect wing bending, I first applied static loads to the model wings. I fixed each wing at its base and applied a point load of 0.005 N at the tip (within the range of loads applied to real wings) or a pressure load of -14.43 Pa to the wing surface (equivalent to the lift force that the wing would experience during steady flight). I then compared the patterns of displacement in the two models.

Dynamic finite element modeling

Although static tests provide some information about how wing stiffness distributions affect bending, real wings are unlikely to experience anything like a point force during flight. And although wings may experience steady aerodynamic forces at certain points in a wing stroke, other forces (such as the inertia of the wing itself) may be more important in determining how wings bend during flapping flight (see Chapter 5).

I used a simple kinematic pattern to examine how rapid, unsteady motions affect bending in the two model wings. I rotated each model wing around one axis (the y-axis, see Fig. 4.3) at the base, with no displacement at the base nodes. I started the wing from rest and gradually increased the amplitude of motion to a sinusoidal curve with the following equation:

$$\theta = (1 - e^{-t/\tau}) * \sin(\omega t) \quad (4.9)$$

where θ is the rotation at the base nodes (standardized to an amplitude of +/-1 radian), t is time in seconds, τ is the time constant and ω is the angular frequency ($2\pi f$, where f is the flapping frequency). I rotated the wing at 26 Hz (a realistic wing beat frequency for *Manduca*) and multiplied the standardized amplitude by 0.9245 radians to rotate the wing through a total amplitude of 108.5°. I adjusted the time constant ($\tau = 1/50$) to minimize the effects of initial conditions at the base.

I set the density of elements at 500 kg/m³ to provide the correct total wing weight of 0.035 g (given the element thickness and total area of the model wing). This density may be lower and the average thickness higher than in real *Manduca* wings, but because the mass distribution is uniform, these values should have little effect on the results. The uniform mass distribution may also cause bending in the distal regions to be overestimated, but the qualitative differences in wing bending between the two models should not be affected by this assumption. I set the Poisson's ratio of wing elements at 0.495 (consistent with measured values of biological materials; Wainwright et al., 1982)

Because the model does not calculate aerodynamic forces acting on the wing, a damping factor must be applied. I use a mass damping factor of 300 on the elements of

the wing, a value which produces wing motions that most closely match those measured in real *Manduca* wings undergoing the same rotation (see Chapter 5).

I used the large-displacement solution option and tested for convergence using the relative/absolute displacement option with tolerances of 0.05 and 0.005, respectively. I ran the model for 1200 time steps, simulating a total flapping time of 0.24 seconds. Within this time, the wing rotates through 6.25 cycles, with the last 3.5 cycles at full amplitude. I compared bending in the two model wings during the last rotation cycle.

Results

Calculation of local flexural stiffness

The patterns of wing displacement measured in *Manduca sexta* are significantly different from those predicted for a wing with constant flexural stiffness or with stiffness that varies linearly in the spanwise direction (Fig. 4.2A,B). Displacement patterns in the chordwise direction of *Manduca* wings, as well as in the spanwise and chordwise directions of *Aeshna multicolor* wings, also differ from those predicted by constant or linear stiffness distributions.

Both exponential and 2nd-degree polynomial distributions of flexural stiffness provide a relatively good prediction of wing displacement (Fig. 4.2C,D, right panels). However, the 2nd-degree polynomial distributions that provide the best fit for wing displacement sometimes increase in stiffness towards the tip or trailing edge (Fig. 4.2D, left panel), and often pass below zero, particularly for stiffness in the chordwise direction. On the other hand, an exponential stiffness distribution provides results that

are consistent among individuals, and effectively predicts displacement in the spanwise and chordwise directions in both *Manduca sexta* and *Aeshna multicolor*. I therefore chose an exponential equation as the best approximation for patterns of wing stiffness in the insects tested.

Applying repeated loads (in random order) to the dorsal surface of a *Manduca* wing revealed that these estimates of stiffness distribution are generally repeatable (i.e. lines of the same color in Fig. 4.4), particularly for larger loads where image resolution is better. In addition, control measurements on a glass coverslip provide an approximation of constant stiffness along the length (as expected), validating the method of estimating local flexural stiffness (Fig. 4.4).

Averages of local flexural stiffness along the length of wings (\overline{EI}) are related to the effective strain (displacement per length) of the wing. The slopes of the relationship between \overline{EI} and strain are significantly different from zero in nearly all cases (Table 4.1), indicating that much of the variability in these stiffness estimates may be due to non-linear behavior of the wings. In addition, the slopes are nearly always positive (Table 4.1), suggesting that wings of both species become effectively stiffer when subjected to larger loads (see Fig. 4.4).

Comparisons of wing stiffness

Wing stiffness and morphological measurements of both species are shown in Tables 4.2-4.4. Female *Manduca sexta* are heavier and have larger wings than males, but aspect ratio and wing loading are the same in the individuals sampled (Table 4.5).

Although overall wing stiffness scales with wing size across a broad range of species (see Chapter 3), spanwise \overline{EI} is not significantly different between male and female hawkmoths (Table 4.5). In the chordwise direction, \overline{EI} is higher in females on the dorsal side of the wing, but not on the ventral side. The exponents of the stiffness distribution in the chordwise direction are also higher in females than in males, but exponents in the spanwise direction are the same in males and females (Table 4.5, Fig. 4.5A).

The wings of all *Manduca sexta* are stiffer on the dorsal side than on the ventral side, in both the spanwise and chordwise direction (Table 4.6). In contrast, *Aeshna multicolor* has no dorsal/ventral difference in its hindwings or in the chordwise direction of its forewings (Table 4.6, Fig. 4.5B). In the spanwise direction, the forewings are stiffer on the dorsal side than on the ventral side, but the difference between dorsal and ventral stiffness is less than half of that seen in *Manduca* (Table 4.3,4.4).

Finite Element Modeling

Although the two finite element models have the same tip or trailing edge displacement in response to a point force, the distribution of flexural stiffness in the spanwise and chordwise direction is radically different in the two wings (Fig. 4.6). The flexural stiffness distribution of the exponential wing matches measured distributions in real *Manduca* wings fairly well (although the model has no dorsal/ventral asymmetry - see Discussion). The model with homogeneous vein and membrane regions has a nearly

constant stiffness in the spanwise direction and increasing stiffness in the chordwise direction (Fig. 4.6).

The effects of these differences are apparent in static tests on the model wings (Fig. 4.7). Although an applied point force results in the same tip displacement, bending in the exponential wing is localized to the outer third of the wing, while the homogeneous wing bends gradually along much of its span (Fig. 4.7A). When subjected to a pressure load, the homogeneous wing again bends along a large portion of its length, and its maximum displacement is nearly twice as large as the displacement of the exponential wing (Fig. 4.7B). In the exponential wing, displacement is localized to the tip and trailing edge of the wing, and bending is apparent in both the spanwise and chordwise directions (Fig. 4.7B).

The effects of an exponential decline in stiffness are further illustrated by dynamic tests on the models (Fig. 4.8; for a movie of the model wings in motion, see <http://faculty.washington.edu/danielt/movies>). The exponential wing bends considerably in the chordwise direction during the middle of the stroke, and bending in the spanwise direction is confined mainly to the outer portion of the wing (Fig. 4.8, left panels). In contrast, the homogeneous wing shows little chordwise bending and spanwise bending is largest near the base, while the outer portion of the wing remains somewhat rigid (Fig. 4.8, right panels).

Discussion

Flexural stiffness declines sharply from wing base to tip and from the leading to the trailing edge in the wings of both *Manduca sexta* and *Aeshna multicolor*.

Displacement in the spanwise and chordwise directions of these wings can be predicted fairly well when the stiffness distribution is approximated by an exponential equation. The observed similarities in flexural stiffness distribution in these two species (despite their dramatic differences in wing shape and venation pattern), suggest that a sharp decline in wing stiffness towards the tip and trailing edge may be a common pattern in many insect wings.

In addition, the wings of both species display a non-linear response to loading, where average stiffness increases in response to larger loads. This behavior could provide insect wings with an automatic control mechanism to resist excessive wing deformations during flight.

Comparisons of wing stiffness

The measurements of wing stiffness in male and female *Manduca sexta* suggest that the two sexes may differ in their patterns of chordwise flexural stiffness. Although the slight difference in wing size between males and females could have an effect on overall wing stiffness, it does not provide an explanation for the different patterns of chordwise stiffness seen in the two sexes; the wings of male *Manduca sexta* decline in stiffness far more sharply than those of females (as indicated by the more negative exponents). The functional significance of these differences is unclear; but other aspects

of *Manduca* wing morphology, such as the physical coupling of fore and hindwings also display sexual dimorphism (Eaton, 1988), which could be related to the higher wing loading measured in females carrying eggs (Willmott and Ellington, 1997b). The higher average stiffness and more gradual decline in chordwise flexural stiffness measured in females could potentially allow their wings to maintain the same level of performance as the wings of male moths despite higher wing loading, for example by providing similar chordwise deflections during flight.

The wings of both male and female *Manduca sexta* display a large dorsal/ventral difference, while those of *Aeshna multicolor* do not. Dorsal stiffness is greater than ventral stiffness in both directions of *Manduca* wings. In the spanwise direction, this difference is greatest near the base; Stepan (2000) found a similar dorsal/ventral asymmetry near the base of butterfly wings. Higher dorsal stiffness has also been found in the leading edge spar of locust hindwings (Wootton et al., 2000).

Although measurements of such bending asymmetry are rare, theoretical studies have suggested that insect wings might display dorsal/ventral stiffness asymmetry due to the camber inherent in most wings (Ennos, 1995; Ennos, 1997; Wootton, 1993). However, these arguments predict that wings should be stiffer to forces from the ventral (concave) side than from the dorsal (convex) side, contrary to what I observed. I therefore explored the effects of camber on bending asymmetry in both the finite element model of a *Manduca* wing (adding 5% spanwise and chordwise camber, as measured in real wings), and in a finite element model of a more strongly cambered beam attached at one end (Fig. 4.9).

In both models, the response to a point force applied at the tip in the dorsal or ventral direction was exactly the same (Fig. 4.9). Although the deformed shape was quite different depending on the direction of force application, the maximum displacement (as well as the magnitude of displacement at each point on the surface, i.e. green arrows in Fig. 4.9A) was identical in both cases. Maximum displacement due to a pressure load (Fig. 4.9B) or to an off-axis load resulting in torsion (not shown) was also symmetric. In a more dynamic situation (such as in flapping flight), camber may in fact lead to dorsal/ventral differences in wing deformation, but it does not seem to explain the large differences measured in this study for wings subjected to static point loading.

Although *Manduca* wings have none of the gross anatomical features often associated with bending asymmetry (i.e., a ventral flexion line), their veins may contain one-way hinges or other micro-structural features that facilitate asymmetric bending in other insect wings (Wootton, 1981; Wootton, 1992). In addition, the stress-stiffening effect explored by Kesel et al. (1998) in models of dipteran wings could potentially apply to *Manduca*. When unloaded, the membranes of *Manduca* wings lay rather loosely between the veins extending to the trailing edge. When a point force is applied to the dorsal side of the trailing edge (which is cambered downwards), it appears to pull the trailing edge veins apart. This should first remove any slack in the membrane, and might then increase the stiffness of the wing as force is applied to the already-taut membrane (the stress-stiffening effect). When a point force is applied to the ventral side of the trailing edge (which is cambered upwards), the veins are pushed together and the membranes between them become looser.

The direction of dorsal/ventral asymmetry measured in *Manduca* wings might at first seem counter-productive to force production, as lower ventral stiffness would suggest that the wings bends upwards during the powerful downstroke. However, tracings from high-speed video of hovering *Manduca sexta* show that the most dramatic wing deformations actually occur at stroke reversals, particularly during supination (Fig. 4.10; for a movie of a hovering hawkmoth, see <http://faculty.washington.edu/danielt/movies>).

The wings of many insects display torsional asymmetry, in which they supinate more easily than pronate (Ennos, 1988; Wootton, 1993). This pronounced supination is necessary to generate useful force on the upstroke, which is required for hovering flight (Wootton, 1990a). However, the coupling of fore and hindwings in *Manduca* may limit twisting at the wing base, which occurs in dipterans (Ennos, 1988) and other insects with uncoupled wings (such as odonates).

Although torsional stiffness was not measured in this study, bending and torsion are necessarily related. The torsion a *Manduca* wing undergoes during supination involves ventral bending (resulting in a ventrally convex surface- see Fig. 4.10), and thus would be facilitated by lower ventral stiffness. In contrast, the torsion and bending during pronation (which would involve dorsal bending) appear to be relatively small (Fig. 4.10, bottom and top panel).

Finite element modeling

The finite element models reveal that the distribution of flexural stiffness in wings is a critical in determining how wings bend. Despite undergoing the same tip deflections in response to a point force, the two model wings display radically different patterns of bending. The sharply declining stiffness measured in real wings (modeled as an exponential decline) localizes bending to the tip and trailing edge of the wing. This serves to maintain essential rigidity in the proximal portions of the wing (despite larger bending moments), and transfers bending to the distal edges of the wing, where aerodynamic force generation is most sensitive to subtle alterations in shape. In addition to these potential aerodynamic effects, lower stiffness at the wing tips may provide other advantages, including lowering inertial costs and reducing damage in collisions (Ennos, 1989; Wootton, 1992).

Concluding remarks

This study demonstrates that the distribution of flexural stiffness in the spanwise and chordwise direction of insect wings can be estimated by measuring local displacement and using a simple mathematical function to approximate local stiffness. Flexural stiffness in the wings of both *Manduca sexta* and *Aeshna multicolor* declines sharply from base to tip and from leading edge to trailing edge; this pattern of stiffness can be modeled as an exponential decline. Modeling stiffness distributions as simple mathematical functions allows comparisons within individuals (i.e. pronounced dorsal/ventral asymmetry in *Manduca*), within species (i.e. potential sexual dimorphism

in *Manduca*), and may ultimately allow comparisons between species, as more measurements are completed. Measurements of stiffness in the two species, as well as generalized finite element models, suggest mechanisms by which the structure of insect wings may automatically control wing deformations: non-linear behavior may help prevent excessive deformations, and a sharp decline in flexural stiffness towards the edges of wings (which appears to be preserved despite large changes in wing venation) may limit bending in core wing regions while enhancing bending in zones critical to aerodynamic control.

Acknowledgements

I would like to thank T. Daniel for his assistance in developing the method of estimating flexural stiffness from displacement and in troubleshooting the finite element models. A. Trimble was critical in devising the method of measuring displacement by a laser ranging technique and in developing Matlab code to analyze loaded and unloaded images. M. Tu and E. Goldman generously provided useful comments and nuggets of Matlab wisdom. J. Henry provided advice on collecting dragonflies and donated specimens to the study. J. Dierberger at MSC Software provided crucial troubleshooting of the FEM models without which the dynamic simulations would not have been possible. This work was supported by NSF grant 66-1822 to T. Daniel, the John D. and Catherine T. MacArthur Foundation, an NSF graduate fellowship to S. Combes, and an ARCS fellowship to S. Combes.

Notes to Chapter 4

- Batchelor, G. K. (1967). *An introduction to fluid dynamics*. Cambridge, UK: Cambridge University Press.
- Birch, J. M. and Dickinson, M. H. (2001). Spanwise flow and the attachment of the leading-edge vortex on insect wings. *Nature* **412**, 729-733.
- Combes, S.A. and Daniel, T.L. (2001). Shape, flapping and flexion: Wing and fin design for forward flight. *J. Exp. Biol.* **204**(12), 2073- 2085.
- Daniel, T. L. (1987). Forward flapping flight from flexible fins. *Can J. Zool.* **66**, 630-638.
- Dickinson, M. H., Lehman, F.-O., and Sane, S. P. (1999). Wing rotation and the aerodynamic basis of insect flight. *Science* **284**, 1954-1960.
- Eaton, J. L. (1988). *Lepidopteran Anatomy*. New York: John Wiley & Sons.
- Ellington, C. P. (1984a). The aerodynamics of hovering insect flight. I. The quasi-steady analysis. *Phil. Trans. R. Soc. Lond. B* **305**, 1-15.
- Ellington, C. P. (1984b). The aerodynamics of hovering insect flight. II. Morphological parameters. *Phil. Trans. R. Soc. Lond. B* **305**, 17-40.
- Ellington, C. P., Van den Berg, C., Willmott, A. P., and Thomas, A. L. R. (1996). Leading-edge vortices in insect flight. *Nature* **384**, 626-630.
- Ennos, A. R. (1988). The importance of torsion in the design of insect wings. *J. Exp. Biol.* **140**, 137-160.
- Ennos, A. R. (1989). Inertial and aerodynamic torques on the wings of Diptera in flight. *J. Exp. Biol.* **142**, 87-95.
- Ennos, A. R. (1995). Mechanical behavior in torsion of insect wings, blades of grass and other cambered structures. *Proc. R. Soc. Lond. B* **259**, 15-18.
- Ennos, A. R. (1997). Flexible structures in biology. *Comments Theor. Biol.* **4**(2-3), 133-149.
- Ennos, A. R. and Wootton, R. J. (1989). Functional wing morphology and aerodynamics of *Panorpa germanica* (Insecta: Mecoptera). *J. Exp. Biol.* **143**, 267-284.

- Gorb, S. N. (1999). Serial elastic elements in the damselfly wing: mobile vein joints contain resilin. *Naturwiss.* **86**, 552-555.
- Haas, F., Gorb, S., and Blickhan, R. (2000). The function of resilin in beetle wings. *Proc. R. Soc. Lond. B* **267**, 1375-1381.
- Haas, F., Gorb, S., and Wootton, R. J. (2000). Elastic joints in dermapteran hind wings: materials and wing folding. *Arthropod Structure & Development* **29**, 137-146.
- Herbert, R. C., Young, P. G., Smith, C. W., Wootton, R. J., and Evans, K. E. (2000). The hind wing of the desert locust (*Schistocerca gregaria* Forskål). III. A finite element analysis of a deployable structure. *J. Exp. Biol.* **203**, 2945-2955.
- Kesel, A. B., Philippi, U., and Nachtigall, W. (1998). Biomechanical aspects of the insect wing: an analysis using the finite element method. *Computers in Biol. and Med.* **28**, 423-437.
- Liu, H., Ellington, C. P., Kawachi, K., Van den Berg, C., and Willmott, A. P. (1998). A computational fluid dynamic study of hawkmoth hovering. *J. Exp. Biol.* **201**, 461-477.
- Sane, S. P. and Dickinson, M. H. (2002). The aerodynamic effects of wing rotation and a revised quasi-steady model of flapping flight. *J. Exp. Biol.* **205**, 1087-1096.
- Smith, C. W., Herbert, R., Wootton, R. J., and Evans, K. E. (2000). The hind wing of the desert locust (*Schistocerca gregaria* Forskål). II. Mechanical properties and functioning of the membrane. *J. Exp. Biol.* **203**, 2933-2943.
- Smith, M. J. C. (1996). Simulating moth wing aerodynamics: towards the development of flapping-wing technology. *AIAA Journal* **34**(7), 1348-1355.
- Smith, M. J. C., Wilkin, P. J., and Williams, M. H. (1996). The advantages of an unsteady panel method in modelling the aerodynamic forces on rigid flapping wings. *J. Exp. Biol.* **199**, 1073-1083.
- Somps, C. and Luttges, M. (1985). Dragonfly flight: novel uses of unsteady separated flows. *Science* **228**, 1326-1329
- Steppan, S. J. (2000). Flexural stiffness patterns of butterfly wings (Papilionoidea). *J. Res. Lepid.* **35**, 61-77.
- Sunada, S., Zeng, L., and Kawachi, K. (1998). The relationship between dragonfly wing structure and torsional deformation. *J. Theor. Biol.* **193**, 39-45.

- Vest, M. S. and Katz, J. (1996). Unsteady aerodynamic model of flapping wings. *AIAA Journal* **34**(7), 1435-1440.
- Wainwright, S. A., Biggs, W. D., Currey, J. D. and Gosline, J. M. (1982). *Mechanical Design in Organisms*. Princeton, New Jersey: Princeton University Press.
- Wakeling, J. M. and Ellington, C. P. (1997a). Dragonfly flight. I. Gliding flight and steady-state aerodynamic forces. *J. Exp. Biol.* **200**, 543-556.
- Wakeling, J. M. and Ellington, C. P. (1997b). Dragonfly flight. II. Velocities, accelerations and kinematics of flapping flight. *J. Exp. Biol.* **200**, 557-582.
- Wakeling, J. M. and Ellington, C. P. (1997c). Dragonfly flight. III. Lift and power requirements. *J. Exp. Biol.* **200**, 583-600.
- Wilkin, P. J. and Williams, M. H. (1993). Comparison of the aerodynamic forces on a flying sphingid moth with those predicted by quasi-steady theory. *Physiol. Zool.* **66**(6), 1015-1044.
- Willmott, A. P. and Ellington, C. P. (1997a). The mechanics of flight in the hawkmoth *Manduca sexta*. I. Kinematics of hovering and forward flight. *J. Exp. Biol.* **200**, 2705-2722.
- Willmott, A. P. and Ellington, C. P. (1997b). The mechanics of flight in the hawkmoth *Manduca sexta*. II. Aerodynamic consequences of kinematic and morphological variation. *J. Exp. Biol.* **200**, 2723-2745.
- Wootton, R. J. (1981). Support and deformability in insect wings. *J. Zool., Lond.* **193**, 447-468.
- Wootton, R. J. (1990a). The mechanical design of insect wings. *Scientific American* **Nov**, 114-120.
- Wootton, R. J. (1991). The functional morphology of the wings of Odonata. *Adv. Odonatol.* **5**, 153-169.
- Wootton, R. J. (1992). Functional morphology of insect wings. *Annu. Rev. Ent.* **37**, 113-140.
- Wootton, R. J. (1993). Leading edge section and asymmetric twisting in the wings of flying butterflies (Insecta, Papilionoidea). *J. Exp. Biol.* **180**, 105-117.
- Wootton, R. J. (1999). Invertebrate paraxial locomotory appendages: design, deformation and control. *J. Exp. Biol.* **202**, 3333-3345.

Wootton, R. J., Evans, K. E., Herbert, R., and Smith, C. W. (2000). The hind wing of the desert locust (*Schistocerca gregaria* Forskål). I. Functional morphology and mode of operation. *J. Exp. Biol.* **203**, 2921-2931.

Wu, T. Y. (1971). Hydromechanics of swimming propulsion. Part 1. Swimming of a two dimensional flexible plate at variable forward speeds in an inviscid fluid. *J. Fluid Mech.* **46**, 337-355.

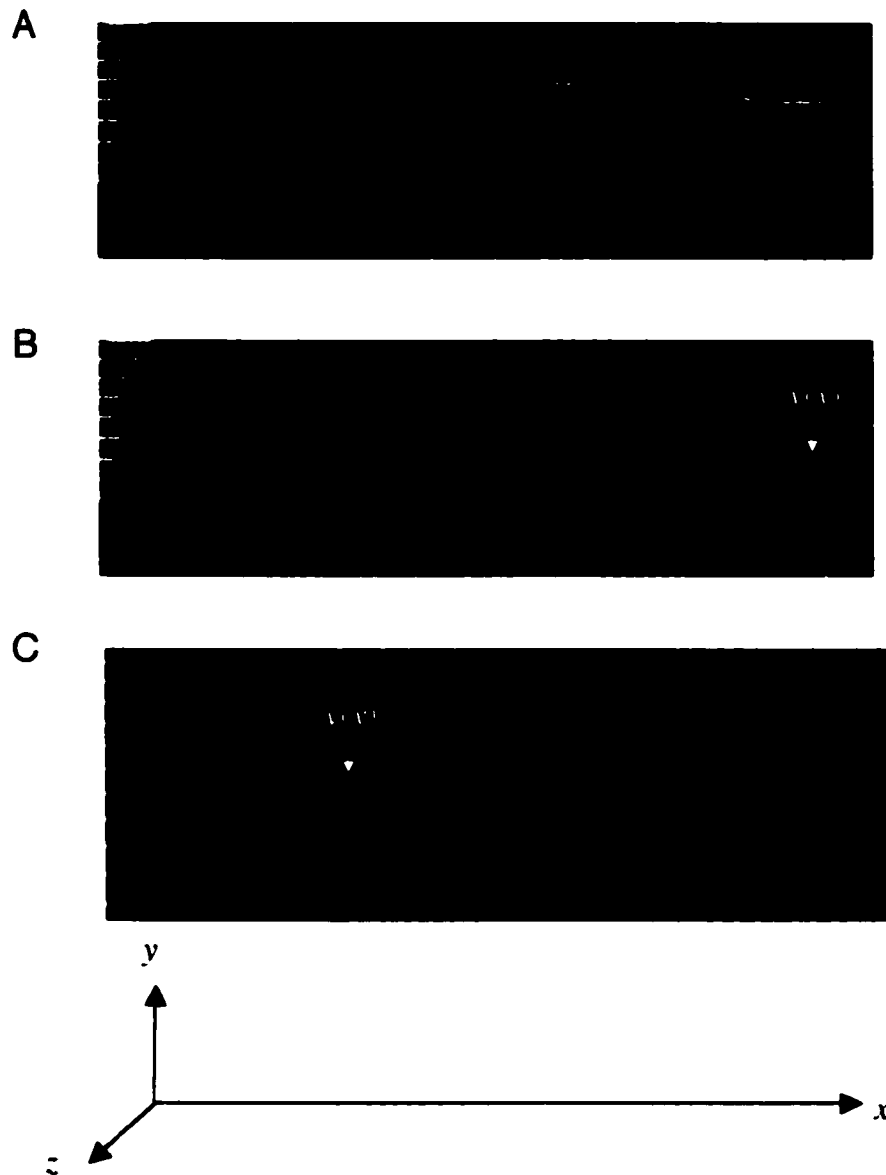


Fig. 4.1. *Manduca sexta* wing and calibration slide illuminated with laser lines. (A) Unloaded *Manduca sexta* wing illuminated with a laser. A Matlab program is used to find the center of a laser line running from the base of the wing to the tip (shown in yellow). (B) Loaded *Manduca sexta* wing illuminated with a laser. A point force is applied to the tip of the wing and the new position of the line is found (in red). The end positions of the lines are recorded (dotted lines) and the change in position of the laser line ($y(x)$) is used to find displacement of the wing in the z -axis ($\delta(x)$). (C) Calibration slide with steps of known height. Change in position of a laser line ($y(x)$) is used to determine the relationship between line position and height in the z -axis.

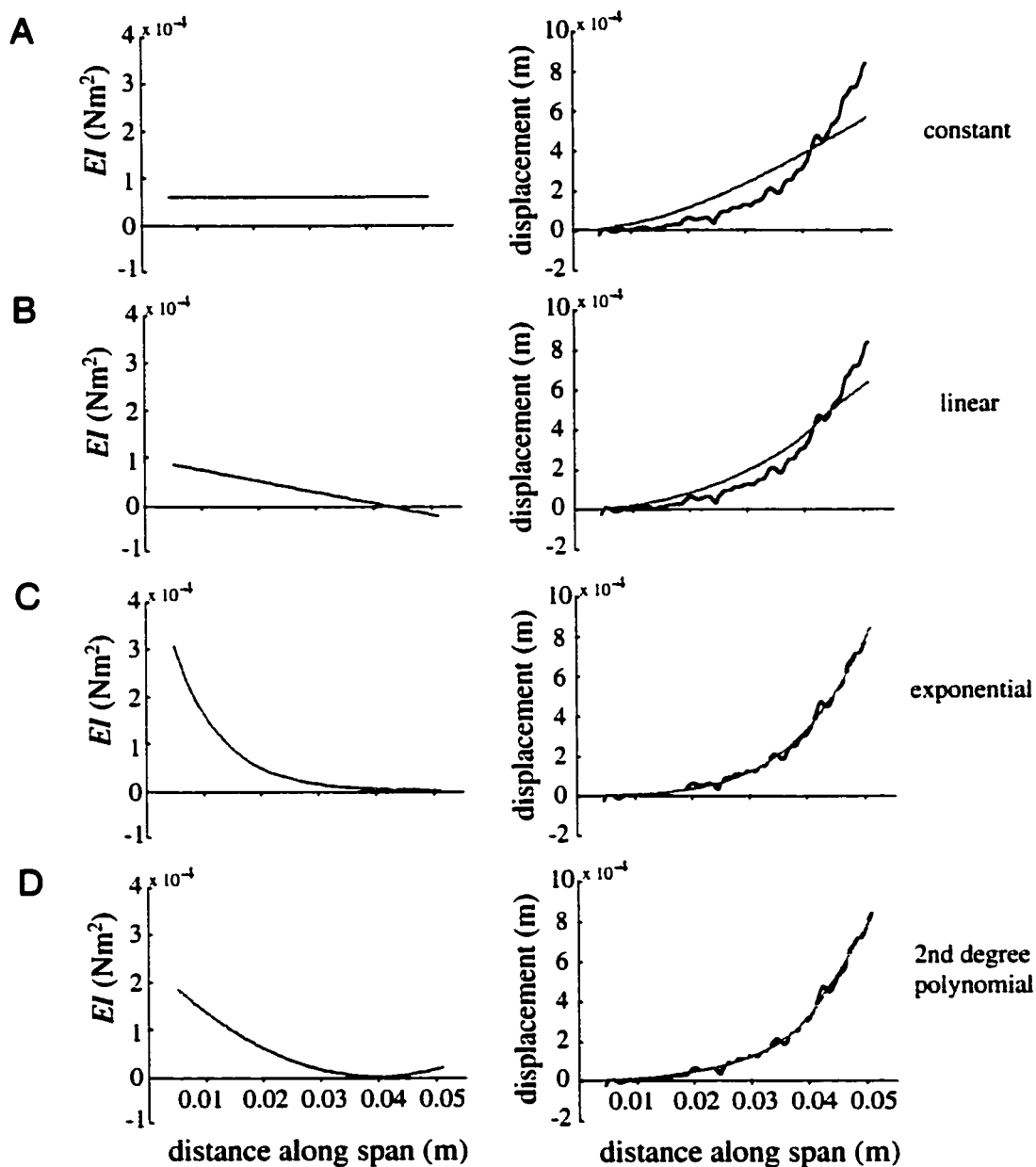


Fig. 4.2. Proposed distributions of flexural stiffness and predicted *versus* measured displacement in a *Manduca* wing. Proposed spanwise distributions are shown on left and predicted displacement due to a point force at the tip are shown on right (in gray). Predicted wing displacement is compared to actual displacement of a *Manduca sexta* wing (right, in black) for four possible approximations of the stiffness distribution: (A) constant along the span, (B) linear, (C) exponential, or (D) 2nd degree polynomial. Simplex minimization was used to find the parameter values of each equation that produced the best fit between actual and predicted displacement; panels on the left show the best approximation of wing stiffness for each stiffness distribution.

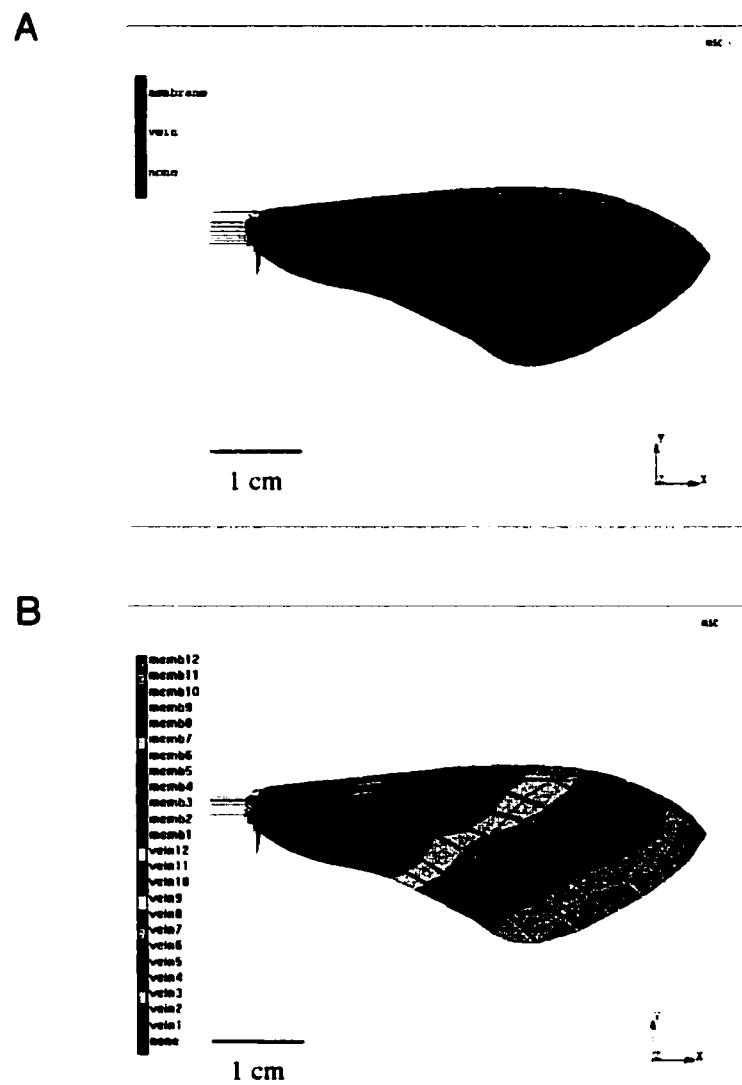


Fig. 4.3. Finite element models of *Manduca* wings. (A) Model of a *Manduca* wing with membranes (blue) and veins (pink) each of homogeneous material stiffness (Young's modulus). (B) Model of a *Manduca* wing in which declining material stiffness of membranes (memb 1-12) and veins (vein 1-12) results in an exponential decline in flexural stiffness. Each color represents a different value of Young's modulus (see text for range of values).

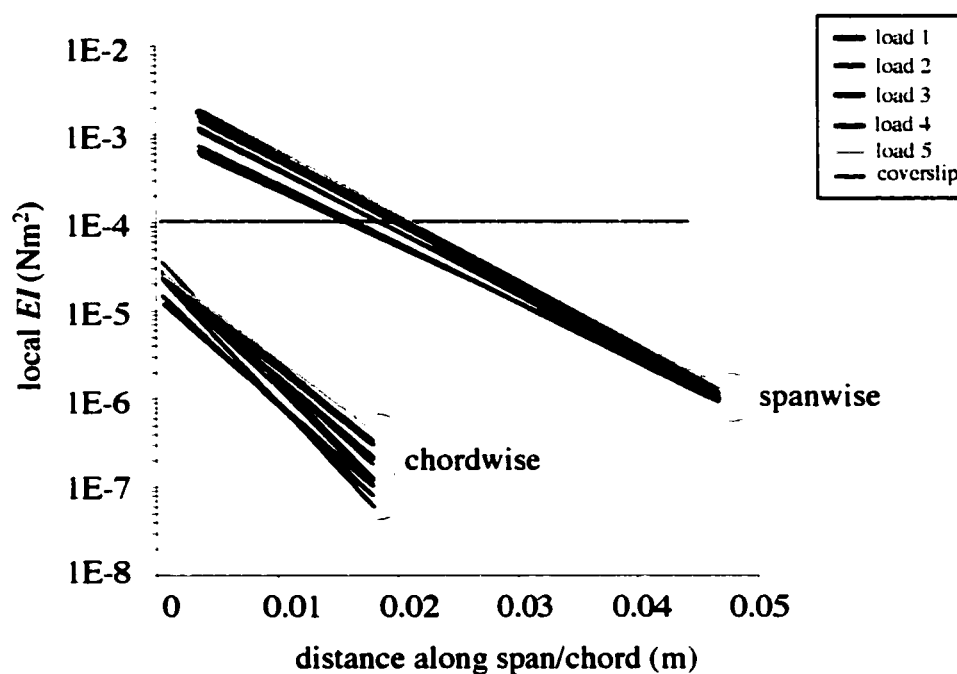


Fig. 4.4. Local flexural stiffness of a single *Manduca* wing subjected to repeated loads. Each line represents a large series of points (from several hundred to several thousand) measured on the wing. Flexural stiffness declines exponentially in both the spanwise and chordwise directions, and varies with the magnitude of the applied force. Point loads of varying strength were applied to the dorsal surface at the wing tip (spanwise) or trailing edge (chordwise). Tip deflections varied from approximately 1.8% of wing span (load 1) to 7.1% span (load 5) and trailing edge deflections varied from 4.4% chord length (load 1) to 15% chord length (load 5). Loads were applied in random order and each load was repeated three times. Local flexural stiffness of a glass coverslip (with constant geometry and homogeneous material properties) was measured as a control.

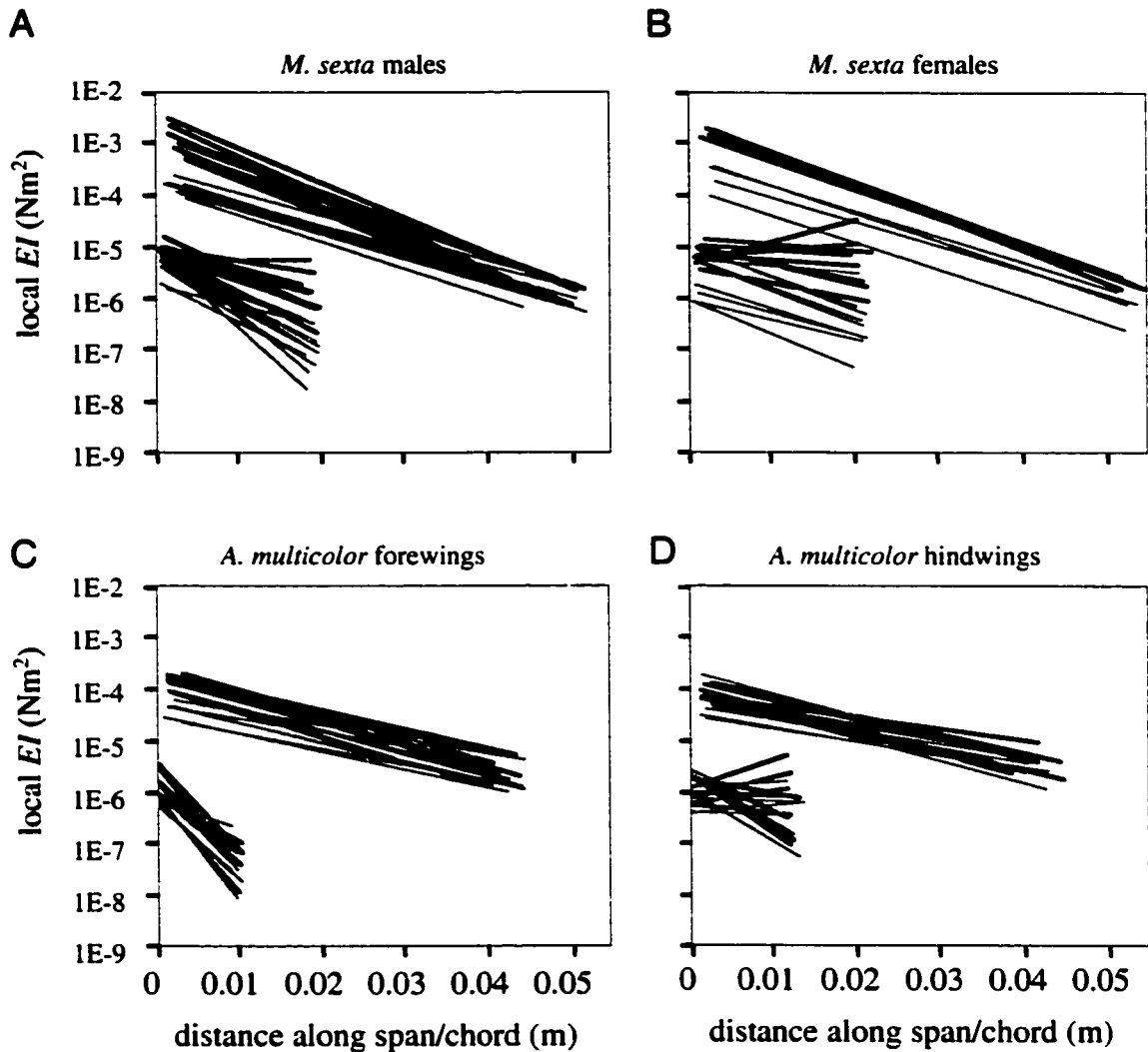


Fig. 4.5. Local flexural stiffness in wings of *Manduca sexta* and *Aeshna multicolor*. In each graph, spanwise stiffness is shown above (longer lines) and chordwise stiffness below. Each line represents a large series of points (from several hundred to several thousand) measured on a wing. Spanwise stiffness is shown for a tip deflection of 5% wing span and chordwise stiffness for a trailing edge deflection of 8% chord length in all individuals; dorsal stiffness is in black and ventral stiffness in grey. (A) Local flexural stiffness of male *Manduca sexta* forewings ($n = 9$ spanwise, $n = 10$ chordwise). (B) Local flexural stiffness of female *Manduca sexta* forewings ($n = 4$ spanwise, $n = 9$ chordwise). (C) Local flexural stiffness of male *Aeshna multicolor* forewings ($n = 8$). (D) Local flexural stiffness of male *Aeshna multicolor* hindwings ($n = 8$).

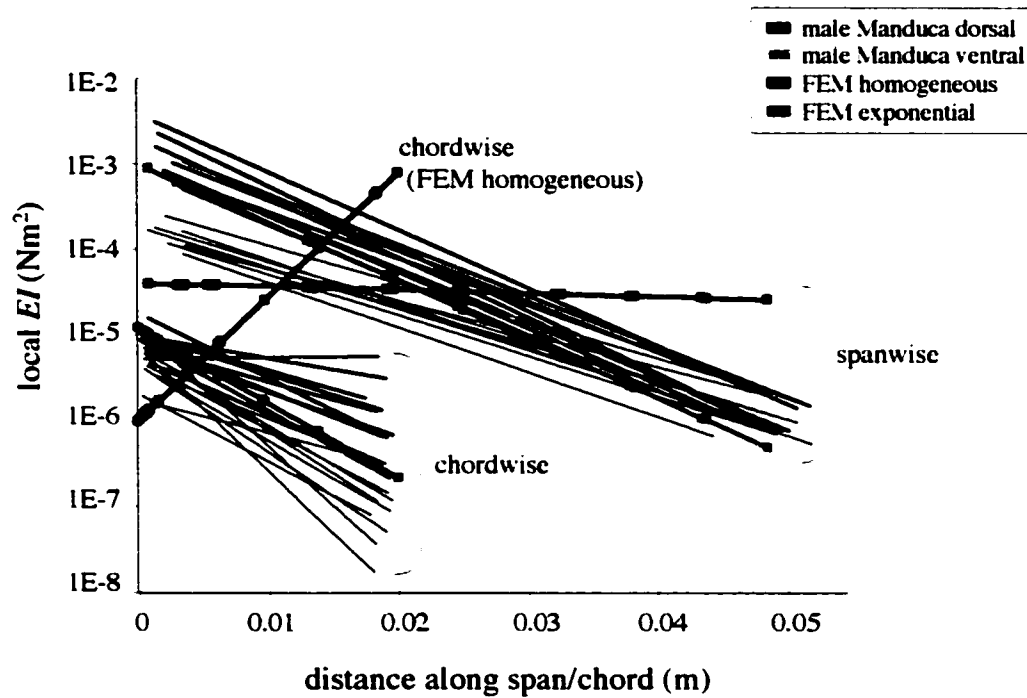


Fig. 4.6. Comparison of local flexural stiffness in finite element model (FEM) and real *Manduca* wings. Local stiffness in male *Manduca* wings is shown in black and gray as in Fig 4.5a. FEM wings are fixed at the base (or leading edge) while a point force is applied to the tip (or trailing edge). Calculated displacement at nodes along the span or chord is used to estimate the distribution of EI with the Matlab simplex minimization program used for real wings.

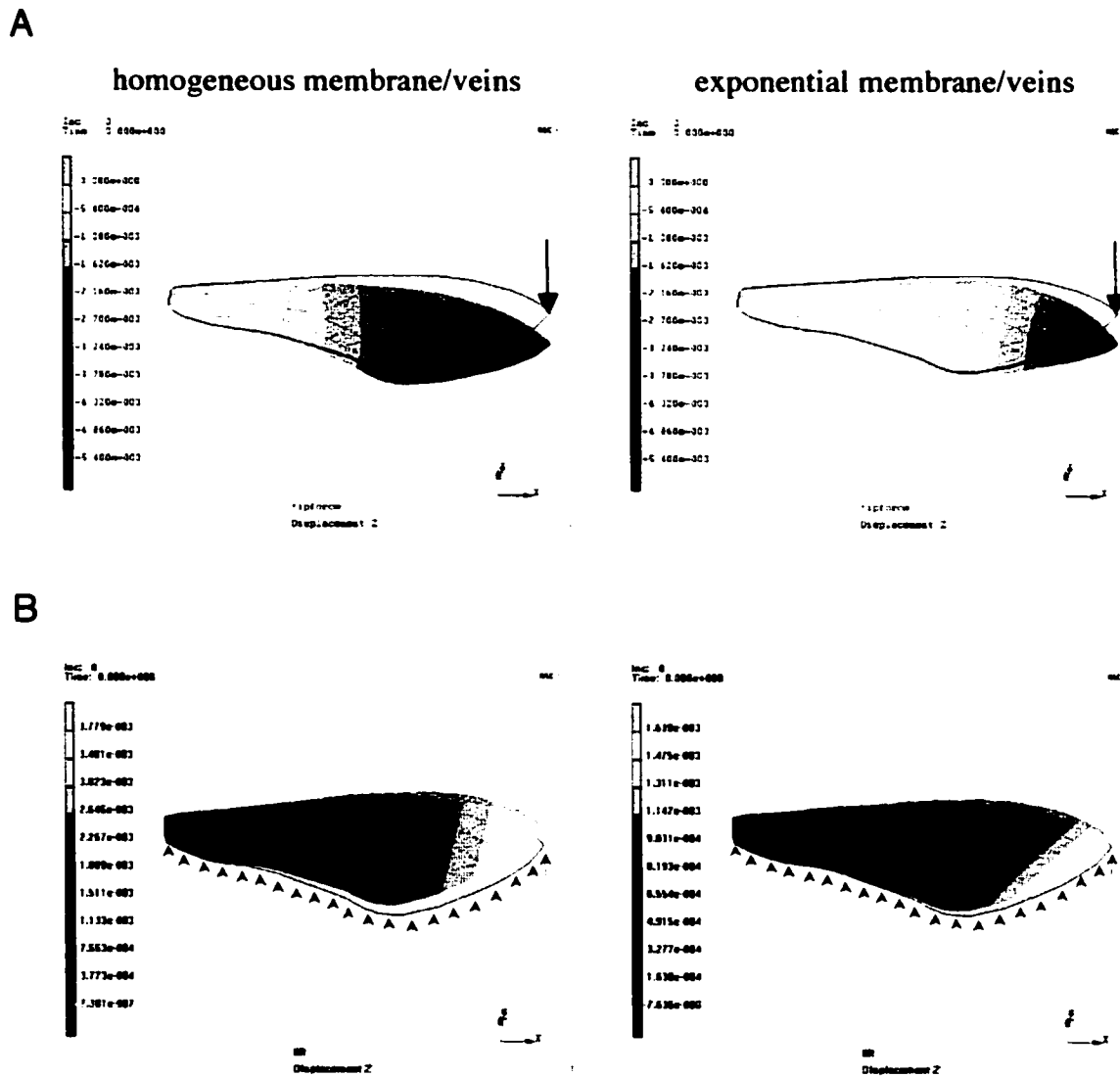


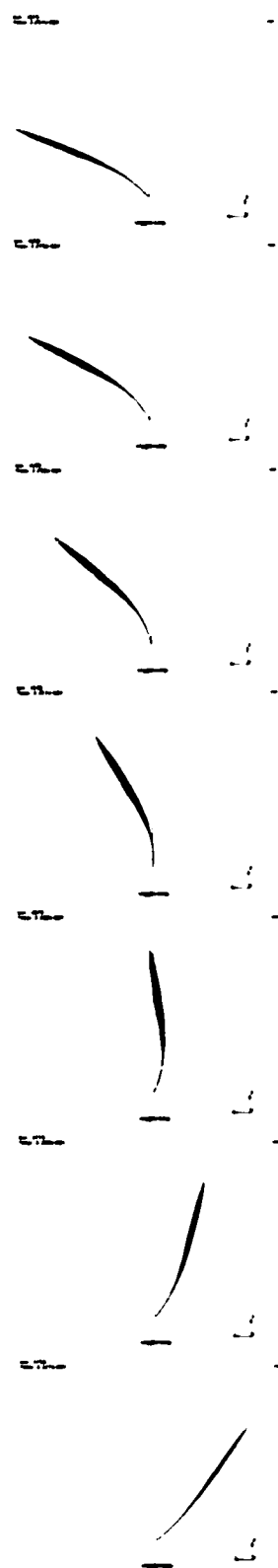
Fig. 4.7. Results of static loading tests on FEM wings. Wings are fixed at the base; displacement from original position (black outline) in the z-direction is shown (in meters). FEM wing with homogeneous membrane/veins is shown on the left and wing with exponential membrane/veins is shown on the right. (A) Displacement due to a point force of 0.005 N (green arrow) at the wing tip. Note that displacement at the tip is the same in both models. (B) Displacement due to a normal face load of -14.43 Pa (green arrows), the approximate pressure on a wing during steady flight (for a moth with a total mass of 1.882 g, the pressure on one wing is 1/2 body weight divided by the area of one wing ($6.4 \times 10^{-4} \text{ m}^2$)). Note that maximum displacement in the homogeneous wing is nearly twice as large as in the exponential wing.

Fig. 4.8. Sequence of images from flapping FEM wings. Wing is moving to the right, viewed from its leading edge; time steps proceed down the page. Wings are shown at the same time steps. The center of the stroke plane is shown with a straight line. (A) FEM wing with exponentially declining membrane and vein stiffness. (B) FEM wing with homogeneous membrane and vein stiffness.

A



B



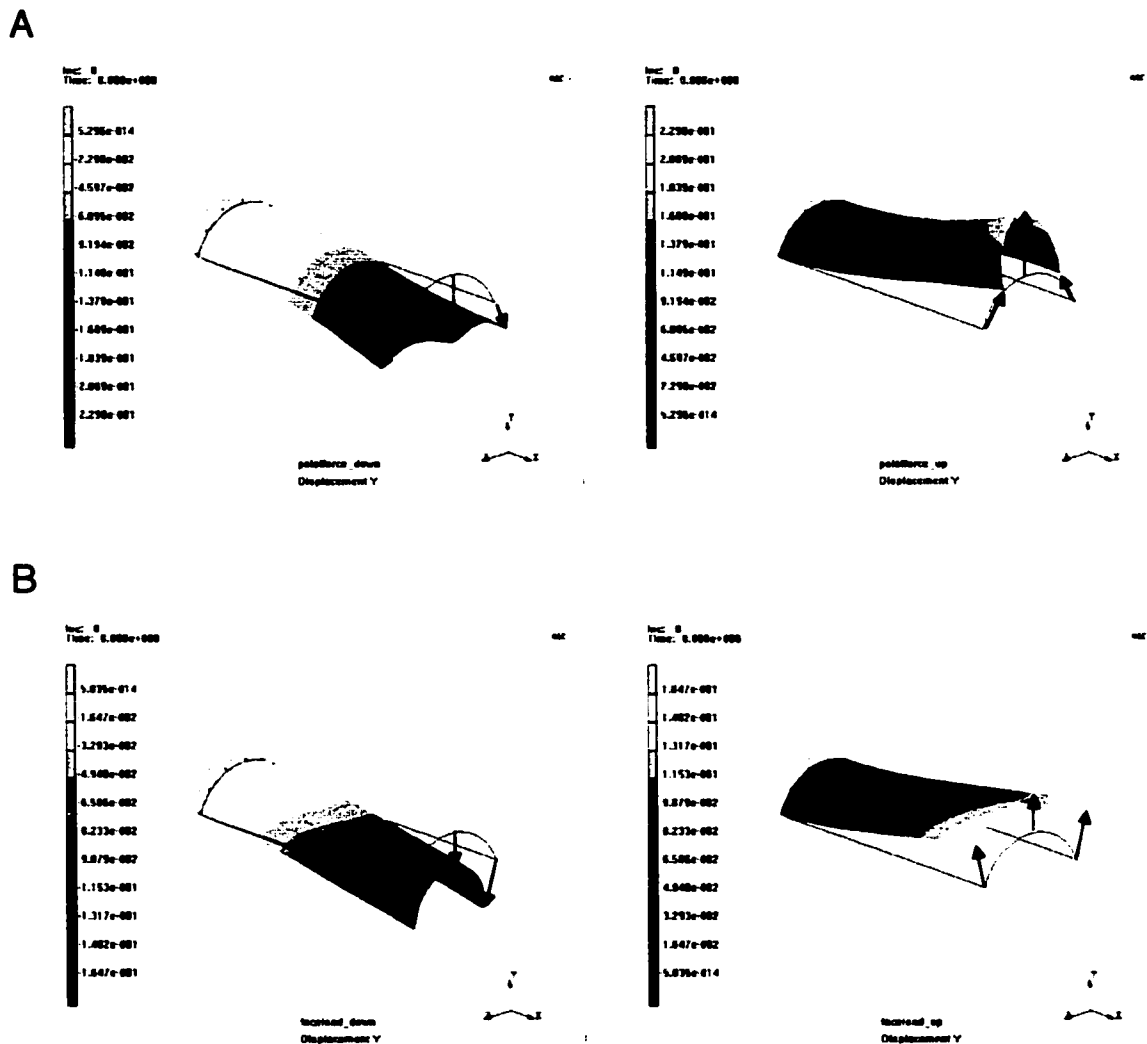


Fig. 4.9. Results of bending tests on a finite element model of a cambered plate. The plate is fixed at the left side (brown arrows), and displacement from the original position (black outline) is shown. (A) Bending due to a point force applied at the center of the tip. Note that the magnitude of displacement at each point on the surface (i.e. green arrows) is the same whether the force is applied to the convex side (left panel) or the concave side (right panel). (B) Bending due to a normal face load applied on the convex side (left panel) or concave side (right panel). The magnitude of displacement at each point on the surface is the same in each case.

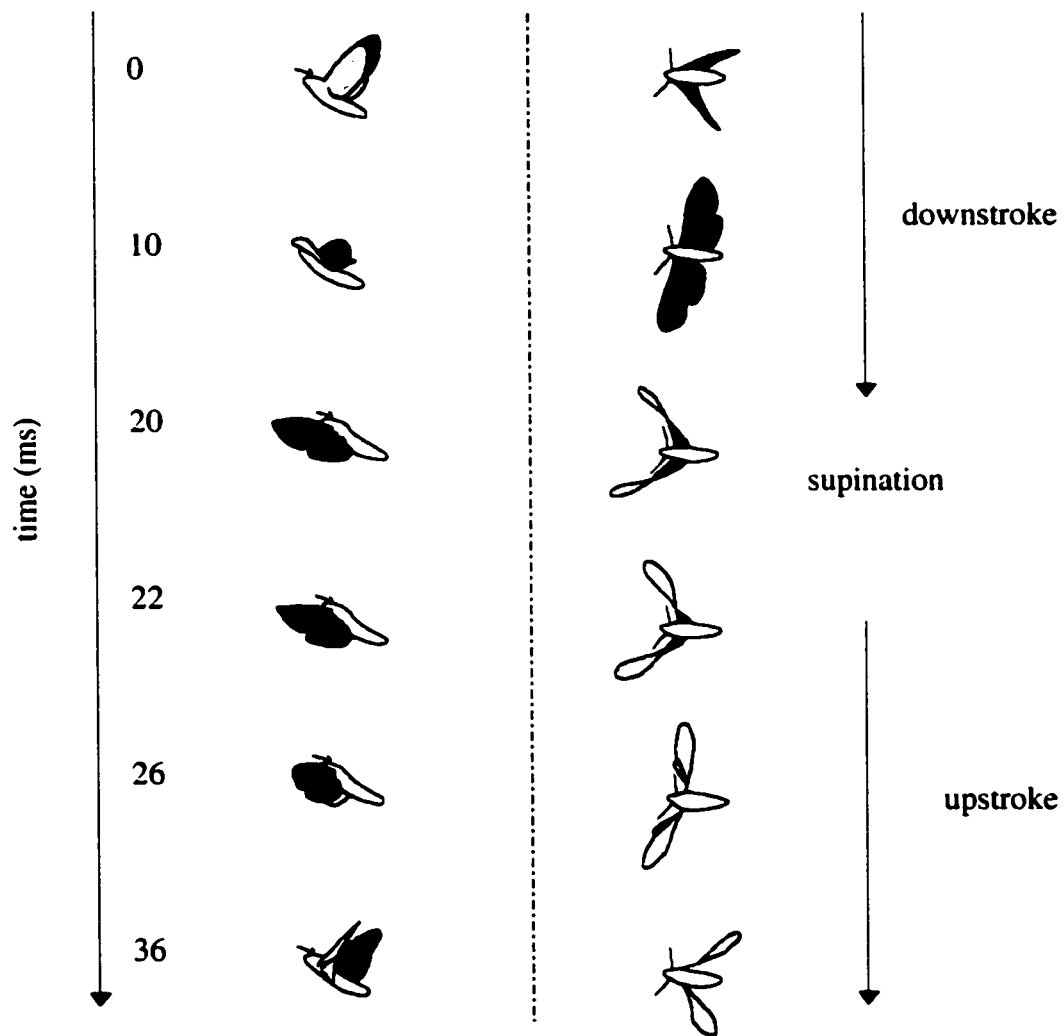


Fig. 4.10. Sketches of *Manduca sexta* hovering freely while feeding at an artificial flower. Images are drawn from high-speed footage (500 frames/sec) from two cameras; lateral view is shown on left and dorsal view on right. Dorsal surface of the wing is shown in dark gray and ventral surface in light gray.

Table 4.1. One sample sign test on slopes of \overline{EI} versus strain. Significant values are shown in bold type.

		p-value	n	n > 0
<i>Manduca sexta</i> forewing	spanwise dorsal	0.2668	13	9
	spanwise ventral	0.0005	12	12
	chordwise dorsal	0.0007	19	17
	chordwise ventral	0.0044	19	16
<i>Aeshna multicolor</i> forewing	spanwise dorsal	0.0078	8	8
	spanwise ventral	0.0078	8	8
	chordwise dorsal	0.0078	8	8
	chordwise ventral	0.0078	8	8
<i>Aeshna multicolor</i> hindwing	spanwise dorsal	0.0078	8	8
	spanwise ventral	0.0078	8	8
	chordwise dorsal	0.0156	7	7
	chordwise ventral	0.0703	8	7

Table 4.2. Morphological measurements of *Manduca sexta* and *Aeshna multicolor*.

	individual	wing area (cm ²)	span (cm)	chord (cm)	body mass (g)	wing mass (g)
<i>Manduca sexta</i>	M1	7.55	5.21	2.01	2.310	0.0440
	M2	7.00	4.96	1.93	2.284	0.0425
	M3	7.19	4.99	1.99	2.207	0.0425
	M4	6.51	4.58	1.89	1.882	0.0350
	M5	7.81	5.04	2.10	1.948	0.0425
	M6	7.32	5.25	2.07		
	M7	6.71	4.99	1.96	1.929	0.0375
	F1	8.66	5.35	2.21	2.610	0.0485
	F2	7.78	5.26	2.04	2.756	0.0480
	F3	8.31	5.33	2.16	2.640	0.0490
	F4	8.12	5.34	2.12	2.565	0.0425
	F5	8.00	5.65	2.27		
	F6	8.65	5.54	2.25	2.774	0.0520
	F7	8.77	5.64	2.27	2.437	0.0475
<i>Aeshna multicolor</i> forewing	D1	3.61	4.22	1.02	0.575	0.0070
	D2	4.06	4.52	1.07	0.619	0.0085
	D3	4.06	4.52	1.07	0.698	0.0100
	D4	4.06	4.57	1.07	0.665	0.0075
	D5	4.00	4.47	1.07	0.683	0.0075
	D6	4.45	4.75	1.09	0.733	0.0085
	D7	4.39	4.72	1.09	0.715	0.0080
	D8	4.32	4.70	1.09	0.763	0.0080
hindwing	D1	4.52	4.01	1.30	0.575	0.0095
	D2	5.03	4.29	1.35	0.619	0.0080
	D3	4.97	4.37	1.32	0.698	0.0150
	D4	4.97	4.29	1.32	0.665	0.0110
	D5	4.90	4.24	1.30	0.683	0.0095
	D6	5.61	4.55	1.42	0.733	0.0105
	D7	5.61	4.57	1.40	0.715	0.0095
	D8	5.42	4.45	1.42	0.763	0.0095

Table 4.3. \overline{EI} and flexural stiffness exponents of *Manduca sexta*. M indicates male moths and F female moths. Spanwise values are calculated at a tip displacement of 0.05 span and chordwise values at a trailing edge displacement of 0.08 chord.

ID	span dors \overline{EI} (x10 ⁻⁴)	span vent \overline{EI} (x 10 ⁻⁴)	span dors exp	span vent exp	chord dors \overline{EI} (x 10 ⁻⁶)	chord vent \overline{EI} (x 10 ⁻⁶)	chord dors exp	chord vent exp
M1	3.834	0.298	-156.2	-109.5	2.248	0.619	-192.5	-183.0
M2	0.847	0.208	-144.4	-108.9	1.592	1.420	-149.6	-227.2
M3	1.394	0.250	-135.9	-117.4	3.093	0.879	-140.6	-235.5
M4	0.709	0.155	-147.1	-119.7				
M5	0.772	0.242	-124.0	-87.5	2.401	1.357	-120.5	-209.7
M6	2.004	0.329	-160.5	-104.8	3.220	1.871	-96.1	-317.7
M7	1.174		-152.0		4.740	1.185	-100.5	-336.4
M8	2.785	0.465	-167.4	-100.2	5.464	1.160	-58.7	-185.2
M9	1.496	0.203	-136.0	-100.8	3.928	1.274	-110.8	-134.0
M10					5.216	0.935	2.9	-87.9
M11					4.282	0.899	-174.1	-202.7
F1	1.910	0.585	-127.0	-113.9	5.384	0.390	-22.6	-86.3
F2	2.201	0.542	-129.8	-124.8	8.892	1.425	-21.6	-143.1
F3	2.695	0.307	-136.0	-107.6	4.300	1.794	-73.8	-135.7
F4	2.335	0.151	-145.3	-120.4	8.538	0.255	30.5	-152.4
F5					15.710	0.511	101.0	-99.5
F6					2.940	1.877	-70.7	-133.0
F7					4.358	2.489	-87.4	-146.0
F8					8.292	2.807	-12.3	-31.1
F9					3.918	1.236	-28.4	-117.3

Table 4.4. \overline{EI} and flexural stiffness exponents of *Aeshna multicolor*. F indicates forewing and H hindwing of same individual. Spanwise values are calculated at a tip displacement of 0.05 span and chordwise values at a trailing edge displacement of 0.08 chord.

ID	span dors \overline{EI} (x10 ⁻⁵)	span vent \overline{EI} (x 10 ⁻⁵)	span dors exp	span vent exp	chord dors \overline{EI} (x 10 ⁻⁷)	chord vent \overline{EI} (x 10 ⁻⁷)	chord dors exp	chord vent exp
F1	1.993	1.672	-110.3	-60.7	7.098	1.305	-460.2	-481.2
F2	3.315	2.067	-102.4	-95.9	7.716	3.491	-487.5	-392.8
F3	3.655	0.742	-99.4	-79.8	4.846	2.878	-329.5	-264.7
F4	4.215	0.596	-106.2	-69.4	7.466	1.689	-470.4	-325.6
F5	3.335	0.623	-99.0	-91.0	1.708	3.928	-440.3	-397.0
F6	3.750	1.128	-78.9	-85.2	2.803	3.908	-316.1	-120.6
F7	4.795		-84.1	-62.2	3.296	1.595	-197.2	-412.8
F8	3.735	2.078	-104.5	-99.1	8.284	1.620	-388.4	-346.5
H1	2.350	1.133	-98.5	-62.8	5.634	9.270	-254.5	-168.4
H2	1.905	2.145	-87.2	-93.0	6.632	7.492	-236.9	-218.2
H3	2.830	1.481	-50.8	-55.5	4.809	13.812	-38.2	22.4
H4	2.291	1.303	-63.8	-64.4	12.076	10.666	91.2	-181.8
H5	1.426	1.534	-79.6	-81.6	7.191	3.670	58.9	-13.4
H6	3.395	1.452	-83.5	-98.9			127.5	35.3
H7	2.011	4.440	-89.9	-98.9	8.280	3.036	-13.8	-221.9
H8	3.180	0.920	-85.9	-56.9	11.800	6.892	-69.3	-13.5

Table 4.5. Mann-Whitney U-test on male *versus* female *Manduca sexta* traits. Significant values are shown in bold type.

		p-value	n (male)	n (female)
Morphological traits:	wing area	0.0027	7	7
	wing span	0.0017	7	7
	chord length	0.0040	7	7
	body mass	0.0039	6	6
	wing mass	0.0115	6	6
	aspect ratio	0.9461	7	7
	wing loading	0.2623	6	6
Wing stiffness:	spanwise dorsal \overline{EI}	0.1649	9	4
	spanwise dorsal exponent	0.1649	9	4
	spanwise ventral \overline{EI}	0.3082	8	4
	spanwise ventral exponent	0.0894	8	4
	chordwise dorsal \overline{EI}	0.0209	10	8
	chordwise dorsal exponent	0.0059	10	8
	chordwise ventral \overline{EI}	0.4772	10	8
	chordwise ventral exponent	0.0077	10	8

Table 4.6. Wilcoxon signed rank test on dorsal *versus* ventral wing stiffness. Significant values are shown in bold type.

		p-value	n
<i>Manduca sexta</i> forewing	spanwise \overline{EI}	0.0022	12
	spanwise exponent	0.0022	12
	chordwise \overline{EI}	0.0001	19
	chordwise exponent	0.0002	19
<i>Aeshna multicolor</i> forewing	spanwise \overline{EI}	0.0180	7
	spanwise exponent	0.0251	8
	chordwise \overline{EI}	0.0687	8
	chordwise exponent	0.2076	8
<i>Aeshna multicolor</i> hindwing	spanwise \overline{EI}	0.3270	8
	spanwise exponent	0.6744	8
	chordwise \overline{EI}	0.7353	7
	chordwise exponent	0.3270	8

Chapter 5

Contributions of inertial and aerodynamic forces to wing bending in *Manduca sexta*

Summary

During flapping flight, insect wings deform in response to the dynamic forces acting upon them. Although the three-dimensional shape of flapping wings can have a large effect on force production, few models of insect flight incorporate passive wing flexibility, in part because the precise forces that determine wing bending are unknown. Flapping wings must withstand both fluid-dynamic forces as well as inertial-elastic forces generated by the rapid acceleration and deceleration of their own mass. Although many theoretical studies suggest that inertial forces are larger than aerodynamic forces in flapping insect wings, the relative importance of these forces in determining wing deformations is unclear. In this study, I use an experimental approach to examine the contributions of aerodynamic and inertial-elastic forces to wing bending in the hawkmoth *Manduca sexta*. I rotate fresh *Manduca* wings at realistic flight frequencies and amplitudes and compare wing bending in normal air *versus* helium (~15% air density), in which the contribution of fluid-dynamic forces to wing deformations should be significantly reduced. I find that an 85% reduction in air density produces only slight changes in the pattern of *Manduca* wing deformations, suggesting that fluid-dynamic forces have a relatively minor effect on wing bending. I then use a simplified finite element model of a *Manduca* wing to recreate the motions of wings. I find that a damped finite element model (with no fluid-dynamic forces included) may be able to predict

overall patterns of wing deformation independent of calculations of aerodynamic force production. These predicted shape changes could then be incorporated into models of insect flight to assess the effects of wing flexibility on flight performance.

Key words: insect flight, wing flexibility, wing bending, aerodynamic forces, inertial forces, finite element model, *Manduca sexta*

Introduction

Insect wings are flexible structures that bend and twist during flight. These three-dimensional shape changes can have dramatic effects on force production. For example, increasing the chordwise camber of a wing by only 10 degrees can lead to a five-fold increase in lift (Batchelor, 1967), and waves of bending (which are commonly seen in insects; Ellington, 1984c) can have dramatic effects on thrust production and aerodynamic efficiency (Wu, 1971; Daniel, 1987; Combes and Daniel, 2001 - see Chapter 1). In addition, wing flexibility may increase maneuverability (as suggested in aquatic animals, Fish, 1999; Walker, 2000) or enhance passive stability (Sneyd et al., 1982).

A model of insect flight that incorporates passive wing deformations would allow us to examine the effects of wing flexibility on many different aspects of insect flight performance. To predict deformations, this type of model would require a knowledge of both the structural properties of the wing as well as the forces that act on the wing to cause deformations. Overall structural and material properties of some insect wings are

now available (see Chapters 3 and 4), but the forces responsible for wing deformations during flight remain unknown.

During flight, wings generate aerodynamic forces (pressure stresses due to the movement of fluid) that provide the lift and thrust necessary for flight. In fixed-wing aircraft and in gliding birds, these aerodynamic forces cause wings to bend up noticeably at their tips (i.e. the wing tips of a B-52 bomber can rise 32 feet from their resting position during flight; Bisplinghoff and Ashley, 1975). Flapping animal wings also experience inertial-elastic forces due to oscillations of the mass of the wing. Although insect wings are small and light, they are accelerated and decelerated anywhere from 10 to over 1000 times per second, suggesting that inertial-elastic forces may be large enough to play a role in wing bending.

If the effects of fluid-dynamic forces on wing bending are small relative to the effects of inertial-elastic forces, predictions of the three-dimensional shape of insect wings could be made from the kinematics, mass distribution and stiffness distribution of the wing, prior to calculations of aerodynamic force production. On the other hand, if fluid-dynamic forces are important in determining dynamic wing shape, predictions of wing shape would have to be coupled (in each time step) to calculations of the fluid forces generated by these shapes.

This coupled problem has been addressed by those studying aeroelastic interactions in airplane design (particularly the aeroelastic "flutter" that was at one time common in airplane wings; Bisplinghoff and Ashley, 1975). The study of aeroelasticity has become an entire discipline and presents an extremely challenging problem, even in

man-made structures with fixed wings and known forces. Aeroelastic effects in insect wings would depend not only on the stiffness distribution and motions of the wing, but also on the temporal and spatial patterns of aerodynamic forces acting on the wing. These forces cannot be measured with current technology, but the time-dependent vortical structures produced by flapping wings (Ellington et al., 1996; Liu et al., 1998; Liu and Kawachi, 1998) suggest that the pattern of aerodynamic forces acting on wings may be very complex, and determining these forces would be a challenge in itself.

The difficulties presented by an aeroelastic analysis of insect flight have undoubtedly hindered the study of passive wing flexibility and its effects on flight performance. However, if inertial-elastic forces dominate wing bending, we may be able to predict the dynamic shape of flapping wings without solving the coupled aeroelastic problem or determining the temporal and spatial patterns of forces acting on the wing. This predicted dynamic wing shape could then be used in a variety of fluid-dynamic models to assess its effects on aerodynamic force production, (for example, Daniel and Combes, in prep.)

Several studies have estimated the magnitudes of inertial and aerodynamic forces in insect flight to calculate total power (Ellington, 1984f; Lehmann and Dickinson, 1997; Wakeling and Ellington, 1997c) or to separate the aerodynamic and inertial portions of force measurements on flying insects (Zanker and Gotz, 1990; Wilkin and Williams, 1993). In most cases, the contribution of wing inertia is estimated to be higher than the contribution of aerodynamic forces, sometimes by a factor of more than 30 (Ellington, 1984f). Wing inertia thus may play an important role in wing bending, but we still lack a

basic understanding of how the mass of the wing and the fluid it moves through contribute to the patterns of bending observed in insect wings.

In this study, I use an experimental approach to examine the relative contributions of inertial-elastic and fluid-dynamic forces to wing bending. I attach fresh *Manduca sexta* wings to an oscillator and rotate them at realistic flight frequencies and amplitudes. I film wings rotating in normal air and in helium (~15% air density); the lower density of helium should substantially reduce the contribution of fluid-dynamic forces to the observed wing deformations.

I then recreate the motions of real wings with a simplified finite element model of a *Manduca* wing. The model does not include any fluid-dynamic forces and thus predicts patterns of wing bending due solely to structural features and inertial-elastic effects. I compare patterns of bending in the model with bending measured in real *Manduca* wings.

Materials and Methods

Dynamic bending experiments

For dynamic bending tests, I used wings from *Manduca sexta* raised in a colony at the University of Washington (see Discussion for an analysis of how the size and weight of insect wings may affect wing bending). I anaesthetized moths by placing them in the freezer for 1 to 5 minutes. I then removed one forewing at the base and recorded wing and body weight. I marked three spots on the wing (on both the dorsal and ventral sides) with a small dot of reflective white paint: the wing tip, the trailing edge (where

chord length is maximum, approximately 50% wing span) and the leading edge (at the same spanwise position). I used cyanoacrylate glue and baking soda to attach the base of the wing to a brass rod extending from an oscillator. The oscillator (pen motor of a Gould chart recorder using the existing Gould amplifier) is capable of high-frequency motions in one axis, and was modified to rotate a brass rod with a wing attached (Fig. 5.1).

I fixed the oscillator to a platform inside a 30-cm Plexiglass cube (with 1-cm thick walls) and controlled its motions with a function generator. I rotated wings sinusoidally through a total amplitude of approximately 110° (see Table 5.1) at room temperature. I recorded wing motions with two high-speed video cameras (Redlake Inc.) filming at 1000 frames per second, one from above (viewing the wing from its leading edge) and the other from the front (viewing the wing from its tip).

I filmed each wing rotating at approximately 0.5 Hz (as a calibration for the shape and position of the wing when no dynamic bending occurs) and at approximately 26 Hz, which is close to the normal flight frequency of *Manduca* (see Table 5.1). I then lowered the density of fluid inside the chamber by repeatedly removing air and adding helium. I used a vacuum pump with a pressure transducer attached to remove approximately 50% of the air from an opening near the bottom of the box and replaced that air with pure helium from an opening near the top of the box (Fig. 5.1). I repeated this process five times (which results in ~97% of the air inside the box being replaced with helium). I then filmed the wing rotating at 26 Hz in helium, which has a density of 0.164 g/l (approximately 14% of normal air density; CRC, 2001). Finally, I opened the lid of the

box to release the helium and filmed the wing rotating again at 26 Hz in normal air (as a control for wing damage). I completed all filming within one hour to prevent the wing from stiffening.

Wing bending analysis

For each wing, I analyzed video sequences of the calibration (0.5 Hz) and experimental (26 Hz) rotations in normal air and in helium. I analyzed video frames from three complete rotation cycles in the middle of each filming sequence. I found the coordinates of the wing tip, leading edge and trailing edge in each frame (Fig. 5.2) using a Matlab program (PointNClick2, provided by M. S. Tu) and converted the coordinates to centimeters using images of 2-cm grids from each camera. I converted the three-dimensional Cartesian coordinates to spherical coordinates in Matlab, using the base of the wing as the origin and measuring the rotation of the wing (viewed from above) in degrees (with zero degrees at the center of the rotation).

Because the settings on the function generator provide only approximate measures of wing motion, I found the actual rotation frequency and amplitude from video sequences of the wings. I calculated the rotation frequency in each sequence as the inverse of the number of frames in a complete rotation divided by 1000 (Table 5.1). I found the rotation amplitude for all sequences of a given wing from the motions of the leading edge in the calibration sequence (because at 26 Hz the leading edge bends slightly and moves through a larger amplitude). To determine whether rotation amplitude varies between 0.5 and 26 Hz, I measured the amplitude of an inflexible,

hollow brass rod (attached in the same way as a wing and of equivalent weight) rotating at both frequencies (Table 5.1).

To quantify wing bending in the spanwise direction, I calculated the difference (in degrees) between the leading edge and wing tip (Fig. 5.2). Although the wing bends along its entire span, the majority of bending occurs between the leading edge marker (at ~50% span) and the tip. To quantify chordwise bending, I calculated the difference in position between the leading and trailing edge. Because of the inherent camber of *Manduca* wings, the position of these points often differs slightly, even in calibration sequences with no dynamic bending (Fig. 5.3). I therefore subtracted the leading edge/tip and leading edge/trailing edge differences in calibration sequences from the differences in the same wing when rotating at 26 Hz. I used the position of the leading edge in time to align the start and stop points of the sequences and used a Matlab program to spline the data to an equal number of points for comparison (Appendix 5).

Finally, I corrected the calculated differences in position for the direction of motion of the wing. I used the derivative of the position of the leading edge to determine if the wing was rotating to the left or the right, and multiplied the values calculated when the wing was moving to the right by -1. The resulting differences in position are negative if the tip or trailing edge follows the leading edge and positive if the tip or trailing edge precedes (moves in front of) the leading edge.

Finite element modeling

I created a finite element model (FEM) based on the planform image of a male *Manduca* wing (see Chapter 4). The model is composed of 345 thin shell elements of uniform thickness (110 μm), with a mixture of 3- and 4-node (triangular and square) elements. I adjusted the material stiffness (Young's modulus) of the elements to provide an exponential decline in flexural stiffness in both the spanwise and chordwise directions (approximating patterns of stiffness in real wings, see Chapter 4); vein elements are stiffer than membrane elements to mimic the increased flexural stiffness of tubular veins (and to provide the measured spanwise-chordwise anisotropy, see Chapter 3). I used a Poisson's ratio of 0.495 (consistent with measured values of biological materials; Wainwright et al., 1982) and set the density of wing elements at 500 kg/m^3 , which gives the correct total wing weight of 0.035 g (this density estimate may be lower and the average thickness higher than in real *Manduca* wings, but because the mass distribution is uniform, these values should have little effect on the results).

Because the modeling program cannot calculate unsteady fluid forces, the predicted motions of the model wing approximate the motions of a wing rotating in a vacuum (with no fluid present), and thus depend on inertial-elastic forces alone. Because fluid generally damps high-frequency motions, a damping factor is often applied to finite element models to simulate the effects of a fluid medium. I used a mass damping factor (mass matrix multiplier of 300) and compared the motions of the model wing with and without this damping.

I rotated the model wing around its base (with no displacement) at a frequency of 26 Hz, as in the experiments on real wings. I started the wing from rest and gradually increased the amplitude of motion to a sinusoidal curve with the following equation:

$$\theta = (1 - e^{-t/\tau}) \sin(\omega t) \quad (5.1)$$

where θ is the rotation at the base nodes (in radians, standardized to an amplitude of +/- 1), t is time in seconds, τ is the time constant and ω is the angular frequency ($2\pi f$, where f is the flapping frequency). I multiplied the standardized amplitude by 0.9245 radians to rotate the base through a total amplitude of 108.5° and adjusted the time constant ($\tau = 1/50$) to minimize the effects of initial conditions at the base.

I ran the model for 4800 steps, simulating a total flapping time of 0.24 seconds. Within this time, the wing rotated through 6.25 cycles, with the last 3.5 cycles at full amplitude. I measured displacement of nodes at the wing tip, leading edge, and trailing edge (in the same locations as on real wings) through the last three cycles of rotation and calculated spanwise bending (leading edge/tip difference) and chordwise bending (leading/trailing edge difference) as above.

Results

Measured values of rotation frequency and amplitude in the three *Manduca* wings are similar, with an average amplitude of 108° , calibration frequency of 0.56 Hz and experimental frequency of 26.2 Hz (Table 5.1). The control performed on a hollow brass rod reveals that rotation amplitude does not change dramatically with frequency (Table

5.1), so amplitudes measured on calibration sequences of each wing can be used to approximate rotation amplitudes at 26 Hz.

The trajectories of the wing tip, leading edge, and trailing edge of wings rotated in normal air at the end of the experiment are indistinguishable from those of wings rotated in normal air at the beginning (data not shown), indicating that the experimental procedure does not damage the wings and that wings do not stiffen appreciably during the procedure. Data from the initial rotation in normal air (as well as the rotation in helium) are presented in Figures 5.4 and 5.5.

The positions of the wing tip and trailing edge reveal that the motions of the wings in normal air and in helium are remarkably similar (top panels, Fig. 5.4, 5.5). Overall patterns of spanwise bending (leading edge/tip differences) and chordwise bending (leading/trailing edge differences) are also similar (bottom panels, Fig. 5.4, 5.5). The wings display some dorsal/ventral asymmetry, but bending patterns are comparable in both directions.

In both normal air and in helium, the tip and trailing edge follow the leading edge through much of the rotation (as indicated by the negative values in bottom panels of Fig. 5.4, 5.5). However, as the wing slows to change direction, the tip and trailing edge tend to move in front of the leading edge (as indicated by positive values in Fig. 5.4, 5.5; see also position of arrow in Fig. 5.2).

Simulations with the FEM wing reveal a similar pattern. The positions of the wing tip and trailing edge are similar to those measured in real wings, and the tip and trailing edge move in front of the leading edge as the wing slows to reverse direction

(Fig. 5.6). For movies of wing bending in real and model wings, see

<http://faculty.washington.edu/danieli/movies>.

Discussion

Manduca wings bend appreciably when rotated at normal flight frequencies, with the wing tip and trailing edge following the leading edge by up to 20 degrees. Overall wing motions and patterns of bending are similar in both normal air and in helium. In both cases, the tip and trailing edge follow the leading edge for much of the rotation, but as the wing slows, the tip and trailing edge swing in front of the leading edge.

The similarity in *Manduca* wing trajectory and bending patterns, despite an 85% decrease in fluid density, suggests that the contribution of aeroelasticity to wing deformations may be relatively minor compared to the contribution of wing inertia. These experimental results agree with several previous theoretical analyses of the effects of wing inertia on bending. Ennos (1989) estimated that spanwise local bending moments due to the inertia of flapping wings may be at least twice as large as those due to aerodynamic forces, and showed that wing inertia alone could cause the tip-to-base torsional wave seen in many insect wings during supination (Ennos, 1988). Daniel and Combes (in prep.) examined chordwise local bending moments in oscillating, flexible strips of wings and found that when these motions occur in air, bending moments generated by elastic wave propagation (inertial-elastic effects) are significantly larger than the moments exerted on the strip by the fluid (fluid-dynamic effects).

Although overall patterns of bending in the wings tested appear to be dominated by inertial-elastic forces, some aspects of wing motion differ in normal air *versus* helium. The most obvious difference is the presence of higher-frequency components of motion in the wings rotating in helium. Both the tip and trailing edge oscillate around the position of the leading edge, particularly after swinging in front of the leading edge as the wing changes direction (Fig. 4.4, 4.5). This type of motion is also present (to a lesser degree) in wings rotating in normal air. However, because these oscillations are smaller, the tip and trailing edge of wings rotating in normal air tend to fall farther behind the leading edge during the middle of a rotation than wings in helium (i.e. shaded areas of Fig. 4.4, 4.5).

Simulations of wing bending in the model wing suggest that fluid damping could explain why these higher-frequency motions are reduced in normal air. The undamped model displays high-frequency motions similar to those seen in real wings rotating in helium (Fig. 5.6). However, mass damping removes these oscillations and causes the wing tip and trailing edge to fall farther behind the leading edge during the middle of each rotation (Fig. 5.6), as in real wings rotated in normal air (Fig. 5.4, 5.5). These results suggest that a damped finite element model could be successful in predicting the overall pattern and magnitude of wing deformations. This model would require knowing only the wing's stiffness distribution (see Chapter 4), its mass distribution (which was absent in the current model), and the boundary conditions (torques or angular excursions) at the base.

The current analysis focuses on *Manduca sexta*, a relatively large insect with heavy wings. The large size and weight of *Manduca* wings might suggest that inertial-elastic effects would be more important in determining wing bending in this species than in other species with smaller, lighter wings. A simple analysis of average bending moments can be used to assess the relative magnitudes of inertial-elastic and aerodynamic moments on flapping wings (Daniel and Combes, in prep):

$$R = (m_w / m_b)4\Theta\omega^2L / 3g \quad (5.2)$$

where R is the ratio of inertial-elastic to aerodynamic bending moments, m_w is mass of the wing, m_b is mass of the body, Θ is stroke amplitude, ω is angular frequency (2π * flapping frequency), L is wing span and g is earth's gravitational acceleration. The ratio of wing to body mass is relatively conserved in many insects, falling between approximately 0.5% and 3% (Ellington, 1984b), but wing span (L) varies widely. However, because the frequency term in Eq. 5.2 is squared, flight frequency has a large effect on the moment ratio. Thus, many smaller insects (with higher flight frequencies; Dudley, 2000) may actually have higher ratios of inertial-elastic to aerodynamic bending moments. Estimates suggest that this ratio is large in insects over a broad size range ($R=5$ in *Manduca* and $R=4$ in *Drosophila melanogaster*), indicating that inertial-elastic effects may be critical in determining wing bending in many species.

Because aeroelastic effects appear to play a relatively minor role in determining dynamic wing shape, an integrative model of insect flight that incorporates passive wing flexibility may be easier to develop than previously thought. Numerical methods that provide detailed calculations of fluid-solid interactions in each time step will

undoubtedly continue to contribute to our understanding of three-dimensional fluid flow and force production in insect flight. However, recent work suggests that far simpler analytical methods are able to predict the temporal patterns of force production in flapping wings remarkably well (Sane and Dickinson, 2002). Inserting the dynamic shape of wing sections (as determined by a simple damped FEM analysis) into quasi-steady models of flight that account for some unsteady effects (such as wing rotation and added mass) may yield a tractable modeling tool that could be used to explore the effects of passive wing flexibility on aerodynamic force production.

Concluding remarks

The results of this study suggest that aeroelastic interactions between insect wings and the fluid-dynamic forces they generate may play a relatively minor role in determining wing deformations, when compared to the inertial-elastic forces generated by flapping wings themselves. This finding greatly simplifies the process of predicting dynamic wing shape, and brings us one step closer to developing a tractable model of insect flight that incorporates passive wing flexibility. Given that overall flexural stiffness scales with wing size (Chapter 3) and declines sharply towards the tip and trailing edge of wings (Chapter 4), measurements of mass distribution in a wing should allow one to make a reasonable prediction of the patterns and magnitude of wing deformations during flight, using a simple damped finite element model of a wing. This information could then be incorporated into a variety of models of insect flight to

understand how passive wing flexibility affects aspects of flight performance ranging from force production to maneuverability and control.

Acknowledgements

I would like to thank M. Dillon for help constructing the vacuum chamber and calibrating the high-speed video cameras, and J. Longnion for his work in salvaging and altering chart recorder motors. E. Goldman provided valuable suggestions regarding data analysis, and M. Tu provided Matlab code for digitizing wing coordinates. K. Flick was instrumental in troubleshooting the high-speed video cameras and J. Dierberger at MSC Software provided crucial troubleshooting of the FEM model. T. Daniel provided stimulating discussions and inspiration throughout the project. This work was supported by NSF grant 66-1822 to T. Daniel, the John D. and Catherine T. MacArthur Foundation, an NSF graduate fellowship to S. Combes, and an ARCS fellowship to S. Combes.

Notes to Chapter 5

Batchelor, G. K. (1967). *An introduction to fluid dynamics*. Cambridge: Cambridge University Press.

Bisplinghoff, R. L. and Ashley, H. (1975). *Principles of aeroelasticity*. New York: Dover Publications, Inc.

Combes, S. A. and Daniel, T. L. (2001). Shape, flapping and flexion: wing and fin design for forward flight. *J. Exp. Biol.* **204**, 2073-2085.

CRC Handbook of chemistry and physics, 81st Ed. (2001). Cleveland, Ohio: CRC Press.

Daniel, T. L. (1987). Forward flapping flight from flexible fins. *Can J. Zool.* **66**, 630-638.

Daniel, T. L. and Combes, S. A. (in prep). Flexing wings and fins: bending by inertial or fluid-dynamic forces? *Amer. Zool.*

Dudley, R. (2000). *The biomechanics of insect flight: form, function, evolution*. Princeton, NJ: Princeton University Press.

Ellington, C. P. (1984b). The aerodynamics of hovering insect flight. Part II: Morphological parameters. *Phil. Trans. R. Soc. Lond. B* **305**, 17-40.

Ellington, C. P. (1984c). The aerodynamics of hovering insect flight. Part III: Kinematics. *Phil. Trans. R. Soc. Lond. B* **305**, 41-78.

Ellington, C. P. (1984f). The aerodynamics of hovering insect flight. Part VI: Lift and power requirements. *Phil. Trans. R. Soc. Lond. B* **305**, 145-181.

Ellington, C. P., Van den Berg, C., Willmott, A. P. and Thomas, A. L. R. (1996). Leading-edge vortices in insect flight. *Nature* **384**, 626-630.

Ennos, A. R. (1988). The inertial cause of wing rotation in Diptera. *J. Exp. Biol.* **140**, 161-169.

Ennos, A. R. (1989). Inertial and aerodynamic torques on the wings of Diptera in flight. *J. Exp. Biol.* **142**, 87-95.

- Fish, F. E. (1999). Performance constraints on the maneuverability of flexible and rigid biological systems. In *Eleventh International Symposium on Unmanned Untethered Submersible Technology*, pp. 394-406. Durham, NH: Autonomous Undersea Systems Institute.
- Lehmann, F.-O. and Dickinson, M. H. (1997). The changes in power requirements and muscle efficiency during elevated force production in the fruit fly *Drosophila melanogaster*. *J. Exp. Biol.* **200**, 1133-1143.
- Liu, H., Ellington, C. P., Kawachi, K., Van den Berg, C., and Willmott, A. P. (1998). A computational fluid dynamic study of hawkmoth hovering. *J. Exp. Biol.* **201**, 461-477.
- Liu, H. and Kawachi, K. (1998). A numerical study of insect flight. *J. Computational Physics* **146**, 124-156.
- Sane, S. P. and Dickinson, M. H. (2002). The aerodynamic effects of wing rotation and a revised quasi-steady model of flapping flight. *J. Exp. Biol.* **205**, 1087-1096.
- Sneyd, A. D., Bundock, M. S. and Reid, D. (1982). Possible effects of wing flexibility on the aerodynamics of *Pteranodon*. *Am. Nat.* **120(4)**, 455-477.
- Wakeling, J. M. and Ellington, C. P. (1997c). Dragonfly flight. III. Lift and power requirements. *J. Exp. Biol.* **200**, 583-600.
- Walker, J. A. (2000). Does a rigid body limit maneuverability? *J. Exp. Biol.* **203**, 3391-3396.
- Wilkin, P. J. and Williams, M. H. (1993). Comparison of the aerodynamic forces on a flying sphingid moth with those predicted by quasi-steady theory. *Physiol. Zool.* **66(6)**, 1015-1044.
- Wu, T. Y. (1971). Hydromechanics of swimming propulsion. Part 1. Swimming of a two dimensional flexible plate at variable forward speeds in an inviscid fluid. *J. Fluid Mech.* **46**, 337-355.
- Zanker, J. M. and Gotz, K. G. (1990). The wing beat of *Drosophila melanogaster*. II. Dynamics. *Phil. Trans. R. Soc. Lond. B* **327**, 19-44.

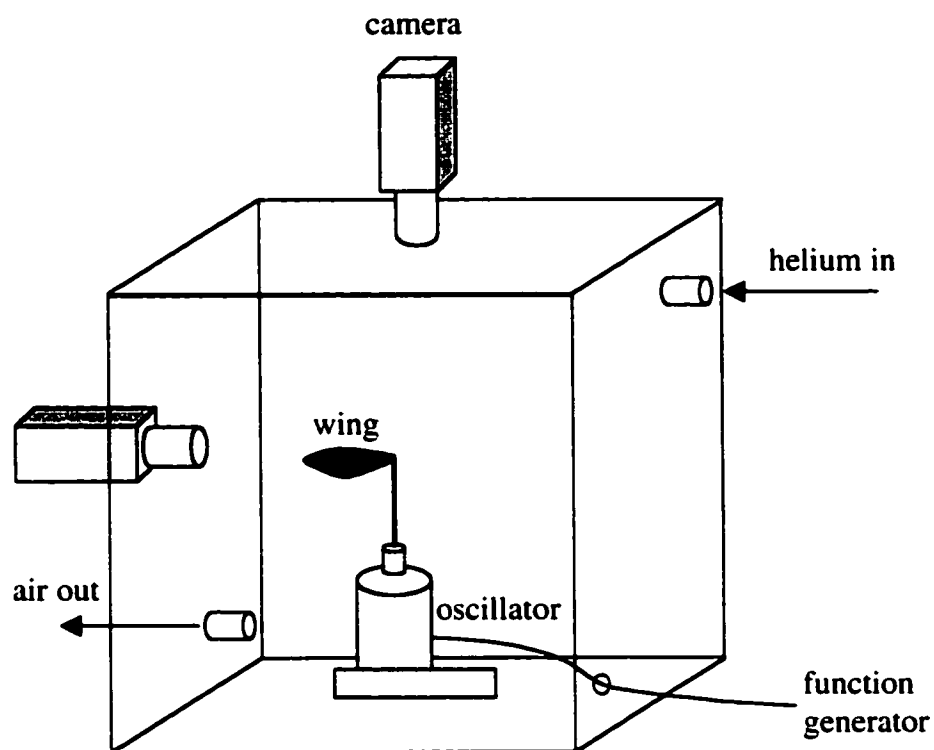


Fig. 5.1. Apparatus used to test *Manduca* wing bending in low air density. A wing is attached to an oscillator that rotates the wing around its base. The wing is rotated at 26 Hz through a total amplitude of 110 degrees and filmed at 1000 frames per second from orthogonal views. Then approximately half the air is removed from the box and replaced with helium. This process is repeated until the box is filled with helium (~15% normal air density) and the wing is again filmed while rotating.

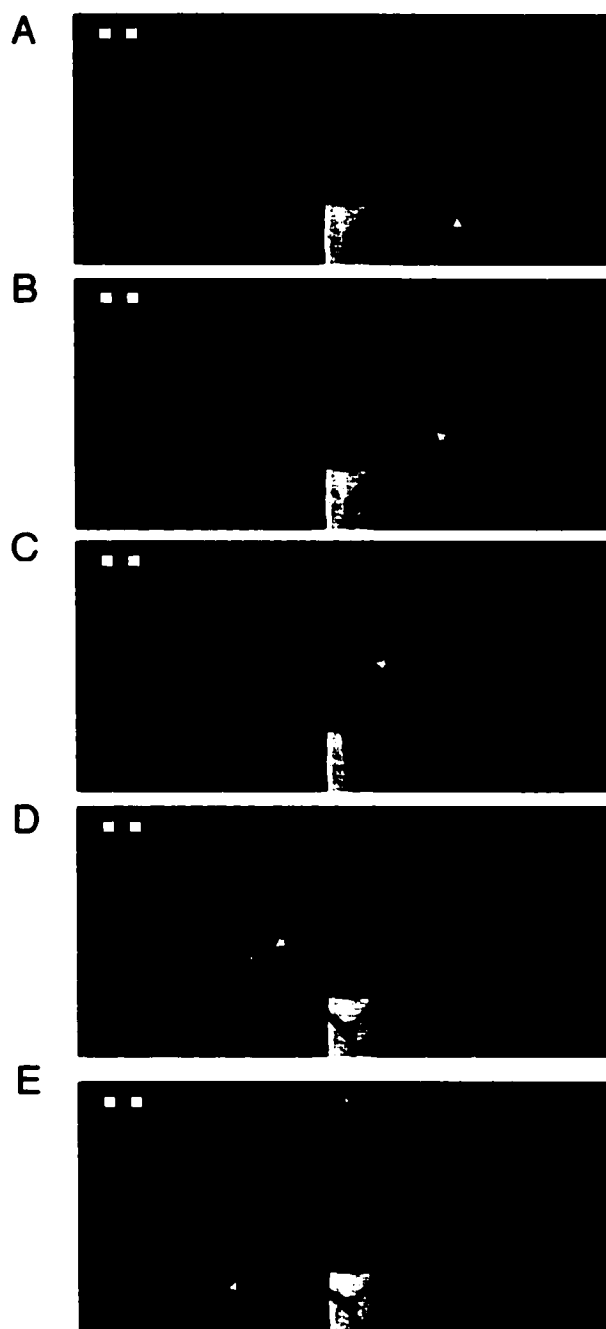


Fig 5.2. Frames from high-speed video of a *Manduca* wing rotating at 26 Hz in low air density. The wing is viewed from above and the positions of the leading edge (star), trailing edge (arrow) and tip are digitized in each frame. In this sequence, the wing is rotating to the left, with the dorsal side of the wing leading the motion. Note that the leading edge precedes the wing tip and trailing edge for most of the rotation, but as the wing slows, the wing tip (D and E) and trailing edge (E) move in front of the leading edge.

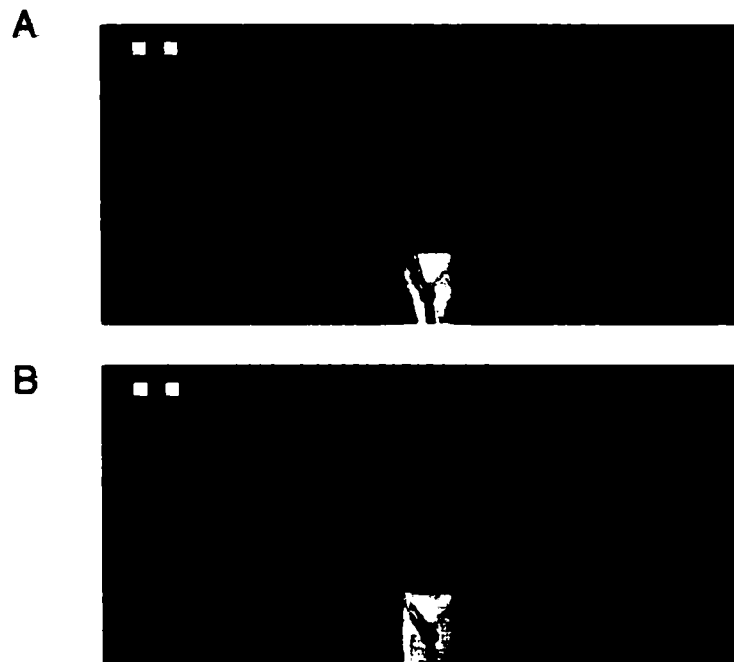


Fig 5.3. Frames from high-speed video of a *Manduca* wing rotating in normal air at 26 Hz and 0.5 Hz. In this sequence, the wing (viewed from above) is rotating to the left with its dorsal surface leading the motion. To quantify wing bending, the position of the leading edge, trailing edge, and wing tip are found (in degrees) for the same wing rotating at 26 Hz (A) and 0.5 Hz (B). The difference between the position of the leading edge (solid line) and trailing edge (dashed line) is used to quantify bending in the chordwise direction. Differences due to the inherent camber of the wing are removed by subtracting the leading/trailing edge difference in a slowly rotating wing (in which no dynamic bending occurs, B) from the leading/trailing edge difference in a wing rotating at *Manduca* flight frequency (A).

Fig. 5.4. Spanwise bending of *Manduca* wings rotated in normal versus low air density. Wings from three different individuals (A,B,C) are shown. Wings were rotated around one axis at ~26 Hz through a total amplitude of ~110°. For each individual, the top panel shows the position of the wing tip (in degrees) and the bottom panel shows the difference in position between the leading edge and the wing tip (in degrees). This difference is adjusted for the direction of motion; values less than zero indicate that the wing tip follows the leading edge, while values greater than zero indicate that the tip precedes the leading edge. Segments in which the dorsal surface of the wing is leading the motion are shaded.

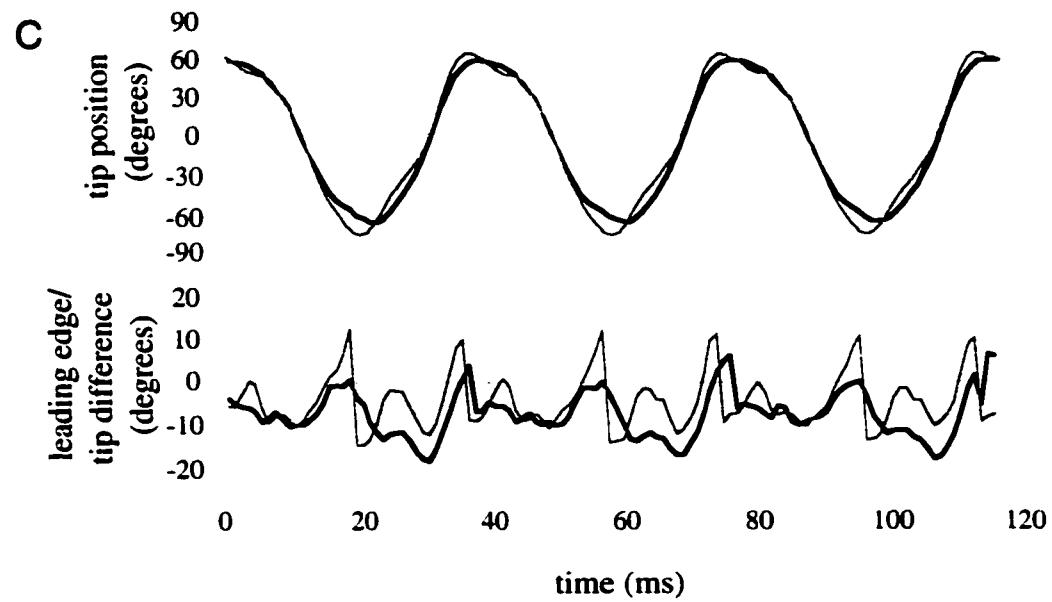
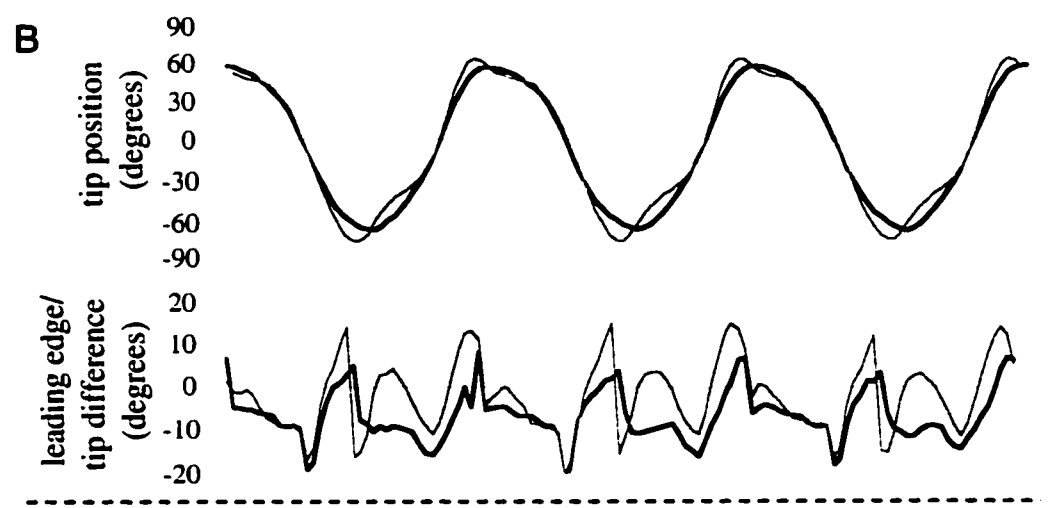
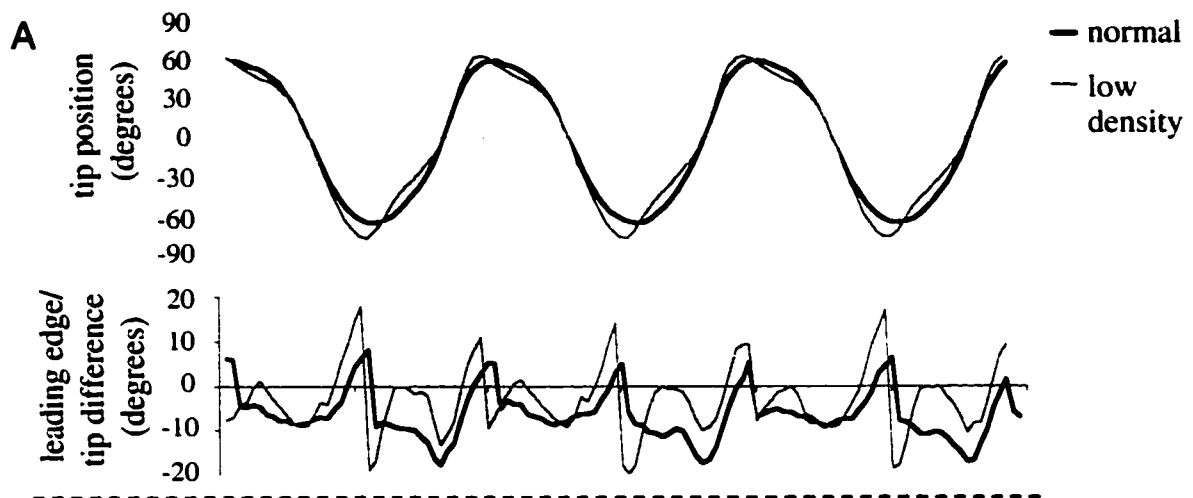
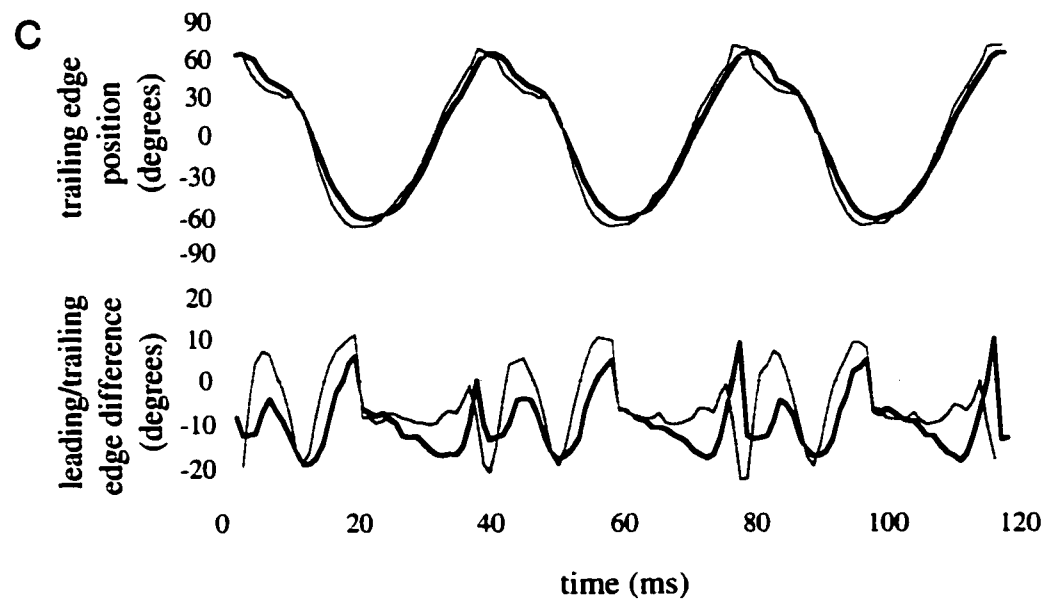
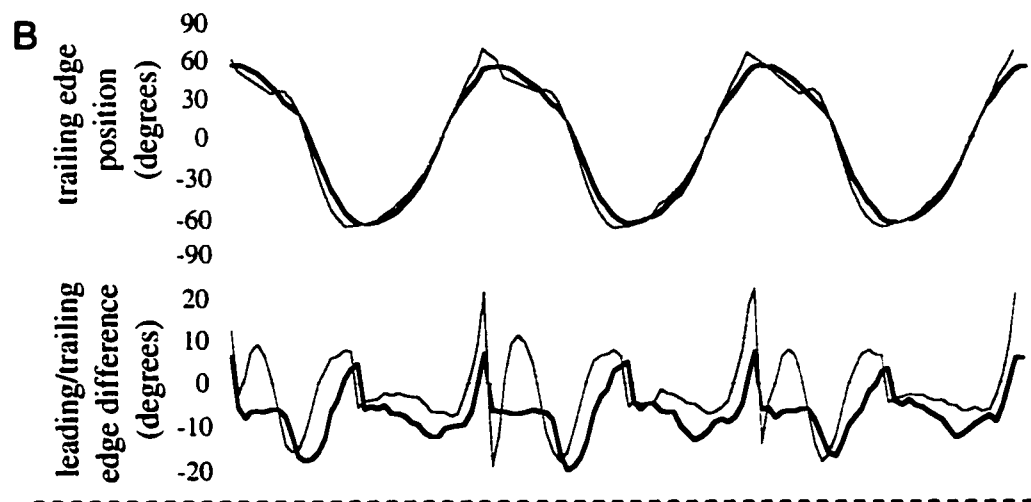
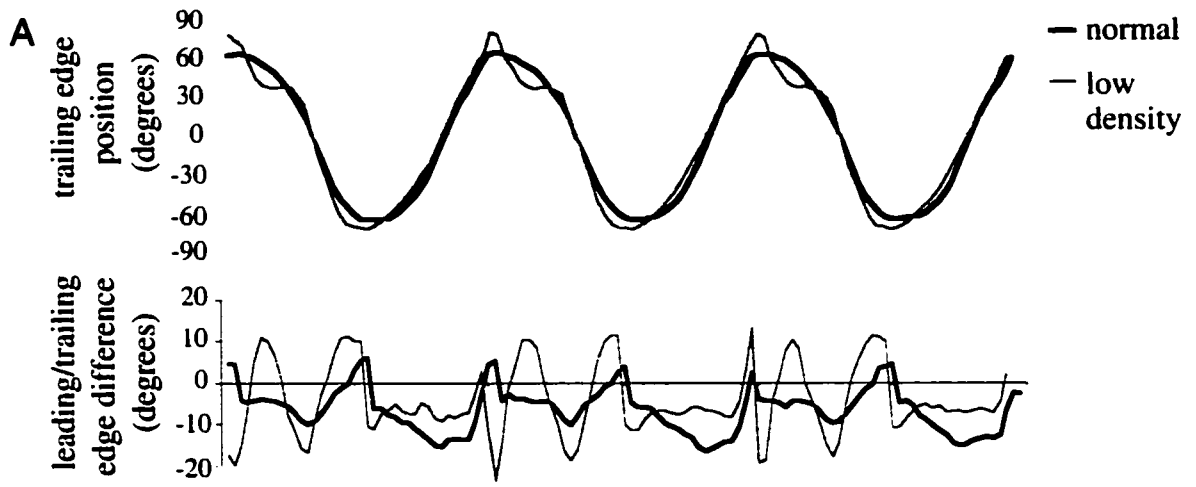


Fig. 5.5. Chordwise bending of *Manduca* wings rotated in normal versus low air density. Wings from three different individuals (A,B,C) are shown. Wings were rotated around one axis at ~26 Hz through a total amplitude of ~110°. For each individual, the top panel shows the position of the trailing edge (in degrees) and the bottom panel shows the difference in position between the leading edge and the trailing edge (in degrees), measured at approximately 50% wing span. This difference is adjusted for the direction of motion; values less than zero indicate that the trailing edge follows the leading edge, while values greater than zero indicate that the trailing edge precedes the leading edge. Segments in which the dorsal surface of the wing is leading the motion are shaded.



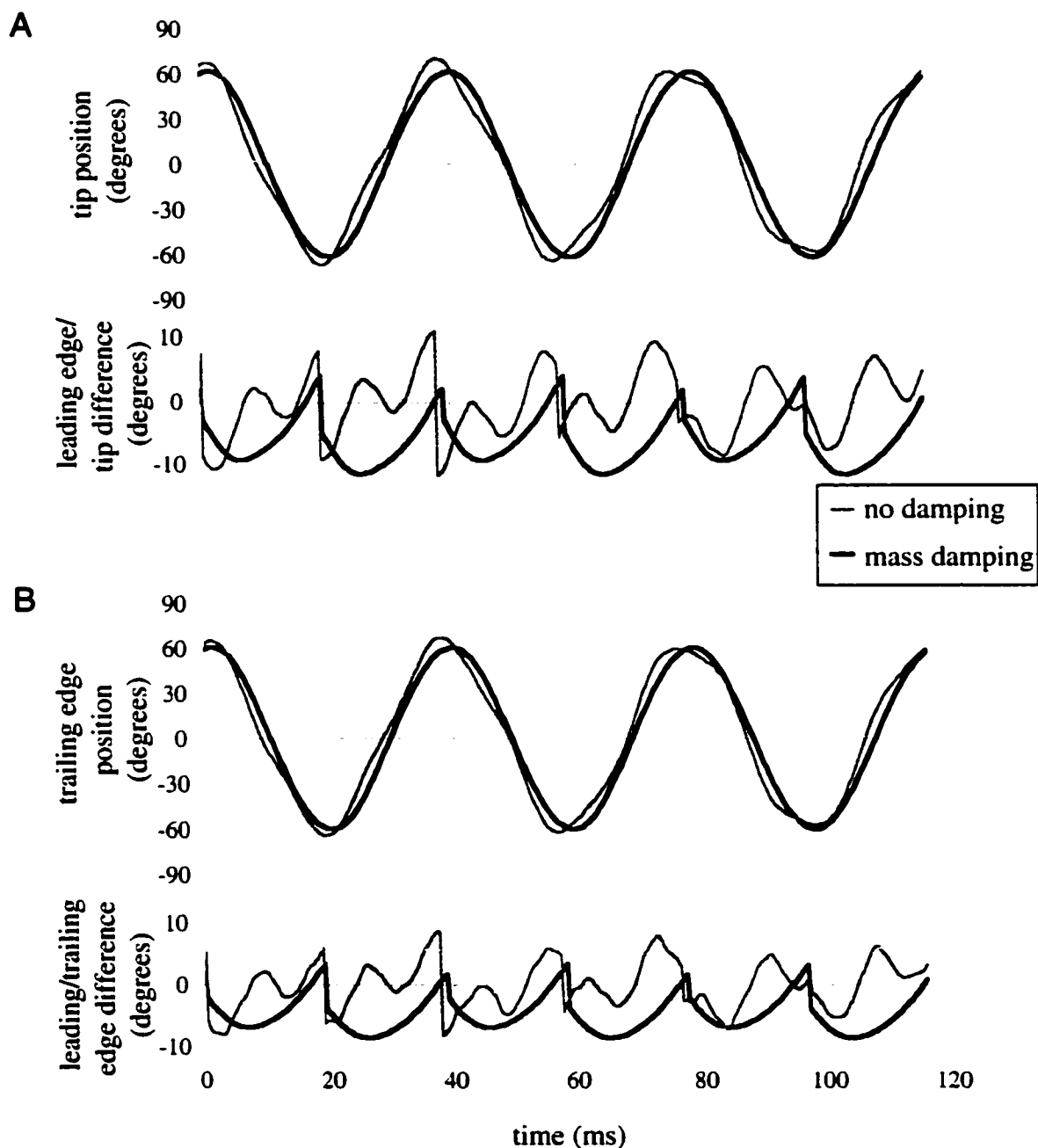


Fig. 5.6. Wing bending in undamped and damped finite element models of a rotating *Manduca* wing. (A) Spanwise bending in the model wing; top panel shows tip position and bottom shows difference in position between the leading edge and tip. (B) Chordwise bending in the model wing; top panel shows trailing edge position and bottom shows difference in position between the leading and trailing edge. Models were rotated around one axis at 26 Hz through an total amplitude of 108.5° . Results are shown for a model with no damping and a model with mass damping (mass matrix multiplier=300).

Table 5.1. Measured rotation frequency and amplitude in *Manduca* wings and brass rod control. Wing rotation amplitude in experimental sequences was estimated from the measured amplitude in calibration sequences of each wing.

	calibration sequence (0.5 Hz)	experimental sequence (normal air)	experimental sequence (helium)	experimental sequence (normal air, post helium)
brass rod	0.57 Hz 123.7°	26.3 Hz 125.8°		
individual A	0.56 Hz 109.9	25.8 Hz	26.9 Hz	26.6 Hz
individual B	0.56 Hz 107.1	25.5 Hz	25.5 Hz	25.5 Hz
individual C	0.57 Hz 107.1	26.6 hz	26.6 Hz	26.6 Hz

Bibliography

- Alexander, R. McN., Jayes, A. S., Maloiy, G. M. O., and Wathuta, E. M. (1979). Allometry of the limb bones of mammals from shrews (*Sorex*) to elephant (*Loxodonta*). *J. Zool., Lond.* **189**, 305-314.
- Arbas, E. A., Levine, R. B. and Strausfeld, N. J. (1997). Invertebrate nervous systems. In *Handbook of Physiology, Section 13, Comparative Physiology, vol II.* (ed. W. H. Dantzler). New York: Oxford University Press.
- Batchelor, G. K. (1967). *An introduction to fluid dynamics.* Cambridge: Cambridge University Press.
- Benton, M. J. (editor) (1993). *The Fossil Record 2.* London: Chapman & Hall, 845 pp. <http://palaeo.gly.bris.ac.uk/frwhole/FR2.html>
- Bestor, C. J. (1993). Pectoral fin locomotion in the spotted ratfish, *Hydrolagus colliei*. *Friday Harbor Laboratories Fisheries 565 course papers* , 1-17.
- Biewener, A. A. and Dial, K. P. (1995). In vivo strain in the humerus of pigeons (*Columba livia*). *J. Morph.* **225(1)**, 61-75.
- Birch, J. M. and Dickinson, M. H. (2001). Spanwise flow and the attachment of the leading-edge vortex on insect wings. *Nature* **412**, 729-733.
- Bisplinghoff, R. L. and Ashley, H. (1975). *Principles of aeroelasticity.* New York: Dover Publications, Inc.
- Blake, R. W. (1983a). *Fish Locomotion.* London: Cambridge University Press.
- Blake, R. W. (1983b). Hovering performance of a negatively buoyant fish. *Can. J. Zool.* **61**, 2629-2630.
- Blake, R. W. (1983c). Median and paired fin propulsion. In *Fish Biomechanics.* (ed. P. W. Webb and D. Weihs), pp. 214-217. New York: Frederick A. Praeger Inc.
- Borror, D. J., Triplehorn, C. A., and Johnson, N. F. (1989). *An Introduction to the Study of Insects*, 6th ed. Fort Worth, TX: Harcourt Brace College Publishers.
- Clark, B. D. and Bemis, W. (1979). Kinematics of swimming of penguins at the Detroit Zoo. *J. Zool.* **188**, 411-428.
- Combes, S.A. and Daniel, T.L. (2001). Shape, flapping and flexion: Wing and fin design for forward flight. *J. Exp. Biol.* **204(12)**, 2073- 2085.

Corning, W. R. and Biewener, A. A. (1998). In vivo strains in pigeon flight feather shafts: Implications for structural design. *J. Exp. Biol.* **201** (22), 3057-3065.

CRC Handbook of chemistry and physics, 81st Ed. (2001). Cleveland, Ohio: CRC Press.

Daniel, T. L. (1987). Forward flapping flight from flexible fins. *Can J. Zool.* **66**, 630-638.

Daniel, T. L. and Combes, S. A. (in prep). Flexing wings and fins: bending by inertial or fluid-dynamic forces? *Amer. Zool.*

Dickinson, M. H. (1996). Unsteady mechanisms of force generation in aquatic and aerial locomotion. *Amer. Zool.* **36**, 537-554.

Dickinson, M. H., Lehmann, F. -O., and Sane, S. P. (1999). Wing rotation and the aerodynamic basis of insect flight. *Science* **184**, 1954-1960.

Dudley, R. (2000). *The biomechanics of insect flight: form, function, evolution*. Princeton, NJ: Princeton University Press.

Eaton, J. L. (1988). *Lepidopteran Anatomy*. New York: John Wiley & Sons.

Ellington, C. P. (1984a). The aerodynamics of hovering insect flight. Part I: The quasi-steady analysis. *Phil. Trans. R. Soc. Lond. B* **305**, 1-15.

Ellington, C. P. (1984b). The aerodynamics of hovering insect flight. Part II: Morphological parameters. *Phil. Trans. R. Soc. Lond. B* **305**, 16-40.

Ellington, C. P. (1984c). The aerodynamics of hovering insect flight. Part III: Kinematics. *Phil. Trans. R. Soc. Lond. B* **305**, 41-78.

Ellington, C. P. (1984d). The aerodynamics of hovering insect flight. Part IV: Aerodynamic mechanisms. *Phil. Trans. R. Soc. Lond. B* **305**, 79-113.

Ellington, C. P. (1984e). The aerodynamics of hovering insect flight. Part V: A vortex theory. *Phil. Trans. R. Soc. Lond. B* **305**, 115-144.

Ellington, C. P. (1984f). The aerodynamics of hovering insect flight. Part VI: Lift and power requirements. *Phil. Trans. R. Soc. Lond. B* **305**, 145-181.

Ellington, C. P. (1995). Unsteady aerodynamics of insect flight. In *Biological Fluid Dynamics* (ed. C. P. Ellington and T. J. Pedley), pp. 109-129. Cambridge, U.K.: The Company of Biologists Limited.

Ellington, C. P., Van Den Berg, C., Willmott, A. P. and Thomas, A. L. R. (1996). Leading-edge vortices in insect flight. *Nature* **384**, 626-630.

Ennos, A. R. (1988). The importance of torsion in the design of insect wings. *J. Exp. Biol.* **140**, 137-160.

Ennos, A. R. (1989). Inertial and aerodynamic torques on the wings of Diptera in flight. *J. Exp. Biol.* **142**, 87-95.

Ennos, A. R. (1995). Mechanical behavior in torsion of insect wings, blades of grass and other cambered structures. *Proc. R. Soc. Lond. B* **259**, 15-18.

Ennos, A. R. (1997). Flexible structures in biology. *Comments Theor. Biol.* **4(2-3)**, 133-149.

Ennos, A. R. and Wootton, R. J. (1989). Functional wing morphology and aerodynamics of *Panorpa germanica* (Insecta: Mecoptera). *J. Exp. Biol.* **143**, 267-284.

Felsenstein, J. (1985). Phylogenies and the comparative method. *Am. Nat.* **125**, 1-15.

Fish, F. E. (1999). Performance constraints on the maneuverability of flexible and rigid biological systems. In *Eleventh International Symposium on Unmanned Untethered Submersible Technology*, pp. 394-406. Durham, NH: Autonomous Undersea Systems Institute.

Full, R. J. and Koditschek, D. E. (1999). Templates and anchors: neuromechanical hypotheses of legged locomotion on land. *J. Exp. Biol.* **202**, 3325-3352.

Fung, Y. C. (1990). *Biomechanics: Motion, Flow, Stress, and Growth*. New York: Springer-Verlag.

Garland, T., Jr., Dickerman, A. W., Janis, C. M., and Jones, J.A. (1993). Phylogenetic analysis of covariance by computer simulation. *Syst. Biol.* **42**, 265-292.

Garland, T., Jr., Midford, P. E., and Ives, A. R. (1999). An introduction to phylogenetically based statistical methods, with a new method for confidence intervals on ancestral states. *Amer. Zool.* **39**, 374-388.

- Garland, T., Jr., and Ives, A. R. (2000). Using the past to predict the present: Confidence intervals for regression equations in phylogenetic comparative methods. *Am. Nat.* **155**, 346-364.
- Garland, T., Jr., and Janis, C. M. (1993). Does metatarsal/femur ratio predict maximal running speed in cursorial mammals? *J. Zool., Lond.* **229**, 133-151.
- Gorb, S. N. (1999). Serial elastic elements in the damselfly wing: mobile vein joints contain resilin. *Naturwiss.* **86**, 552-555.
- Gordon, J.E. (1978). *Structures: or Why Things Don't Fall Down*. New York: Penguin Books.
- Haas, F., Gorb, S., and Blickhan, R. (2000). The function of resilin in beetle wings. *Proc. R. Soc. Lond. B* **267**, 1375-1381.
- Haas, F., Gorb, S., and Wootton, R. J. (2000). Elastic joints in dermapteran hind wings: materials and wing folding. *Arthropod Structure & Development* **29**, 137-146.
- Herbert, R. C., Young, P. G., Smith, C. W., Wootton, R. J., and Evans, K. E. (2000). The hind wing of the desert locust (*Schistocerca gregaria* Forskål). III. A finite element analysis of a deployable structure. *J. Exp. Biol.* **203**, 2945-2955.
- Kammer, A. E. (1985). Flying. In *Comprehensive Insect Physiology, Biochemistry and Pharmacology. Vol 5, Nervous system: structure and motor function*. (ed. G. A. Kerkut and L. I. Gilbert). Oxford: Pergamon Press.
- Kent, G. C. (1992). *Comparative anatomy of the vertebrates*. St. Louis, Missouri: Mosby-Year Book, Inc.
- Kesel, A. B., Philippi, U., and Nachtigall, W. (1998). Biomechanical aspects of the insect wing: an analysis using the finite element method. *Computers in Biol. and Med.* **28**, 423-437.
- Kristensen, N. P. (1991). Phylogeny of extant hexapods. In *The Insects of Australia: A textbook for students and research workers*, 2nd ed., Vol. 1, pp. 125-140. Ithaca, NY: Cornell University Press.
- Kubow, T. M. and Full, R. J. (1999). The role of the mechanical system in control: a hypothesis of self-stabilization in hexapedal runners. *Phil. Trans. R. Soc. Lond. B* **354**, 849-861.

- Kukalova-Peck, J. (1991). Fossil history and the evolution of hexapod structures. In *The Insects of Australia: A textbook for students and research workers*, 2nd ed., Vol. 1, pp. 141-179. Ithaca, NY: Cornell University Press.
- Lehmann, F.-O. and Dickinson, M. H. (1997). The changes in power requirements and muscle efficiency during elevated force production in the fruit fly *Drosophila melanogaster*. *J. Exp. Biol.* **200**, 1133-1143.
- Lighthill, M. J. (1975). *Mathematical Biofluidynamics*. Philadelphia: Society for Industrial Applied Mathematics.
- Liu, H., Ellington, C. P., Kawachi, K., Van Den Berg, C. and Willmott A. P. (1998). A computational fluid dynamic study of hawkmoth hovering. *J. Exp. Biol.* **201**, 461-477.
- Liu, H. and Kawachi, K. (1998). A numerical study of insect flight. *J. Computational Physics* **146**, 124-156.
- Maddison, D. R. (1995a). Hymenoptera. In *The Tree of Life Web Project*, (ed. D. R. Maddison and K.-S. Schultz). <http://tolweb.org/tree/phylogeny.html>
- Maddison, D. R. (1995b). Lepidoptera. In *The Tree of Life Web Project*, (ed. D. R. Maddison and K.-S. Schultz). <http://tolweb.org/tree/phylogeny.html>
- McMahon, T. A. (1973). Size and shape in biology. *Science* **179**: 1201-1204.
- Newman, D. J. S. and Wootton, R. J. (1986). An approach to the mechanics of pleating in dragonfly wings. *J. Exp. Biol.* **125**, 361-372.
- Pagel, M. D. (1992). A method for the analysis of comparative data. *J. Theor. Biol.* **164**, 194-205.
- Papadimitriou, H. M., Swartz, S. M. and Kunz, T. H. (1996). Ontogenetic and anatomic variation in mineralization of the wing skeleton of the Mexican free-tailed bat, *Tadarida brasiliensis*. *J. Zool., Lond.* **240(3)**, 411-426.
- Pennycuik, C. J. (1972). *Animal Flight*. London: Edward Arnold (Publishers) Ltd.
- Peskin, C. S. (1995). A general method for the computer simulations of biological systems interacting with fluids. In *Biological Fluid Dynamics* (ed. C. P. Ellington and T. J. Pedley), pp. 265-275. Cambridge, U.K.: The Company of Biologists Limited.
- Rayner, J. M. V. (1979). A new approach to animal flight mechanics. *J. Exp. Biol.* **80**, 17-54.

- Rezende, E. L., Swanson, D. L., Novoa, F. F., and Bozinovic, F. (2002). Passerines versus nonpasserines: so far, no statistical differences in the scaling of avian energetics. *J. Exp. Biol.* **205**, 101-107.
- Sane, S. P. and Dickinson, M. H. (2002). The aerodynamic effects of wing rotation and a revised quasi-steady model of flapping flight. *J. Exp. Biol.* **205**, 1087-1096.
- Smith, C. W., Herbert, R., Wootton, R. J., and Evans, K. E. (2000). The hind wing of the desert locust (*Schistocerca gregaria* Forskål). II. Mechanical properties and functioning of the membrane. *J. Exp. Biol.* **203**, 2933-2943.
- Smith, M. J. C. (1996). Simulating moth wing aerodynamics: towards the development of flapping-wing technology. *AIAA Journal* **34**(7), 1348-1355.
- Smith, M. J. C., Wilkin, P. J., and Williams, M. H. (1996). The advantages of an unsteady panel method in modelling the aerodynamic forces on rigid flapping wings. *J. Exp. Biol.* **199**, 1073-1083.
- Sneyd, A. D., Bundock, M. S. and Reid, D. (1982). Possible effects of wing flexibility on the aerodynamics of *Pteranodon*. *Am. Nat.* **120**(4), 455-477.
- Somps, C. and Luttges, M. (1985). Dragonfly flight: novel uses of unsteady separated flows. *Science* **228**, 1326-1329.
- Song, D., Wang, H., Zeng, L., and Yin, C. (2001). Measuring the camber deformation of a dragonfly wing using projected comb fringe. *Review of Scientific Instruments* **72**(5), 2450-2454.
- Spedding, G. R. (1992). The aerodynamics of flight. In *Advances in Comparative and Environmental Physiology, Vol. 11*. (ed. R. McN. Alexander), pp. 51-111. New York: Springer-Verlag.
- Steppan, S. J. (2000). Flexural stiffness patterns of butterfly wings (Papilionoidea). *J. Res. Lepid.* **35**, 61-77.
- Sullivan, K. (1979). Mechanical aspects of swimming in the ratfish, *Hydrolagus collicii*. *Friday Harbor Laboratories Biomechanics (Zool. 533b) course papers*, 1-28.
- Sunada, S., Zeng, L., and Kawachi, K. (1998). The relationship between dragonfly wing structure and torsional deformation. *J. Theor. Biol.* **193**, 39-45.
- Swartz, S. M., Bennett, M. B., and Carrier, D. R. (1992). Wing bone stresses in free flying bats and the evolution of skeletal design for flight. *Nature* **359** (6397), 726-729.

- Timoshenko, S., Young, D. H. and Weaver Jr., W. (1974). *Vibration Problems in Engineering*. New York: John Wiley & Sons.
- Trimble, A. C. (2001). Musculoskeletal control of flight in the hawkmoth *Manduca sexta*. Thesis (Ph.D.), University of Washington.
- Trueman, J. W. H. and Rowe, R. J. (2001). Odonata. In *The Tree of Life Web Project*, (ed. D. R. Maddison and K.-S. Schultz). <http://tolweb.org/tree/phylogeny.html>
- Tong, B.-J., Zhuang, L.-X. and Cheng, J.-Y. (1993). The hydrodynamic analysis of fish propulsion performance and its morphological adaptation. *Sadhana* **18** (3&4), 719-728.
- Tu, M. S. and Daniel, T. L. (in prep). Cardiac-like behavior in an insect flight muscle.
- Tu, M. S. and Dickinson, M. H. (1994). Modulation of negative work output from a steering muscle of the blowfly, *Calliphora vicina*. *J. Exp. Biol.* **192**, 207-224.
- Vest, M. S. and Katz, J. (1996). Unsteady aerodynamic model of flapping wings. *AIAA Journal* **34**(7), 1435-1440.
- Wainwright, S. A., Biggs, W. D., Currey, J. D. and Gosline, J. M. (1982). *Mechanical Design in Organisms*. Princeton, New Jersey: Princeton University Press.
- Wakeling, J. M. and Ellington, C. P. (1997a). Dragonfly flight. I. Gliding flight and steady-state aerodynamic forces. *J. Exp. Biol.* **200**, 543-556.
- Wakeling, J. M. and Ellington, C. P. (1997b). Dragonfly flight. II. Velocities, accelerations and kinematics of flapping flight. *J. Exp. Biol.* **200**, 557-582.
- Wakeling, J. M. and Ellington, C. P. (1997c). Dragonfly flight. III. Lift and power requirements. *J. Exp. Biol.* **200**, 583-600.
- Walker, J. A. (2000). Does a rigid body limit maneuverability? *J. Exp. Biol.* **203**, 3391-3396.
- Webb, P. W. (1973). Kinematics of pectoral fin propulsion in *Cymatogaster aggregata*. *J. Exp. Biol.* **59**, 697-710.
- Weis-Fogh, T. (1975). Flapping flight and power in birds and insects, conventional and novel mechanisms. In *Swimming and Flying in Nature*. (ed. T. Y. Wu, C. J. Brokaw and C. J. Brennen), pp. 729-762. New York: Plenum Press.

Whiting, M. F., Carpenter, J. C., Wheeler, Q. D., and Wheeler, W. C. (1997). The Strepsiptera problem: Phylogeny of the holometabolous insect orders inferred from 18s and 28s ribosomal DNA sequences and morphology. *Syst. Biol.* **46**(1), 1-68.

Wiegmann, B. M. and Yeates, D. K. (1996). Diptera. In *The Tree of Life Web Project*, (ed. D. R. Maddison and K.-S. Schultz). <http://tolweb.org/tree/phylogeny.html>

Wilkin, P. J. and Williams, M. H. (1993). Comparison of the aerodynamic forces on a flying sphingid moth with those predicted by quasi-steady theory. *Physiol. Zool.* **66**(6), 1015-1044.

Willmott, A. P. and Ellington, C. P. (1997a). The mechanics of flight in the hawkmoth *Manduca sexta*. I. Kinematics of hovering and forward flight. *J. Exp. Biol.* **200**, 2705-2722.

Willmott, A. P. and Ellington, C. P. (1997b). The mechanics of flight in the hawkmoth *Manduca sexta*. II. Aerodynamic consequences of kinematic and morphological variation. *J. Exp. Biol.* **200**, 2723-2745.

Wootton, R. J. (1981). Support and deformability in insect wings. *J. Zool., Lond.* **193**, 447-468.

Wootton, R. J. (1990a). The mechanical design of insect wings. *Scientific American* **Nov**, 114-120.

Wootton, R. J. (1990b). Major insect radiations. In *Major Evolutionary Radiations* (ed. P. D. Taylor and G. P. Larwood), Systematics Association Special Volume No. 42, pp. 187-208. Oxford: Clarendon Press.

Wootton, R. J. (1991). The functional morphology of the wings of Odonata. *Adv. Odonatol.* **5**, 153-169.

Wootton, R. J. (1992). Functional morphology of insect wings. *Annu. Rev. Ent.* **37**, 113-140.

Wootton, R. J. (1993). Leading edge section and asymmetric twisting in the wings of flying butterflies (Insecta, Papilionoidea). *J. Exp. Biol.* **180**, 105-117.

Wootton, R. J. (1995). Geometry and mechanics of insect hindwing fans: a modelling approach. *Proc. R. Soc. Lond. B* **262**, 181-187.

Wootton, R. J. (1999). Invertebrate paraxial locomotory appendages: design, deformation and control. *J. Exp. Biol.* **202**, 3333-3345.

Wootton, R. J., Evans, K. E., Herbert, R., and Smith, C. W. (2000). The hind wing of the desert locust (*Schistocerca gregaria* Forskål). I. Functional morphology and mode of operation. *J. Exp. Biol.* **203**, 2921-2931.

Worcester, S. E. (1996). The scaling of the size and stiffness of primary flight feathers. *J. Zool., Lond.* **239**, 609-624.

Wu, T. Y. (1971). Hydromechanics of swimming propulsion. Part 1. Swimming of a two dimensional flexible plate at variable forward speeds in an inviscid fluid. *J. Fluid Mech.* **46**, 337-355.

Zanker, J. M. and Gotz, K. G. (1990). The wing beat of *Drosophila melanogaster*. II. Dynamics. *Phil. Trans. R. Soc. Lond. B* **327**, 19-44.

Appendix 1: Derivation of fluid-dynamic equations for Chapter 2
(Combes and Daniel, 2001; from Daniel, 1987)

Each segment of the wing is treated as a harmonically oscillating flexible plate centered at the origin. Its motion is prescribed by equation (2.1). The solution of Wu (Wu, 1971) to Euler's equation requires a Fourier representation of the position and velocity of all points on the wing:

$$h(x,t) = \frac{\beta_0}{2} + \sum_{n=1}^{\infty} \beta_n \cos(n\theta) \quad (\text{A1})$$

where

$$\beta_n = \frac{2}{\pi} \int_0^{\pi} h(x,t) \cos(n\theta) d\theta \quad (\text{A2})$$

and

$$V(x,t) = \frac{b_0}{2} + \sum_{n=1}^{\infty} b_n \cos(n\theta) \quad (\text{A3})$$

where

$$b_n = \frac{2}{\pi} \int_0^{\pi} V(x,t) \cos(n\theta) d\theta \quad (\text{A4})$$

β represents the Fourier coefficients for wing position, b represents the Fourier coefficients for wing velocity, θ is a variable in the Fourier representation and $V(x,t)$ is the vertical velocity at all points on the surface of the wing, which is given by the material derivative of the instantaneous wing position:

$$V(x,t) = \left(\frac{\partial}{\partial t} + U \frac{\partial}{\partial x} \right) h(x,t) \quad (\text{A5})$$

where U is the forward velocity. From these Fourier representations, Wu (Wu, 1971) provides equations for the time-averaged thrust, energy and power coefficients, here defined as:

$$C_p = \frac{P_{\text{avg}}}{\frac{1}{2} \rho \pi U^3 l} = \text{Re} \left\{ \left(\frac{-i\sigma}{U} \right) (b_0 + b_1) [(\beta_0^* - \beta_1^*) \Theta(\sigma) + \beta_1^*] \right\} \quad (\text{A6})$$

where the asterisk denotes the complex conjugate of the parameter. P_{avg} is the mean power expenditure, $\Theta(\sigma)$ is Theodorsen's function (defined below), Re indicates the real part of the enclosed function and ρ is the density of the fluid. C_p is a dimensionless coefficient that represents the total rate at which energy is expended to produce thrust and create vorticity in the wake behind the wing. This latter form of energy dissipation arises from the existence of a jump in the tangential velocity of flow at the trailing edge of the wing. The coefficient for the rate of energy loss by this mechanism is given by:

$$C_E = \frac{E_{\text{avg}}}{\frac{1}{2} \rho \pi U^3 l} = \frac{B(\sigma)(b_0 + b_1)(b_0^* + b_1^*)}{U^2} \quad (\text{A7})$$

where E_{avg} is the mean energy expended in the wake and $B(\sigma)$ is a modified Theodorsen's function. Two functions in Equations A6 and A7 depend on the degree of unsteadiness

in the motion. This unsteadiness is given by the parameter σ , called the reduced frequency parameter, which is a measure of the amount of vertical oscillation relative to forward steady motion:

$$\sigma = \frac{\omega l}{U} \quad (\text{A8})$$

The two functions of this parameter, $B(\sigma)$ and $\Theta(\sigma)$, set the time lag in the growth of circulation around the wing. The latter is called Theodorsen's function and is a complex combination of Bessel functions. The former represents portions of Theodorsen's function:

$$\Theta(\sigma) = F + iG = \frac{K_1(i\sigma)}{K_0(i\sigma) + K_1(i\sigma)} \quad (\text{A9})$$

and

$$B(\sigma) = F - (F^2 + G^2) \quad (\text{A10})$$

where F is the real part of Theodorsen's function, G is the imaginary part of Theodorsen's function, i is equal to the square root of -1 , and K_0 and K_1 are modified Bessel functions. The function $\Theta(\sigma)$ declines asymptotically from a value of i at $\sigma = 0$ to a value of 0.5 as σ tends to infinity (see Lighthill, 1975). Finally, a coefficient of thrust may be defined by the difference in the coefficients for total power expended and energy lost:

$$C_T = C_P - C_E \quad (\text{A11})$$

with an efficiency parameter defined as the rate of useful work done to total power expended:

$$\eta = \frac{C_T}{C_P} \quad (\text{A12})$$

Following the appropriate manipulations of the above equations, we arrive at expressions for the coefficients in terms of various Bessel functions. Below are simplified versions of the resultant equations:

$$C_E = \frac{4\beta(\sigma)(\phi_1^2 + \phi_2^2)}{U^2} \quad (\text{A13})$$

$$C_P = \frac{4\omega(\psi_1\phi_2 + \phi_1\psi_2)}{U^2} \quad (\text{A14})$$

where

$$\phi_1 = U\epsilon J_0(\alpha) + (1 - U/c)\omega J_1(\alpha)(h_0 + 2\epsilon) \quad (\text{A15})$$

$$\phi_2 = -U\epsilon J_1(\alpha) + (1 - U/c)\omega[(h_0 + \epsilon)J_0(\alpha) + \mu] \quad (\text{A16})$$

$$\zeta_1 = (h_0 + \epsilon)J_0(\alpha) - \mu \quad (\text{A17})$$

$$\zeta_2 = -J_1(\alpha)h_0 \quad (\text{A18})$$

$$\psi_1 = \zeta_1 F - \zeta_2 G + \mu \quad (\text{A19})$$

$$\psi_2 = \zeta_1 G + \zeta_2 F + (h_0 + \epsilon)J_1(\alpha) \quad (\text{A20})$$

$$\mu = \frac{\epsilon[J_0(\alpha) - J_2(\alpha)]}{2} \quad (\text{A21})$$

$$\alpha = \frac{\omega l}{c} \quad (\text{A22})$$

and where J_n is a Bessel function of order n . The central point of these equations is that the performance of this two-dimensional strip, as defined by the coefficients in Equations A11, A13, and A14, depends in a complex manner upon Bessel functions of the parameter α . This parameter is a measure of the number of propulsive waves present on the wing at any instant in time.

Appendix 2: Derivation of wing shape equations for Chapter 2
(Combes and Daniel, 2001)

Wings generated with a polynomial distribution were created using equations from Ellington (1984b):

$$\hat{c} = a_0 + a_1\hat{r} + a_2\hat{r}^2 + a_3\hat{r}^3 \quad (\text{A23})$$

where \hat{c} is the non-dimensional chord length at any position \hat{r} along the non-dimensional span. The coefficients a_0 - a_3 are found by solving the set of simultaneous equations:

$$\hat{r}_k^k = \frac{a_0}{k+1} + \frac{a_1}{k+2} + \frac{a_2}{k+3} + \frac{a_3}{k+4} \quad (\text{A24})$$

with $k = 0, 1, 2$ and 3 and where \hat{r}_k is the radius of the k th moment of area. The first moment of area was taken to be 0.4 (as measured on the ratfish fins) and the second and third moments of area were found from the equations (Ellington, 1984b):

$$\hat{r}_2 = 0.929(\hat{r}_1)^{0.732} \quad (\text{A25})$$

$$\hat{r}_3 = 0.900(\hat{r}_1)^{0.581} \quad (\text{A26})$$

Wings generated with a Beta distribution were also created with equations from Ellington (1984b). The Beta distribution is defined for x from 0 to 1 as:

$$f(B) = \frac{x^{p-1}(1-x)^{q-1}}{B(p,q)} \quad (\text{A27})$$

where the Beta function $B(p,q)$ is

$$B(p,q) = \int_0^1 x^{p-1}(1-x)^{q-1} dx \quad (\text{A28})$$

integrated from 0 to 1 . Ellington (1984b) equated f to \hat{c} , the non-dimensional chord length and x to \hat{r} , the non-dimensional span. He then defined the parameters p and q as:

$$p = \hat{r}_1 \left[\frac{\hat{r}_1(1-\hat{r}_1)}{(\hat{r}_2^2 - \hat{r}_1^2)} - 1 \right] \quad (\text{A29})$$

$$q = (1-\hat{r}_1) \left[\frac{\hat{r}_1(1-\hat{r}_1)}{(\hat{r}_2^2 - \hat{r}_1^2)} - 1 \right] \quad (\text{A30})$$

where \hat{r}_1 is the radius of the first moment of area and \hat{r}_2 is the radius of the second moment of area (found using equation (25), as above).

The last series of wings was created with an exponential equation of the form (Daniel, 1987):

$$l(z) = l_0 [1 - (z/z_0)^a] \quad (\text{A31})$$

where l_0 is the half chord length at the base, z_0 is the span of the wing, and $l(z)$ describes the half chord length at various local positions along the span. The exponent a was varied from 0.01 to 4 to change the shape of the wing.

Appendix 3: Matlab code for Chapter 3

calculation of vein density

veindensity.m

last modified 4/10/00

```
clear all;
A = imread('Manduca_veins.bmp','bmp');
Q = double(A);
[i,j] = find(Q == 1 );
clear Q;
veinpixels = length(i)
[a,b] = find(A > 1);
clear A;
veinmistakes = length(a)
A = imread('Manduca_area.bmp','bmp');
Q = double(A);
[i,j] = find(Q == 1 );
clear Q;
areapixels = length(i)
[a,b] = find(A > 1);
clear A;
areamistakes = length(a)
A = imread('Manduca_scale.bmp','bmp');
Q = double(A);
[i,j] = find(Q == 1 );
clear Q;
scalepixels = length(i)
[a,b] = find(A > 1);
clear A;
scalemistakes = length(a)
pixellength = 0.5/scalepixels;
pixelarea = pixellength*pixellength;
veinarea = veinpixels*pixelarea
area = areapixels*pixelarea
veindens = veinarea/area
```

calculation of vein thickness

skeletonize.m

last modified 4/6/00

```
%read image, convert from unit8 to 0/1 and skeletonize
```

```

clear all;
A = imread('Manduca_veins.bmp','bmp');
C = double(A);
%clear A;
M = double(bwmorph(C,'thin',Inf));
clear C;
%shift to the right, multiply by original, and sum
[m,n] = size(M);
Mrcut = M(:,1:n - 1);
Mr = [zeros(m,1) Mrcut];
clear Mrcut;
Mrmult = M.*Mr;
clear Mr;
rneigh = sum(sum(Mrmult))
clear Mrmult;
%shift down, multiply, and sum
Mdcut = M(1:m - 1,:);
Md = [zeros(1,n); Mdcut];
clear Mdcut;
Mdmult = M.*Md;
clear Md;
dneigh = sum(sum(Mdmult))
clear Mdmult;
%shift to the right diagonal down, multiply, and sum
Mdr1 = M(1:m - 1,1:n - 1);
Mdr = [zeros(1,n-1); Mdr1];
clear Mdr1;
Mdrmult = M.*Mdr;
clear Mdr;
drneigh = sum(sum(Mdrmult))
clear Mdrmult;
%shift to the left diagonal down, multiply, and sum
Mdlcut = M(1:m - 1,2:n);
Mdlcut(:,n) = zeros(m-1,1);
Mdl = [zeros(1,n); Mdlcut];
clear Mdlcut;
Mdlmult = M.*Mdl;
clear Mdl;
dlneigh = sum(sum(Mdlmult))
%find length of pixel side and diagonal
A = imread('Manduca_scale.bmp','bmp');
B = double(A); clear A;

```

```

[i,j] = find(B == 1 ); clear B;
scalepixels = length(i);
pixellength = 0.5/scalepixels
pixeldiag = pixellength*(sqrt(2))
%find total vein length
veinlength =
(rneigh*pixellength)+(dneigh*pixellength)+(drneigh*pixeldiag)+(dlneigh*pixeldiag)
%find area of veins
A = imread('Manduca_veins.bmp','bmp');
Q = double(A);
[i,j] = find(Q == 1 );
clear Q;
veinpixels = length(i)
[a,b] = find(A > 1);
clear A;
veinmistakes = length(a)
pixelarea = pixellength*pixellength;
veinarea = veinpixels*pixelarea
veinthick = veinarea/veinlength

```

calculation of percent lead veins

leadveinpercent.m
last modified 6/7/00

```

clear all;
A = imread('Manduca_leadveins.bmp','bmp');
Q = double(A);
[i,j] = find(Q == 1 );
clear Q;
leadveinpixels = length(i)
[a,b] = find(A > 1);
clear A;
leadveinmistakes = length(a)
A = imread('Manduca_veins.bmp','bmp');
Q = double(A);
[i,j] = find(Q == 1 );
clear Q;
veinpixels = length(i)
[a,b] = find(A > 1);
clear A;
veinmistakes = length(a)
A = imread('Manduca_scale.bmp','bmp');

```

```

Q = double(A);
[i,j] = find(Q == 1 );
clear Q;
scalepixels = length(i)
[a,b] = find(A > 1);
clear A;
scalemistakes = length(a)
pixellength = 0.5/scalepixels;
pixelarea = pixellength*pixellength;
leadveinarea = leadveinpixels*pixelarea
veinarea = veinareapixels*pixelarea
percentveins = leadveinarea/veinarea
*****

```

calculation of leading edge vein density

leadveindensity.m

last modified 5/24/00

```

clear all;
A = imread('Manduca_leadveins.bmp','bmp');
Q = double(A);
[i,j] = find(Q == 1 );
clear Q;
leadveinpixels = length(i);
[a,b] = find(A > 1);
clear A;
leadveinmistakes = length(a);
A = imread('Manduca_leadarea.bmp','bmp');
Q = double(A);
[i,j] = find(Q == 1 );
clear Q;
leadareapixels = length(i);
[a,b] = find(A > 1);
clear A;
leadareamistakes = length(a);
A = imread('Manduca_scale.bmp','bmp');
Q = double(A);
[i,j] = find(Q == 1 );
clear Q;
scalepixels = length(i);
[a,b] = find(A > 1);
clear A;
scalemistakes = length(a);
pixellength = 0.5/scalepixels;

```

```
pixelarea = pixellength*pixellength;  
leadveinarea = leadveinpixels*pixelarea  
leadarea = leadareapixels*pixelarea  
leadveindens = leadveinarea/leadarea
```


Appendix 4: Matlab code for Chapter 4

code to find the center of laser lines on z-calibration steps

findcaliblines.m

by S.A. Combes and A.C. Trimble

last modified 4/28/01

```

clear all;
colormap(gray);

bugnumber = 19;
cs = 'span';
dv = 'vent';
lr = 'R';
bug = 'manduca';
bugabb = 'mand';
computer = 'Combseyland';

imageplace =
[computer,':Stacey:wing/laser2000:',bug,num2str(bugnumber),':cs,':cut_images'];
image_name = [bugabb,num2str(bugnumber),cs,'_calib3',lr,dv,'.jpg'];
calib_name = [bugabb,num2str(bugnumber),cs,'_calib3',lr,dv,'.jpg'];
cd(imageplace);

params = [736 1159 142 1214 1650 79 1 60 3.15];
column_start = params(1);
column_end = params(2);
start_row = params(3);
column_start2 = params(4);
column_end2 = params(5);
start_row2 = params(6);
all_lines = params(7);
line_pixel_width = params(8);
sheet_thick = params(9);

%READ THE IMAGE
image = imread(image_name,'jpg');
%READ THE CALIBRATION IMAGE
% calib_name = input('What calibration do you want? ','s');
calib = imread(calib_name,'jpg');

home = 'Combseyland:Stacey:wing/laser2000:bending_code';
cd(home);

```

```

%DISPLAY THE IMAGE
imagesc(image)

%GET ONE COMPONENT OF THE IMAGES
oneband = image(:,:,1);
calib_oneband = calib(:,:,1);

%WE NEED PLACES TO STORE SOME STUFF

global line_xsection;
global yin;
global initguess;
global COLM;

line_xsection = ones(line_pixel_width,2,(column_end - column_start + 2));
lines = zeros((column_end - column_start), 2, all_lines);

calib_lines = zeros((column_end2 - column_start2), 2, all_lines);

%*****FOR LEFT LINE *****

%START LINE DETECTION AT LINE #1 (=incr)
%LOOP FOR ALL LINES
incr = 1;
while incr <= all_lines;
    column = column_start;
    COLM=3;
    meanCOLM = mean(line_xsection(:,1,COLM));
    meanCOLM2 = meanCOLM;
    %jump forward to the correct row to begin searching at the beginning of each line
    (incr)
    if incr == 1;
        row = start_row;
    else;
        row = round(lines(1, 2, (incr - 1)) + (0.2 * line_pixel_width));
    end;
    % set the initial guess for the fmins to be near the right place
    initguess = [(row + (0.2 * line_pixel_width)) 1 2];
    %while column <= column_end;
    while ((meanCOLM / meanCOLM2) > 0.4); %GO until mean test fails...
        %READ A LINE X_SECTION
        patch = 0;
        while patch < line_pixel_width;
            line_xsection((patch+1),1,COLM) = oneband((row + patch), column);

```

```

line_xsection((patch+1),2,COLM) = (row + patch);
patch = patch + 1;
end;

%COMPUTE THE PEAK OF THIS PATCH
%CALCULATE A GAUSSIAN LEAST_SQUARES FIT TO THE PIXEL
INTENSITIES
[final_Mu, nextguess] = gausstest(line_xsection, initguess, COLM);
local_peak_row = final_Mu;
initguess = nextguess;

%check for nonsensical return from fmins...
%and check again... for a peak pos. outside the sample range.
%if (local_peak_row - row) < 0; it really shouldn't be outside the sample...
    if (local_peak_row < row); %it really shouldn't below the sample...
        lines(((column+1)- column_start), 1, incr) = 0;
        lines(((column+1)- column_start), 2, incr) = 0;
        column = column + 1;
        COLM = COLM + 1;
        break;
    end;
    if (local_peak_row - row) > line_pixel_width:
%it really shouldn't be outside the sample...
        lines(((column+1)- column_start), 1, incr) = 0;
        lines(((column+1)- column_start), 2, incr) = 0;
        column = column + 1;
        COLM = COLM + 1;
        break;
    end;
%end;

%WRITE LOCAL LINE POSITION
% as (column, row, line) where column and line are integers and row is the "height"
lines(((column+1)- column_start), 1, incr) = (column);
lines(((column+1)- column_start), 2, incr) = (local_peak_row);
%RE-ESTIMATE THE LOCATION OF THE PATCH SEARCH BASED ON THE
CURRENT PEAK LOCATION
row = round(local_peak_row - (0.2 * line_pixel_width));
if COLM >= 7;
    meanCOLM = mean(line_xsection(:,1,COLM));
    meanCOLM2 = mean(line_xsection(:,1,COLM-4));
end;
column = column + 1
if column == column_end;

```

```

        break;
    end;
    COLM = COLM + 1;
end;

%SETUP FOR NEXT LINE
incr = incr + 1;
hold on;
%TEST HERE FOR NON_ZERO DATA TO PLOT
nonzeroX = find(lines(:,1,(incr - 1)) > 0);
plot(lines(nonzeroX,1,(incr - 1)), lines(nonzeroX,2,(incr - 1)), 'r')
drawnow;
end;

%***** END OF LEFT LINE MEASURE *****
%
%*****
%
%*****START RIGHT LINE MEASURE*****
line_xsection(:,,:) = 1;
%START LINE DETECTION AT LINE #1 (=incr)
%LOOP FOR ALL LINES
incr = 1;
while incr <= all_lines;
    column = column_start2;
    COLM=3;
    meanCOLM = mean(line_xsection(:,1,COLM));
    meanCOLM2 = meanCOLM;
    %jump forward to the correct row to begin searching at the beginning of each line
    (incr)
    if incr == 1;
        row = start_row2;
    else;
        row = round(calib_lines(1, 2, (incr - 1)) + (0.2 * line_pixel_width));
    end;
    % set the initial guess for the fmins to be near the right place
    initguess = [(row + (0.2 * line_pixel_width)) 1 2];
    %while column <= column_end; fixed line search end point...
    while ((meanCOLM / meanCOLM2) > 0.35); %GO until mean test fails...
        %READ A LINE X_SECTION
        patch = 0;
        while patch < line_pixel_width;
            line_xsection((patch+1),1,COLM) = calib_oneband((row + patch), column);
            line_xsection((patch+1),2,COLM) = (row + patch);

```

```

    patch = patch + 1;
    end;

    %COMPUTE THE PEAK OF THIS PATCH
    %CALCULATE A GAUSSIAN LEAST_SQUARES FIT TO THE PIXEL
    INTENSITIES
    [final_Mu, nextguess] = gausstest(line_xsection, initguess, COLM);
    local_peak_row = final_Mu;
    initguess = nextguess;

    %check for nonsensical return from fmins...
    %and check again... for a peak pos. outside the sample range.
    if (local_peak_row < row); %it really shouldn't be outside the sample...
        calib_lines(((column+1)- column_start2), 1, incr) = 0;
        calib_lines(((column+1)- column_start2), 2, incr) = 0;
        column = column + 1;
        COLM = COLM + 1;
        break;
    end;
    if (local_peak_row - row) > line_pixel_width;
    %it really shouldn't be outside the sample...
        calib_lines(((column+1)- column_start2), 1, incr) = 0;
        calib_lines(((column+1)- column_start2), 2, incr) = 0;
        column = column + 1;
        COLM = COLM + 1;
        break;
    end;
    %end;

    %WRITE LOCAL LINE POSITION
    % as (column, row, line) where column and line are integers and row is the "height"
    calib_lines(((column+1) - column_start2), 1, incr) = (column);
    calib_lines(((column+1) - column_start2), 2, incr) = (local_peak_row);
    %RE-ESTIMATE THE LOCATION OF THE PATCH SEARCH BASED ON THE
    CURRENT PEAK LOCATION
    row = round(local_peak_row - (0.2 * line_pixel_width));
    if COLM >= 7;
        meanCOLM = mean(line_xsection(:,1,COLM));
        meanCOLM2 = mean(line_xsection(:,1,COLM-4));
    end;
    column = column + 1
    if column == column_end2;
        break;
    end;
end;

```

```

        COLM = COLM + 1;
    end;

    %NEXT LINE
    incr = incr + 1;
    hold on;
    %TEST HERE FOR NON_ZERO DATA TO PLOT
    calib_nonzero = find(calib_lines(:,1,(incr - 1)) > 0);
    plot(calib_lines(calib_nonzero,1,(incr - 1)), calib_lines(calib_nonzero,2,(incr - 1)), 'g')
    drawnow;
end;

fileplace =
[computer,':Stacey:wing/laser2000:',bug,num2str(bugnumber),',',cs,':calibrations'];
filename = [bugabb,num2str(bugnumber),cs,'_calib3',lr,dv, '.mat']
cd(fileplace)
save(filename, 'lines', 'calib_lines', 'sheet_thick');

```

calculation of z-displacement calibration

caliblinestodepth.m

last modified 11/21/01

%COMPUTE CALIBRATION OFFSETS

**%TO CALCULATE THE PIXEL OFFSET IN THE Y-DIRECTION FOR MICRON
DEPTH IN THE Z DIRECTION:**

clear all;

```

bugnumber = 8;
cs = 'chord';
dv = 'vent';
lr = 'R';
bug = 'manduca';
bugabb = 'mand';
computer = 'Combseyland';

```

midpoint = 1095;

dataplace =

```

[computer,':Stacey:wing/laser2000:',bug,num2str(bugnumber),',',cs,':calibrations'];
cd(dataplace);
dataname = [bugabb,num2str(bugnumber),cs,'_calib3',lr,dv, '.mat'];

```

```

load(dataname);

%IF THERE IS ONLY ONE LINE:
%fit a first degree polynomial the first half of one line, then second half

line1x = lines(:,1);
line1y = lines(:,2);
polyorder = 1;
polyline1 = polyfit(line1x, line1y, polyorder);
slopeline1 = polyline1(1);
xpolyline1 = line1x(1):5:line1x(size(line1x));
ypolyline1 = polyval(polyline1, xpolyline1);
calibline1x = calib_lines(:,1);
calibline1y = calib_lines(:,2);
polycalibline1 = polyfit(calibline1x, calibline1y, polyorder);
slopecalib1 = polycalibline1(1);
xpolycalibline1 = calibline1x(1):5:calibline1x(size(calibline1x));
ypolycalibline1 = polyval(polycalibline1, xpolycalibline1);
avgslope = (slopeline1 + slopecalib1)/2;

figure
title ('polynomial fit to calibration slide')
plot(line1x, line1y, calibline1x, calibline1y, xpolyline1, ypolyline1, xpolycalibline1,
ypolycalibline1)

yposline1 = (polyline1(1)*midpoint) + polyline1(2);
yposcalibline1 = (polycalibline1(1)*midpoint) + polycalibline1(2);
offset1 = abs(yposline1 - yposcalibline1)
mic_per_Z1 = (sheet_thick * 1000.0) / offset1

fileplace =
[computer,':Stacey:wing/laser2000:',bug,num2str(bugnumber),':',cs,':calibrations'];
filename = [bugabb,num2str(bugnumber),cs,'_cal3',lr,dv,'depth.mat'];
cd(fileplace)
save(filename, 'slopeline1', 'slopecalib1', 'avgslope', 'polyline1', 'polycalibline1',
'midpoint', 'offset1', 'mic_per_Z1');

```

code to prepare wing images for Matlab (trim and change to grayscale)

preimage.m

last modified 11/12/01

```

clear all;
colormap(gray);

bug = 'manduca';
bugabb = 'mand';
bugnumber = 11;
cs = 'span';
dv = 'vent';
computer = 'Combseyland';

newheight = 900;
newheightfixtop = 400;
newwidth = 1800;
newwidthfixright = 1800;

camerainages =
[computer,':Stacey:wing/laser2000:',bug,num2str(bugnumber),',',cs,':camera_images'];
cd(camerainages);

%READ THE IMAGE AND CHANGE TO GRAYSCALE
image_name =input('What image do you want? ','s');
image = imread(image_name,'jpg');
imagegray = (image(:,:,1));
width = length(imagegray(1,:));
height = length(imagegray(:,1));

%CLIP WIDTH (L/R)
clipLR = (width - newwidth)/2;
imageclipwidth = imagegray(:,(1+clipLR):(length(imagegray(1,:))-clipLR));

%CLIP WIDTH (FIX RIGHT)
clipLRfixR = newwidth - newwidthfixright;
% imageclipfixR = imageclipwidth(:,1:(length(imageclipwidth(1,:))-clipLRfixR));
imageclipfixR = imageclipwidth(:,clipLRfixR:(length(imageclipwidth(1,:)))));

%CLIP HEIGHT (TOP/BOTTOM)
cliptopbot = (height - newheight)/2;
imagecliptopbot = imageclipfixR((1+cliptopbot):(length(imageclipfixR(:,1))-
cliptopbot),:);

%CLIP HEIGHT (FIX TOP)
clipfixtop = newheight - newheightfixtop;
% imageclipfixtop = imagecliptopbot(1:(length(imagecliptopbot(:,1))-clipfixtop),:);

```



```

%(FIX BOTTOM):
imageclipfixtop = imageclipfixR(clipfixtop:(length(imagecliptopbot(:,1))),:);

```

```

%LOOP FOR ALL IMAGES:

```

```

image1 = [bugabb,num2str(bugnumber),cs,'_zero1',dv,'.jpg'];
image2 = [bugabb,num2str(bugnumber),cs,'_zero1',dv,'_lt.jpg'];
image3 = [bugabb,num2str(bugnumber),cs,'_load1',dv,'.jpg'];
image4 = [bugabb,num2str(bugnumber),cs,'_load1',dv,'_lt.jpg'];
image5 = [bugabb,num2str(bugnumber),cs,'_zero2',dv,'.jpg'];
image6 = [bugabb,num2str(bugnumber),cs,'_zero2',dv,'_lt.jpg'];
image7 = [bugabb,num2str(bugnumber),cs,'_load2',dv,'.jpg'];
image8 = [bugabb,num2str(bugnumber),cs,'_load2',dv,'_lt.jpg'];
image9 = [bugabb,num2str(bugnumber),cs,'_zero3',dv,'.jpg'];
image10 = [bugabb,num2str(bugnumber),cs,'_zero3',dv,'_lt.jpg'];
image11 = [bugabb,num2str(bugnumber),cs,'_load3',dv,'.jpg'];
image12 = [bugabb,num2str(bugnumber),cs,'_load3',dv,'_lt.jpg'];
image13 = [bugabb,num2str(bugnumber),cs,'_zero4',dv,'.jpg'];
image14 = [bugabb,num2str(bugnumber),cs,'_zero4',dv,'_lt.jpg'];
image15 = [bugabb,num2str(bugnumber),cs,'_load4',dv,'.jpg'];
image16 = [bugabb,num2str(bugnumber),cs,'_load4',dv,'_lt.jpg'];
image17 = [bugabb,num2str(bugnumber),cs,'_calib3L',dv,'.jpg'];
image18 = [bugabb,num2str(bugnumber),cs,'_calib3R',dv,'.jpg'];
image19 = [bugabb,num2str(bugnumber),cs,'_4mmgrid',dv,'.jpg'];
image20 = [bugabb,num2str(bugnumber),cs,'_2mmgrid',dv,'.jpg'];
% image17 = [bugabb,num2str(bugnumber),cs,'_calib3',dv,'.jpg'];
% image18 = [bugabb,num2str(bugnumber),cs,'_4mmgrid',dv,'.jpg'];
% image19 = [bugabb,num2str(bugnumber),cs,'_2mmgrid',dv,'.jpg'];

```

```

image_id{1} = image1;
image_id{2} = image2;
image_id{3} = image3;
image_id{4} = image4;
image_id{5} = image5;
image_id{6} = image6;
image_id{7} = image7;
image_id{8} = image8;
image_id{9} = image9;
image_id{10} = image10;
image_id{11} = image11;
image_id{12} = image12;
image_id{13} = image13;
image_id{14} = image14;
image_id{15} = image15;

```

```

image_id{16} = image16;
image_id{17} = image17;
image_id{18} = image18;
image_id{19} = image19;
image_id{20} = image20;

i = 1;
for i = 1:20;
    image_name = image_id{i};
    cd(cameraimages);

    %READ THE IMAGE AND CHANGE TO GRAYSCALE
    image = imread(image_name,'jpg');
    imagegray = (image(:,:,1));
    width = length(imagegray(1,:));
    height = length(imagegray(:,1));

    %CLIP WIDTH (L/R)
    clipLR = (width - newwidth)/2;
    imageclipwidth = imagegray(:,(1+clipLR):(length(imagegray(1,:))-clipLR));

    %CLIP WIDTH (FIX RIGHT)
    clipLRfixR = newwidth - newwidthfixright;
    %imageclipfixR = imageclipwidth(:,1:(length(imageclipwidth(1,:))-clipLRfixR));
    imageclipfixR = imageclipwidth(:,clipLRfixR:(length(imageclipwidth(1,:)))));

    %CLIP HEIGHT (TOP/BOTTOM)
    cliptopbot = (height - newheight)/2;
    imagecliptopbot = imageclipfixR((1+cliptopbot):(length(imageclipfixR(:,1))-
cliptopbot),:);

    %CLIP HEIGHT (FIX TOP)
    clipfixtop = newheight - newheightfixtop;
    %imageclipfixtop = imageclipfixR(1:(length(imagecliptopbot(:,1))-clipfixtop),:);
    %(FIX BOTTOM):
    imageclipfixtop = imageclipfixR(clipfixtop:(length(imagecliptopbot(:,1))),:);

    size(imageclipfixtop)
    imagesc(imageclipfixtop)

    fixedimages =
[computer,':Stacey:wing/laser2000:',bug,num2str(bugnumber),':',cs,':cut_images'];
    cd(fixedimages);

```

```

        imwrite(imageclipfixtop, image_name, 'jpg');
        i = i + 1;
end;

*****

code to locate the center of laser lines on wing images
findlineloop.m
by S.A. Combes and A.C. Trimble
last modified 11/13/01

clear all;
%*****CHANGE BUG NUMBER AND PARAMETERS!!!!!!***** *

bugnumber = 11;
bug = 'manduca';
bugabb = 'mand';
computer = 'Combseyland';
istart = 1;
istop = 16;

%****first set: chord dorsal*****
fixchdors = 'fixed';
params{1} = [200 55 1 160 16.2309 12.4429 0.00063358 1700 1686 99 1748 1831];
params{2} = [200 55 1 160 16.2309 12.4429 0.00152772 1700 1676 99 1748 1831];
params{3} = [200 55 1 160 16.2309 12.4429 0.00264437 1700 1661 99 1748 1831];
params{4} = [200 55 1 160 16.2309 12.4429 0.00390424 1700 1647 99 1748 1831];

dorschordplace =
[computer,':Stacey:wing/laser2000:',bug,num2str(bugnumber),':chord:cut_images'];
imagelocation{1} = dorschordplace;
imagelocation{2} = dorschordplace;
imagelocation{3} = dorschordplace;
imagelocation{4} = dorschordplace;

imageload1chdors = [bugabb,num2str(bugnumber),'chord_load1dors',fixchdors,'.jpg'];
imageload2chdors = [bugabb,num2str(bugnumber),'chord_load2dors',fixchdors,'.jpg'];
imageload3chdors = [bugabb,num2str(bugnumber),'chord_load3dors',fixchdors,'.jpg'];
imageload4chdors = [bugabb,num2str(bugnumber),'chord_load4dors',fixchdors,'.jpg'];
imagezero1chdors = [bugabb,num2str(bugnumber),'chord_zero1dors',fixchdors,'.jpg'];
imagezero2chdors = [bugabb,num2str(bugnumber),'chord_zero2dors',fixchdors,'.jpg'];
imagezero3chdors = [bugabb,num2str(bugnumber),'chord_zero3dors',fixchdors,'.jpg'];
imagezero4chdors = [bugabb,num2str(bugnumber),'chord_zero4dors',fixchdors,'.jpg'];
names{1,1} = imageload1chdors;

```

```

names{1,2} = imagezero1chdors;
names{2,1} = imageload2chdors;
names{2,2} = imagezero2chdors;
names{3,1} = imageload3chdors;
names{3,2} = imagezero3chdors;
names{4,1} = imageload4chdors;
names{4,2} = imagezero4chdors;

folderpath1chdors =
[computer,':Stacey:wing/laser2000:',bug,num2str(bugnumber),':chord:load1dors'];
folderpath2chdors =
[computer,':Stacey:wing/laser2000:',bug,num2str(bugnumber),':chord:load2dors'];
folderpath3chdors =
[computer,':Stacey:wing/laser2000:',bug,num2str(bugnumber),':chord:load3dors'];
folderpath4chdors =
[computer,':Stacey:wing/laser2000:',bug,num2str(bugnumber),':chord:load4dors'];
foldername{1} = folderpath1chdors;
foldername{2} = folderpath2chdors;
foldername{3} = folderpath3chdors;
foldername{4} = folderpath4chdors;

save1chdors = [bugabb,num2str(bugnumber),'chord_load1dors.mat'];
save2chdors = [bugabb,num2str(bugnumber),'chord_load2dors.mat'];
save3chdors = [bugabb,num2str(bugnumber),'chord_load3dors.mat'];
save4chdors = [bugabb,num2str(bugnumber),'chord_load4dors.mat'];
savename{1} = save1chdors;
savename{2} = save2chdors;
savename{3} = save3chdors;
savename{4} = save4chdors;

%*****second set: chord ventral*****
fixchvent = 'fixed';
params{5} = [165 95 1 150 14.0757 12.0706 0.00029944 1651 1647 70 1671 1738];
params{6} = [165 95 1 150 14.0757 12.0706 0.00092774 1651 1638 70 1671 1738];
params{7} = [165 95 1 150 14.0757 12.0706 0.00185336 1651 1627 70 1671 1738];
params{8} = [165 95 1 150 14.0757 12.0706 0.00295428 1651 1617 70 1671 1738];

ventchordplace =
[computer,':Stacey:wing/laser2000:',bug,num2str(bugnumber),':chord:cut_images'];
imagelocation{5} = ventchordplace;
imagelocation{6} = ventchordplace;
imagelocation{7} = ventchordplace;
imagelocation{8} = ventchordplace;

```

```

imageload1chvent = [bugabb,num2str(bugnumber),'chord_load1vent',fixchvent,'.jpg'];
imageload2chvent = [bugabb,num2str(bugnumber),'chord_load2vent',fixchvent,'.jpg'];
imageload3chvent = [bugabb,num2str(bugnumber),'chord_load3vent',fixchvent,'.jpg'];
imageload4chvent = [bugabb,num2str(bugnumber),'chord_load4vent',fixchvent,'.jpg'];
imagezero1chvent = [bugabb,num2str(bugnumber),'chord_zero1vent',fixchvent,'.jpg'];
imagezero2chvent = [bugabb,num2str(bugnumber),'chord_zero2vent',fixchvent,'.jpg'];
imagezero3chvent = [bugabb,num2str(bugnumber),'chord_zero3vent',fixchvent,'.jpg'];
imagezero4chvent = [bugabb,num2str(bugnumber),'chord_zero4vent',fixchvent,'.jpg'];
names{5,1} = imageload1chvent;
names{5,2} = imagezero1chvent;
names{6,1} = imageload2chvent;
names{6,2} = imagezero2chvent;
names{7,1} = imageload3chvent;
names{7,2} = imagezero3chvent;
names{8,1} = imageload4chvent;
names{8,2} = imagezero4chvent;

```

```

folderpath1chvent =
[computer,':Stacey:wing/laser2000:',bug,num2str(bugnumber),':chord:load1vent'];
folderpath2chvent =
[computer,':Stacey:wing/laser2000:',bug,num2str(bugnumber),':chord:load2vent'];
folderpath3chvent =
[computer,':Stacey:wing/laser2000:',bug,num2str(bugnumber),':chord:load3vent'];
folderpath4chvent =
[computer,':Stacey:wing/laser2000:',bug,num2str(bugnumber),':chord:load4vent'];
foldername{5} = folderpath1chvent;
foldername{6} = folderpath2chvent;
foldername{7} = folderpath3chvent;
foldername{8} = folderpath4chvent;

```

```

save1chvent = [bugabb,num2str(bugnumber),'chord_load1vent.mat'];
save2chvent = [bugabb,num2str(bugnumber),'chord_load2vent.mat'];
save3chvent = [bugabb,num2str(bugnumber),'chord_load3vent.mat'];
save4chvent = [bugabb,num2str(bugnumber),'chord_load4vent.mat'];
savename{5} = save1chvent;
savename{6} = save2chvent;
savename{7} = save3chvent;
savename{8} = save4chvent;

```

```

%****third set: span dorsal*****
fixspdors = 'fixed';
params{9} = [125 30 1 65 34.8428 28.4841 0.00168455 1710 1702 29 1757 1772];
params{10} = [125 30 1 65 34.8428 28.4841 0.00353109 1710 1693 29 1757 1772];
params{11} = [125 30 1 65 34.8428 28.4841 0.0053747 1710 1683 29 1757 1772];

```

```
params{12} = [125 30 1 65 34.8428 28.4841 0.00727722 1710 1673 29 1757 1772];
```

```
dorsspanplace =
```

```
[computer,':Stacey:wing/laser2000:',bug,num2str(bugnumber),':span:cut_images'];
```

```
imagelocation{9} = dorsspanplace;
```

```
imagelocation{10} = dorsspanplace;
```

```
imagelocation{11} = dorsspanplace;
```

```
imagelocation{12} = dorsspanplace;
```

```
imageload1spdors = [bugabb,num2str(bugnumber),'span_load1dors',fixspdors,'.jpg'];
```

```
imageload2spdors = [bugabb,num2str(bugnumber),'span_load2dors',fixspdors,'.jpg'];
```

```
imageload3spdors = [bugabb,num2str(bugnumber),'span_load3dors',fixspdors,'.jpg'];
```

```
imageload4spdors = [bugabb,num2str(bugnumber),'span_load4dors',fixspdors,'.jpg'];
```

```
imagezero1spdors = [bugabb,num2str(bugnumber),'span_zero1dors',fixspdors,'.jpg'];
```

```
imagezero2spdors = [bugabb,num2str(bugnumber),'span_zero2dors',fixspdors,'.jpg'];
```

```
imagezero3spdors = [bugabb,num2str(bugnumber),'span_zero3dors',fixspdors,'.jpg'];
```

```
imagezero4spdors = [bugabb,num2str(bugnumber),'span_zero4dors',fixspdors,'.jpg'];
```

```
names{9,1} = imageload1spdors;
```

```
names{9,2} = imagezero1spdors;
```

```
names{10,1} = imageload2spdors;
```

```
names{10,2} = imagezero2spdors;
```

```
names{11,1} = imageload3spdors;
```

```
names{11,2} = imagezero3spdors;
```

```
names{12,1} = imageload4spdors;
```

```
names{12,2} = imagezero4spdors;
```

```
folderpath1spdors =
```

```
[computer,':Stacey:wing/laser2000:',bug,num2str(bugnumber),':span:load1dors'];
```

```
folderpath2spdors =
```

```
[computer,':Stacey:wing/laser2000:',bug,num2str(bugnumber),':span:load2dors'];
```

```
folderpath3spdors =
```

```
[computer,':Stacey:wing/laser2000:',bug,num2str(bugnumber),':span:load3dors'];
```

```
folderpath4spdors =
```

```
[computer,':Stacey:wing/laser2000:',bug,num2str(bugnumber),':span:load4dors'];
```

```
foldername{9} = folderpath1spdors;
```

```
foldername{10} = folderpath2spdors;
```

```
foldername{11} = folderpath3spdors;
```

```
foldername{12} = folderpath4spdors;
```

```
save1spdors = [bugabb,num2str(bugnumber),'span_load1dors.mat'];
```

```
save2spdors = [bugabb,num2str(bugnumber),'span_load2dors.mat'];
```

```
save3spdors = [bugabb,num2str(bugnumber),'span_load3dors.mat'];
```

```
save4spdors = [bugabb,num2str(bugnumber),'span_load4dors.mat'];
```

```
savename{9} = save1spdors;
```

```

savename{ 10} = save2spdors;
savename{ 11} = save3spdors;
savename{ 12} = save4spdors;

%*****fourth set: span ventral*****
fixspvent = 'fixed';
params{ 13} = [130 65 1 65 34.6673 29.5593 0.00030489 1725 1720 4 1743 1757];
params{ 14} = [130 65 1 65 34.6673 29.5593 0.00072776 1725 1713 4 1743 1757];
params{ 15} = [130 65 1 65 34.6673 29.5593 0.00148786 1725 1707 4 1743 1757];
params{ 16} = [130 65 1 65 34.6673 29.5593 0.00261126 1725 1699 4 1743 1757];

ventspanplace =
[computer,':Stacey:wing/laser2000:',bug,num2str(bugnumber),':span:cut_images'];
imagelocation{ 13} = ventspanplace;
imagelocation{ 14} = ventspanplace;
imagelocation{ 15} = ventspanplace;
imagelocation{ 16} = ventspanplace;

imageload1spvent = [bugabb,num2str(bugnumber),'span_load1vent',fixspvent,'.jpg'];
imageload2spvent = [bugabb,num2str(bugnumber),'span_load2vent',fixspvent,'.jpg'];
imageload3spvent = [bugabb,num2str(bugnumber),'span_load3vent',fixspvent,'.jpg'];
imageload4spvent = [bugabb,num2str(bugnumber),'span_load4vent',fixspvent,'.jpg'];
imagezero1spvent = [bugabb,num2str(bugnumber),'span_zero1vent',fixspvent,'.jpg'];
imagezero2spvent = [bugabb,num2str(bugnumber),'span_zero2vent',fixspvent,'.jpg'];
imagezero3spvent = [bugabb,num2str(bugnumber),'span_zero3vent',fixspvent,'.jpg'];
imagezero4spvent = [bugabb,num2str(bugnumber),'span_zero4vent',fixspvent,'.jpg'];
names{ 13,1} = imageload1spvent;
names{ 13,2} = imagezero1spvent;
names{ 14,1} = imageload2spvent;
names{ 14,2} = imagezero2spvent;
names{ 15,1} = imageload3spvent;
names{ 15,2} = imagezero3spvent;
names{ 16,1} = imageload4spvent;
names{ 16,2} = imagezero4spvent;

folderpath1spvent =
[computer,':Stacey:wing/laser2000:',bug,num2str(bugnumber),':span:load1vent'];
folderpath2spvent =
[computer,':Stacey:wing/laser2000:',bug,num2str(bugnumber),':span:load2vent'];
folderpath3spvent =
[computer,':Stacey:wing/laser2000:',bug,num2str(bugnumber),':span:load3vent'];
folderpath4spvent =
[computer,':Stacey:wing/laser2000:',bug,num2str(bugnumber),':span:load4vent'];
foldername{ 13} = folderpath1spvent;

```

```

foldername{ 14} = folderpath2spvent;
foldername{ 15} = folderpath3spvent;
foldername{ 16} = folderpath4spvent;

```

```

save1spvent = [bugabb,num2str(bugnumber),'span_load1vent.mat'];
save2spvent = [bugabb,num2str(bugnumber),'span_load2vent.mat'];
save3spvent = [bugabb,num2str(bugnumber),'span_load3vent.mat'];
save4spvent = [bugabb,num2str(bugnumber),'span_load4vent.mat'];
savename{ 13} = save1spvent;
savename{ 14} = save2spvent;
savename{ 15} = save3spvent;
savename{ 16} = save4spvent;

```

```

%celldisp(names)

```

```

%*****

```

```

i = istart;

```

```

for i = istart:istop

```

```

    imageplace = imagelocation{i};
    folderplace = foldername{i};
    image_name = names{i,1};
    calib_name = names{i,2};
    savefilename = savename{i};
    column_start = params{i}(1);
    start_row = params{i}(2);
    all_lines = params{i}(3);
    line_pixel_width = params{i}(4);
    mic_per_Z = params{i}(5);
    mic_per_XY = params{i}(6);
    force = params{i}(7);
    pin_calib = params{i}(8);
    pin = params{i}(9);
    wingbasex = params{i}(10);
    pinapp = params{i}(11);
    endwing = params{i}(12);

```

```

%***following code by A.C. Trimble*****

```

```

    %READ THE IMAGES
    cd(imageplace);
    image = imread(image_name,'jpg');
    calib = imread(calib_name,'jpg');

```

```

    home = [computer,':Stacey:wing/laser2000:bending_code'];
    cd(home);

```



```

%DISPLAY THE IMAGE
colormap(gray);
imagesc(image)

%GET ONE COMPONENT OF THE IMAGES
oneband = image(:,:,1);
calib_oneband = calib(:,:,1);

%WE NEED PLACES TO STORE SOME STUFF

global line_xsection;
global yin;
global initguess;
global COLM;

line_xsection = ones(line_pixel_width,2,(pin - column_start + 2));
lines = zeros((pin - column_start), 2, all_lines);

calib_lines = zeros((pin - column_start), 2, all_lines);

%*****FOR LOADED IMAGE*****

%START LINE DETECTION AT LINE #1 (=incr)
%LOOP FOR ALL LINES
incr = 1;
while incr <= all_lines;
    column = column_start;
    COLM=3;
    meanCOLM = mean(line_xsection(:,1,COLM));
    meanCOLM2 = meanCOLM;
%jump forward to the correct row to begin searching at the beginning of each line (incr)
    if incr == 1;
        row = start_row;
    else;
        row = round(lines(1, 2, (incr - 1)) + (0.45 * line_pixel_width));
    end;
    % set the initial guess for the fmins to be near the right place
    initguess = [(row + (0.5 * line_pixel_width)) 1 2];
    while column <= pin;
        patch = 0;
        while patch < line_pixel_width;
            line_xsection((patch+1),1,COLM) = oneband((row + patch), column);
            line_xsection((patch+1),2,COLM) = (row + patch);
            patch = patch + 1;

```

```

end;

%COMPUTE THE PEAK OF THIS PATCH
%CALCULATE A GAUSSIAN LEAST_SQUARES FIT TO THE PIXEL
INTENSITIES
[final_Mu, nextguess] = gausstest(line_xsection, initguess,
COLM);
local_peak_row = final_Mu;
initguess = nextguess;

%check for nonsensical return from fmins...
%and check again... for a peak pos. outside the sample range.
%if (local_peak_row - row) < 0; it really shouldn't be outside the sample...
    if (local_peak_row < row);
%it really shouldn't below the sample...
        lines(((column+1)- column_start), 1, incr) = 0;
        lines(((column+1)- column_start), 2, incr) = 0;
        column = column + 1;
        COLM = COLM + 1;
        break;
    end;
    if (local_peak_row - row) > line_pixel_width;
%it really shouldn't be outside the sample...
        lines(((column+1)- column_start), 1, incr) = 0;
        lines(((column+1)- column_start), 2, incr) = 0;
        column = column + 1;
        COLM = COLM + 1;
        break;
    end;
%end;

%WRITE LOCAL LINE POSITION
% as (column, row, line) where column and line are integers and row is the "height"
    lines(((column+1)- column_start), 1, incr) = (column);
    lines(((column+1)- column_start), 2, incr) = (local_peak_row);
%RE-ESTIMATE THE LOCATION OF THE PATCH SEARCH BASED ON THE
CURRENT PEAK LOCATION
    row = round(local_peak_row - (0.5 * line_pixel_width));
    if COLM >= 7;
        meanCOLM = mean(line_xsection(:,1,COLM));
        meanCOLM2 = mean(line_xsection(:,1,COLM-4));
    end;
    column = column + 1
    i

```

```

        COLM = COLM + 1;
    end;

    %SETUP FOR NEXT LINE
    incr = incr + 1;
    hold on;
    %TEST HERE FOR NON_ZERO DATA TO PLOT
    nonzeroX = find(lines(:,1,(incr - 1)) > 0);
    plot(lines(nonzeroX,1,(incr - 1)), lines(nonzeroX,2,(incr - 1)), 'r')
    drawnow;
end;

%***** END OF LOADED IMAGE MEASURE *****
%
%*****
%
%*****START CALIBRATION IMAGE (UNLOADED)
MEASURE*****
line_xsection(:,,:) = 1;
%START LINE DETECTION AT LINE #1 (=incr)
%LOOP FOR ALL LINES
incr = 1;
while incr <= all_lines;
    column = column_start;
    COLM=3;
    meanCOLM = mean(line_xsection(:,1,COLM));
    meanCOLM2 = meanCOLM;
    %jump forward to the correct row to begin searching at the beginning of each line (incr)
    if incr == 1;
        row = start_row;
    else;
        row = round(calib_lines(1, 2, (incr - 1)) + (0.45 *
line_pixel_width));
    end;
    % set the initial guess for the fmins to be near the right place
    initguess = [(row + (0.5 * line_pixel_width)) 1 2];
    while column <= pin_calib;
        patch = 0;
        while patch < line_pixel_width;
            line_xsection((patch+1),1,COLM) = calib_oneband((row + patch),
column);
            line_xsection((patch+1),2,COLM) = (row + patch);
            patch = patch + 1;
        end;
    end;
end;

```

```

                %COMPUTE THE PEAK OF THIS PATCH
%CALCULATE A GAUSSIAN LEAST_SQUARES FIT TO THE PIXEL
INTENSITIES
                [final_Mu, nextguess] = gausstest(line_xsection, initguess,
COLM);
                local_peak_row = final_Mu;
                initguess = nextguess;

                %check for nonsensical return from fmins...
                %and check again... for a peak pos. outside the sample range.
                if (local_peak_row < row);
%it really shouldn't be outside the sample...
                                calib_lines(((column+1)- column_start), 1, incr) =
0;
                                calib_lines(((column+1)- column_start), 2, incr) =
0;
                                column = column + 1;
                                COLM = COLM + 1;
                                break;
                end;
                if (local_peak_row - row) > line_pixel_width;
%it really shouldn't be outside the sample...
                                calib_lines(((column+1)- column_start), 1, incr) =
0;
                                calib_lines(((column+1)- column_start), 2, incr) =
0;
                                column = column + 1;
                                COLM = COLM + 1;
                                break;
                end;
                %end;

                %WRITE LOCAL LINE POSITION
                % as (column, row, line) where column and line are integers and row is the "height"
                calib_lines(((column+1)- column_start), 1, incr) = (column);
                calib_lines(((column+1)- column_start), 2, incr) = (local_peak_row);
%RE-ESTIMATE THE LOCATION OF THE PATCH SEARCH BASED ON THE
CURRENT PEAK LOCATION
                row = round(local_peak_row - (0.5 * line_pixel_width));
                if COLM >= 7;
                        meanCOLM = mean(line_xsection(:,1,COLM));
                        meanCOLM2 = mean(line_xsection(:,1,COLM-4));
                end;

```

```

        column = column + 1
            i
            COLM = COLM + 1;
        end;

        %NEXT LINE
        incr = incr + 1;
        hold on;
        %TEST HERE FOR NON_ZERO DATA TO PLOT
        calib_nonzero = find(calib_lines(:,1,(incr - 1)) > 0);
        plot(calib_lines(calib_nonzero,1,(incr - 1)),
calib_lines(calib_nonzero,2,(incr - 1)), 'c')
        drawnow;
        cd(folderplace)
        print loadimage.tif -f1 -dtiff
    end;

    cd(folderplace)
    save(savefilename, 'lines', 'calib_lines', 'mic_per_Z', 'mic_per_XY', 'force',
'wingbasex', 'pinapp', 'endwing');
    clear lines;
    clear calib_lines;
    clear image;
    clear calib;
    i = i + 1;
end;

```

code to filter raw line data and convert to wing displacement

linestozdiff.m

last modified 11/28/01

%CODE TO FILTER AND FIND EI FROM ONE LASER LINE

%uses calib_lines and lines from findline

clear all;

close all;

bugnumber = 4;

cs = 'chord';

%manducafilt = 0.0005 span/ 0.001 chord

%dragonfilt = 0.001 span/ 0.003 chord

filter = .001;

dv = 'vent';

```

dvabb = 'vt';
loadnumber = 3;
computer = 'Combseyland';
bug = 'manduca';
bugabb = 'mand';

home = [computer,':Stacey:wing/laser2000:bending_code'];
Inpath =
[computer,':Stacey:wing/laser2000:'bug,num2str(bugnumber),':',cs,':load',num2str(loadnu
mber),dv];

cd(Inpath);
loadfilename = [bugabb,num2str(bugnumber),cs,'_load',num2str(loadnumber),dv,'.mat'];
load(loadfilename);

%split calibration and loaded lines into x and y components,
calib_linesx = calib_lines(:,1);
calib_linesy = calib_lines(:,2);
linesx = lines(:,1);
linesy = lines(:,2);
loadpoints = length(linesx)
calibpoints = length(calib_linesx)

%FILTER NOISE OUT OF RAW DATA:
%FilteredSignal=bwfilter(RawSignal,Order,Cutoff,SampleRate)
cd(home);

SampleRate = 1/mic_per_XY;
Order = 2;
Cutoff = filter;
filteredcalib_linesy = bwfilter(calib_linesy, Order, Cutoff, SampleRate);
filteredlinesy = bwfilter(linesy, Order, Cutoff, SampleRate);

%look at raw vs. filtered data
startpoint = 1;
endpoint = length(linesy);
figure
plot(linesx(startpoint:endpoint), linesy(startpoint:endpoint), 'g',
linesx(startpoint:endpoint), filteredlinesy(startpoint:endpoint), 'b',
calib_linesx(startpoint:endpoint), calib_linesy(startpoint:endpoint), 'y',
calib_linesx(startpoint:endpoint),filteredcalib_linesy(startpoint:endpoint), 'b')
title('raw vs. filtered data- 1st filter')
%SPLINE FILTERED LOAD AND CALIBRATION LINES TO EVEN NUMBER OF
POINTS:

```

```

%calculate the number of points to spline
splinepoints = loadpoints;

%define in and out indices of calibration spline (change 1st entry to zero):
inptscalib = length(calib_linesx);
inindexcalib = 1:inptscalib;
outptscalib = splinepoints;
outindexcalib = 1:((inptscalib-1)/(outptscalib-1)):inptscalib;
%create a spline of the y-points of the calibration curve:
calibspline = spline(inindexcalib, filteredcalib_linesy, outindexcalib);

%define in and out indices of loaded spline:
inptload = length(linesx);
inindexload = 1:inptload;
outptload = splinepoints;
outindexload = 1:((inptload-1)/(outptload-1)):inptload;
%create a spline of the y-points of the calibration curve:
loadspline = spline(inindexload, filteredlinesy, outindexload);

%CALIBRATE SO WINGBASE IS AT PIXEL 0:
xcalibpixel = outindexcalib + (calib_linesx(1) - wingbasex) - 1;
ycalibpixel = calibspline;
xloadpixel = outindexload + (linesx(1) - wingbasex) - 1;
yloadpixel = loadspline;
pinx = pinapp - wingbasex;
endx = endwing - wingbasex;
splinepoints = length(xcalibpixel)

%COMPUTE DISPLACEMENTS FROM LINES- in pixels
diff = yloadpixel - ycalibpixel;

%CONVERT Z - DIFFS TO METERS
yload = (diff * mic_per_Z * 0.000001);

%CONVERT CALIBRATION (ZERO) AND LOADED LINE X-POSITION TO METERS
xcalib = (xcalibpixel * mic_per_XY * 0.000001);
xload = (xloadpixel * mic_per_XY * 0.000001);
xpin = (pinx * mic_per_XY * 0.000001);
xend = (endx * mic_per_XY * 0.000001);

startpoint = 1;
endpoint = length(yload);
figure

```

```
plot(xload(startpoint:endpoint), yload(startpoint:endpoint))
%axis([0 0.014 -0.0005 0.0035])
title('z-position difference vs. distance')
```

```
cd(Inpath)
savefilename =
[bugabb,num2str(bugnumber),cs,'_load',num2str(loadnumber),dvabb,'_zdiffs'];
save(savefilename, 'xload', 'xcalib', 'yload', 'xpin', 'xend', 'force');
```

```
*****
```

**code to convert wing displacement to local EI
(assuming exponential EI distribution)**

EIminexp.m

last modified 4/19/02

```
close all;
clear all;
global c
global a
global xcalibc
global xpinc
global forcec
global yloadc
global ypredictedc
```

```
bugnumber = 15;
cs = 'chord';
dv = 'dors';
dvabb = 'drs';
loadnumber = 1;
computer = 'Combseyland';
bug = 'manduca';
bugabb = 'mand';
```

%load the data

```
Inpath =
[computer,':Stacey:wing/laser2000:',bug,num2str(bugnumber),':',cs,':load',num2str(loadn
umber),dv];
cd(Inpath)
loadfilename =
[bugabb,num2str(bugnumber),cs,'_load',num2str(loadnumber),dvabb,'_zdiffs'];
load(loadfilename);
home = [computer,':Stacey:wing/laser2000:bending_code'];
```



```

cd(home)

%convert values if necessary
conversion = 1;
xcalibc = xcalib*conversion;
xpinc = xpin*conversion;
forcec = force*conversion;
yloadc = yload*conversion;

%enter initial guess and error tolerance
initguess = [0.0005 -100];
foptions(1) = 0;
foptions(2) = 1.e-8;
foptions(3) = 1.e-8;
foptions(14) = 10000;
[Pfiddle,out] = fmins('Elcompareexp', initguess, foptions);
Pfiddle

%CALCULATE SOME STUFF
format long e;
ypredicted = ypredictedc/(conversion);
intercept = Pfiddle(1)
exponent = Pfiddle(2)

figure
title ('predicted and actual displacement vs. span/chord')
plot(xcalib, yload, 'k', xcalib, ypredicted, 'r')
h = findobj('type', 'line');
blueline = h(1);
redline = h(2);
set(blueline, 'LineWidth', 3);
set(redline, 'LineWidth', 5);
box('off');
set(gca, 'FontSize', 24);
% folderpath =
[computer,':Stacey:wing/laser2000:',bug,num2str(bugnumber),':',cs,':load',num2str(loadn
umber),dv];
% cd(folderpath)
% print fitimage.tiff -f1 -dtiff

%FIND PROPORTIONAL ERROR IN DISPLACEMENT FIT
n = 1;
prop_error = ones(length(ypredicted), 1);

```

```

while n <= length(ypredicted);
    prop_error(n) = (yload(n) - ypredicted(n))/yload(n);
    n = n + 1;
end;
abs_error = abs(prop_error);
med_error = median(abs_error)
avg_error = sum(abs_error)/length(abs_error)

%output error data
dataname = ['load',num2str(loadnumber),dv,'_errorexp'];
name1 = ['avgerr/mederr/int/exp      '];

dataplace = [computer,':Stacey:wing/laser2000:',bug,num2str(bugnumber),':cs'];
cd(Inpath)
WriteTextFile(dataname, name1, 'w', ' ', '%s\n')
equationdata = [avg_error 0; med_error 0; intercept 0; exponent 0;];
WriteTextFile(dataname, equationdata, 'a', ' ', '%5.10f %5.10f\n')
middle = zeros(length(xcalib),1);
figure
title('proportional error vs. span/chord')
plot(xcalib, prop_error,'b', xcalib, middle, 'k--')
j = findobj('type', 'line');
blackline = j(1);
blueline = j(2);
set(blackline, 'LineWidth', 5);
set(blueline, 'LineWidth', 5);
box('off');
set(gca, 'FontSize', 24);
axis([0 xcalib(length(xcalib)) -1 1])
cd(folderpath)
print errorimage.tif -f2 -dtiff

%FIND EI
n = 1;
Ellocalc = ones(length(xcalibc), 1);
while n <= length(xcalibc);
    Ellocalc(n) = c*(exp(a*xcalibc(n)));
    n = n + 1;
end;
Ellocal = Ellocalc/(conversion^3);
xpoints = [xcalib, xpin, xend];
xtip = [xpin 0; xend 0];

figure

```

```

plot(xcalib, EIlocal, 'r')
axis([0 0.06 -0.0001 0.0004])
h = findobj('type', 'line');
blueline = h(1);
set(blueline, 'LineWidth', 3);
box('off');
set(gca, 'FontSize', 24);

% %SAVE FILE
cd(Inpath)
savefilename =
[bugabb,num2str(bugnumber),cs,'_load',num2str(loadnumber),dvabb,'_expfit'];
save(savefilename, 'intercept', 'exponent', 'EIlocal', 'xpoints', 'yload', 'ypredicted',
'prop_error', 'avg_error', 'med_error', 'xpin', 'xend');

%output EI data
dataname = ['load',num2str(loadnumber),dv,'_data'];
name1 = ['int/exp/avgerr/mederr      '];
name2 = ['xcalib      EI_load',num2str(loadnumber),dv];
errorname = [bugabb,num2str(bugnumber),cs,dv,'_error'];
name3 = ['x(load',num2str(loadnumber),dv,','bugabb,num2str(bugnumber),cs,) yload
ypredicted'];

cd(Inpath)
WriteTextFile(dataname, name1, 'w', '', '%s\n')
equationdata = [intercept 0; exponent 0; avg_error 0; med_error 0];
WriteTextFile(dataname, equationdata, 'a', '', '%5.10f %5.10f\n')

WriteTextFile(dataname, name2, 'a', '', '%s\n')
exportdata = [xcalib EIlocal];
WriteTextFile(dataname, exportdata, 'a', '', '%5.16f %5.16f\n')
WriteTextFile(dataname, xtip, 'a', '', '%5.16f %5.16f\n')

%output displacement error data
WriteTextFile(errorname, name3, 'a', '', '%s\n')
errordata = [xcalib yload ypredicted'];
WriteTextFile(errorname, errordata, 'a', '', '%5.10f %5.10f %5.10f\n')

```

**code to run simplex minimization on actual vs. predicted displacement
(assuming exponential EI distribution)**

EIcompareexp.m
last modified 11/16/00

```
function [C] = EIcompareexp(Pfiddle)
```

```
global c
global a
global xcalibc
global xpinc
global forcec
global yloadc
global ypredictedc
```

```
%FOR AN EXPONENTIAL EI DISTRIBUTION
```

```
c = Pfiddle(1);
a = Pfiddle(2);
ypredictedc = -((2*exp(-(a*xcalibc))*forcec)/(a^3*c)) + ((exp(-
(a*xcalibc))*forcec*xpinc)/(a^2*c)) - (((-2*forcec) + (a*forcec*xpinc))/(a^3*c)) -
((exp(-(a*xcalibc))*forcec.*xcalibc)/(a^2*c)) - (((forcec -
(a*forcec*xpinc))*xcalibc)/(a^2*c));
```

```
%COMPUTE SUM-SQUARED ERROR
```

```
C = sum((yloadc - ypredictedc).^2)
```

```
*****:*****
```

```
code to convert wing displacement to local EI  
(assuming 2nd degree polynomial EI distribution)
```

```
EIminpoly2.m
```

```
last modified 4/19/02
```

```
close all;
clear all;
global a
global b
global c
global xcalibc
global xpinc
global forcec
global yloadc
global ypredictedc
```

```
bugnumber = 15;
cs = 'chord';
dv = 'dors';
dvabb = 'drs';
```

```

loadnumber = 1;
computer = 'Combseyland';
bug = 'manduca';
bugabb = 'mand';

%load the data
Inpath =
[computer,':Stacey:wing/laser2000:',bug,num2str(bugnumber),':',cs,':load',num2str(loadn
umber),dv];
cd(Inpath)
loadfilename =
[bugabb,num2str(bugnumber),cs,'_load',num2str(loadnumber),dvabb,'_zdiffs'];
load(loadfilename);
home = [computer,':Stacey:wing/laser2000:bending_code'];
cd(home)

%convert values if necessary
conversion = 1;
xcalibc = xcalib*conversion;
xpinc = xpin*conversion;
forcec = force*conversion;
yloadc = yload*conversion;

%enter initial guess and error tolerance
initguess = [1 -.01 0.0005];
foptions(1) = 0;
foptions(2) = 1.e-8;
foptions(3) = 1.e-8;
foptions(14) = 10000;
[Pfiddle,out] = fmins('EIcomparepoly2', initguess, foptions);
Pfiddle

%CALCULATE SOME STUFF
format long e;
ypredicted = ypredictedc/(conversion);
const1 = Pfiddle(1)
const2 = Pfiddle(2)
const3 = Pfiddle(3)

%FIND PROPORTIONAL ERROR IN DISPLACEMENT FIT
n = 1;
prop_error = ones(length(ypredicted), 1);
while n <= length(ypredicted);
    prop_error(n) = (yload(n) - ypredicted(n))/yload(n);

```

```

        n = n + 1;
end;
abs_error = abs(prop_error);
med_error = median(abs_error)
avg_error = sum(abs_error)/length(abs_error)

```

```
%FIND EI
```

```

n = 1;
EIlocalc = ones(length(xcalibc), 1);
while n <= length(xcalibc);
    EIlocalc(n) = (a*(xcalibc(n)^2)) + (b*xcalibc(n)) + c;
    n = n + 1;
end;
EIlocal = EIlocalc/(conversion^3);
xpoints = [xcalib, xpin, xend];
xtip = [xpin 0; xend 0];

```

```
*****
```

**code to run simplex minimization on actual vs. predicted displacement
(assuming 2nd degree polynomial EI distribution)**

Elcomparepoly2.m

last modified 4/18/02

```
function [C] = Elcomparepoly2(Pfiddle)
```

```

global a
global b
global c
global xcalibc
global xpinc
global forcec
global yloadc
global ypredictedc

```

```
%FOR A 2ND DEGREE POLYNOMIAL EI DISTRIBUTION
```

```

a = Pfiddle(1);
b = Pfiddle(2);
c = Pfiddle(3);
ypredictedc = (1/(2*a^2*(sqrt(-b^2+(4*a*c)))))*(forcec*((
2*(b^2+(a*b*(xpinc+xcalibc)))+(2*a*(-c+(a*xpinc*xcalibc))))*atan(b/(sqrt(-
b^2+(4*a*c)))) + (2*(b^2+(a*b*(xpinc+xcalibc)))+(2*a*(
c+(a*xpinc*xcalibc)))).*atan((b+(2*a*xcalibc))/(sqrt(-b^2+(4*a*c)))) + (sqrt(-

```

```
b^2+(4*a*c))*((2*a*xcalibc)+(b+(a*(xpinc+xcalibc))*log(c))-
((b+(a*(xpinc+xcalibc))).*log(c+(xcalibc.*(b+(a*xcalibc))))))));
```

```
%COMPUTE SUM-SQUARED ERROR
```

```
C = sum((yloadc - ypredictedc).^2)
```

```
*****
```

```
code to convert wing displacement to local EI  
(assuming linear EI distribution)
```

```
Elminlinear.m
```

```
last modified 4/19/02
```

```
clear all;  
global b  
global m  
global xcalibconv  
global xpincconv  
global forceconv  
global yloadconv  
global ypredictedconv
```

```
bugnumber = 15;  
cs = 'chord';  
dv = 'dors';  
dvabb = 'drs';  
loadnumber = 1;  
computer = 'Combseyland';  
bug = 'Manduca';  
bugabb = 'mand';
```

```
%load the data
```

```
Inpath =
```

```
[computer,':Stacey:wing/laser2000:',bug,num2str(bugnumber),':',cs,':load',num2str(loadn  
umber),dv];
```

```
%Inpath = [computer,':Stacey:wing/laser2000:',bug,num2str(bugnumber),':',cs,];
```

```
cd(Inpath)
```

```
loadfilename =
```

```
[bugabb,num2str(bugnumber),cs,'_load',num2str(loadnumber),dvabb,'_zdiffs'];
```

```
load(loadfilename);
```

```
home = [computer,':Stacey:wing/laser2000:bending_code'];
```

```
cd(home)
```

```

%convert values if necessary
conversion = 0.1;
xcalibconv = xcalib*conversion;
xpinconv = xpin*conversion;
forceconv = force*conversion;
yloadconv = yload*conversion;

%enter initial guess and error tolerance
initguess = [ -0.0001    0.001];
foptions(1) = 0;
foptions(2) = 1.e-8;
foptions(3) = 1.e-8;
foptions(14) = 10000;
[Pfiddle,out] = fmins('Elcomparelinear', initguess, foptions);
Pfiddle

%CALCULATE SOME STUFF
format long e;
ypredicted = ypredictedconv/(conversion);
intercept = Pfiddle(1)
slope = Pfiddle(2)

%FIND EI
n = 1;
Ellocalconv = ones(length(xcalibconv), 1);
while n <= length(xcalibconv);
    Ellocalconv(n) = (m*xcalibconv(n)) + b;
    n = n + 1;
end;
Ellocal = Ellocalconv/(conversion^3);

%FIND PROPORTIONAL ERROR IN DISPLACEMENT FIT
n = 1;
prop_error = ones(length(ypredicted), 1);
while n <= length(ypredicted);
    prop_error(n) = (yload(n) - ypredicted(n))/yload(n);
    n = n + 1;
end;
abs_error = abs(prop_error);
med_error = median(abs_error)
avg_error = sum(abs_error)/length(abs_error)

```

```

*****

```


**code to run simplex minimization on actual vs. predicted displacement
(assuming linear EI distribution)**

EIcomparelinear.m

last modified 11/26/00

```
function [C] = EIcomparelinear(Pfiddle)
```

```
global b
global m
global xcalibconv
global xpinconv
global forceconv
global yloadconv
global ypredictedconv
```

```
%FOR A LINEAR EI DISTRIBUTION:
```

```
b = Pfiddle(1);
```

```
m = Pfiddle(2);
```

```
ypredictedconv = -(1/(2*m^3))*(forceconv*(((m*xcalibconv).*((2*b) +
(m*((2*xpinconv) + xcalibconv)))) + (2*(b + (m*xpinconv))*(b +
(m*xcalibconv))*log(b)) - (2*(b + (m*xpinconv))*(b + (m*xcalibconv)).*log(b +
(m*xcalibconv))))));
```

```
%COMPUTE SUM-SQUARED ERROR
```

```
C = sum((yloadconv-abs(ypredictedconv)).^2)
```

```
*****
```

**code to convert wing displacement to local EI
(assuming constant EI distribution)**

EIminconst.m

last modified 4/19/02

```
clear all;
global c
global xcalibconv
global xpinconv
global forceconv
global yloadconv
global ypredictedconv
```

```
bugnumber = 15;
```

```
cs = 'chord';
```

```
dv = 'dors';
```

```

dvabb = 'drs';
loadnumber = 1;
computer = 'Combseyland';
bug = 'Manduca';
bugabb = 'mand';

%load the data
Inpath =
[computer,':Stacey:wing/laser2000:',bug,num2str(bugnumber),':',cs,':load',num2str(loadn
umber),dv];
%Inpath = [computer,':Stacey:wing/laser2000:',bug,num2str(bugnumber),':',cs,];
cd(Inpath)
loadfilename =
[bugabb,num2str(bugnumber),cs,'_load',num2str(loadnumber),dvabb,'_zdiffs'];
load(loadfilename);
home = [computer,':Stacey:wing/laser2000:bending_code'];
cd(home)

%convert values if necessary
conversion = 1;
xcalibconv = xcalib*conversion;
xpinconv = xpin*conversion;
forceconv = force*conversion;
yloadconv = yload*conversion;

%enter initial guess and error tolerance
initguess = [ 0.001];
foptions(1) = 0;
foptions(2) = 1.e-8;
foptions(3) = 1.e-8;
foptions(14) = 10000;
[Pfiddle,out] = fmins('EIcompareconst', initguess, foptions);
Pfiddle

%CALCULATE SOME STUFF
format long e;
ypredicted = ypredictedconv/(conversion);
const = Pfiddle(1)

%FIND EI
n = 1;
EIlocalconv = ones(length(xcalibconv), 1);
while n <= length(xcalibconv);
    EIlocalconv(n) = c;

```

```

        n = n + 1;
end;
EIlocal = EIlocalconv/(conversion^3);

%FIND PROPORTIONAL ERROR IN DISPLACEMENT FIT
n = 1;
prop_error = ones(length(ypredicted), 1);
while n <= length(ypredicted);
    prop_error(n) = (yload(n) - ypredicted(n))/yload(n);
    n = n + 1;
end;
abs_error = abs(prop_error);
med_error = median(abs_error)
avg_error = sum(abs_error)/length(abs_error)

*****

code to run simplex minimization on actual vs. predicted displacement
(assuming constant EI distribution)
EIcompareconst.m
last modified 4/17/02

function [C] = EIcomparelinear(Pfiddle)

global c
global xcalibconv
global xpinconv
global forceconv
global yloadconv
global ypredictedconv

%FOR A CONSTANT EI DISTRIBUTION:
c = Pfiddle(1);
ypredictedconv = ((forceconv*xpinconv*(xcalibconv.^2))/(2*c)) -
((forceconv*(xcalibconv.^3))/(6*c));

%COMPUTE SUM-SQUARED ERROR
C = sum((yloadconv-abs(ypredictedconv)).^2)

```

Appendix 5: Matlab code for Chapter 5

code to spline points and calculate theta difference between lead/trail or lead/tip minus same difference in slow wing

vacboxspline.m

last modified 5/14/02

```

% PROVIDE:  thetalead, timelead, thetat, timet,
%          thetaslowlead, timeslowlead, thetaslowt, timeslowt

clear all;

% LOAD DATA
home = ['Combseyland:Stacey:vacuum_box2001:April2_vacbox'];
cd(home);
load mothd_slowtrail;
load mothd_helvactrail;

% THETALEAD
%define in and out indices of leading edge spline:
wholenumlead = round(timelead(length(timelead)));
outptslead = wholenumlead + 1;
outindexlead = [(1:1:wholenumlead), timelead(length(timelead))];
%create a spline of the y-points of the leading edge curve:
splinelead = spline(timelead, thetalead, outindexlead);

% THETAT
%define in and out indices of trailing edge or tip spline:
wholenumt = round(timet(length(timet)));
outptst = wholenumt + 1;
outindext = [(1:1:wholenumt), timet(length(timet))];
%create a spline of the y-points of the trailing edge or tip curve:
spline = spline(timet, thetat, outindext);

% THETASLOWLEAD
%define in and out indices of slow leading edge spline:
wholenumslowlead = round(timeslowlead(length(timeslowlead)));
outptsslowlead = wholenumslowlead + 1;
outindexslowlead = [(1:1:wholenumslowlead), timeslowlead(length(timeslowlead))];
%create a spline of the y-points of the slow leading edge curve:
splineslowlead = spline(timeslowlead, thetaslowlead, outindexslowlead);

% THETASLOWT
%define in and out indices of slow trailing edge or tip spline:

```

```

wholenumslowt = round(timeslowt(length(timeslowt)));
outptsslowt = wholenumslowt + 1;
outindexslowt = [(1:1:wholenumslowt), timeslowt(length(timeslowt))];
%create a spline of the y-points of the slow trailing edge or tip curve:
splineslowt = spline(timeslowt, thetaslowt, outindexslowt);

% find lowest number of even points to use:
wholepoints = [wholenumlead, wholenumt, wholenumslowlead, wholenumslowt];
wholepointssort = sort(wholepoints);
totalpoints = wholepointssort(1);

% create new vectors with even numbers of points:
thetaleadnew = splinelead(1:totalpoints);
thetatnew = splinet(1:totalpoints);
thetaslowleadnew = splineslowlead(1:totalpoints);
thetaslowtnew = splineslowt(1:totalpoints);

% multiply by -1 for downstroke, 1 for upstroke, duplicate last posneg
deriv = diff(thetaleadnew);
posneg = deriv';
posneg(find(posneg>0)) = 1; posneg(find(posneg<=0)) = -1;
posnegall = [posneg', posneg(length(posneg))];

% subtract trail from lead, then slow from fast
timesteps = 1:1:totalpoints;
flapdiff = (thetaleadnew - thetatnew)';
slowdiff = (thetaslowleadnew - thetaslowtnew)';
thetadiff = flapdiff - slowdiff;
thetadifffinal = (thetadiff.*posnegall)*-1;

timesteps'
thetadifffinal'

% find inflection points:
[max,min] = findpeakindex(thetaleadnew)

plot(timelead, thetalead, 'o', timesteps, thetaleadnew, '*')
plot(timet, thetat, 'o', timesteps, thetatnew, '*')
plot(timeslowlead, thetaslowlead, 'o', timesteps, thetaslowleadnew, '*')
plot(timeslowt, thetaslowt, 'o', timesteps, thetaslowtnew, '*')
plot(timesteps, flapdiff, 'g', timesteps, slowdiff, 'c', timesteps, thetadiff, 'b', timesteps,
thetadifffinal, 'r')

```

VITA

Stacey Anne Combes was born on December 6, 1971 in Dayton, OH. After brief stints in Greenwich, CT and Los Angeles, CA, Stacey along with her mother, two older sisters and older brother settled in Merced, CA. And thus began Stacey's sun-worshipping days—when Merced temperatures soared to 110°F, Stacey could be found alternately baking herself and dunking in the pool, all of which, of course, foreshadowed her painful plummet towards rainy grad school days in Seattle.

Stacey's Merced years were marked by many notable accomplishments. Her musical talents brought her fame and fortune as an easy listening pianist at the Mansion House restaurant, and her skill at clarinet (not to mention flag-twirling) propelled the Merced marching band to new heights. Stacey's interest in biology began in high school and led her to the urban jungle of U.C. Berkeley, where she earned a B.A. in Integrative Biology in 1994.

Stacey's love of animals began early. At the age of 4, she reputedly found an enormous hairy spider in a sandbox and, with pride, ran to show her less-than-enthralled Aunt Mickey. Stacey actually went on to study spiders during her semester abroad in Costa Rica, sitting for hours by the side of a dirt road watching them spin their webs. Stacey also studied jumping tropical tree frogs before moving on to the illustrious *Manduca* gut neurons as a research technician in Portland, OR. After swearing that she had dealt with her last scaly, black-blooded moth, she somehow ended up studying *Manduca* flight for a large chunk of her dissertation research. Ah, the best laid plans...

Stacey's love of the natural world (and her globe-trotting father) infected her with insatiable wanderlust. She has traveled to Costa Rica, Italy, England, France, Germany, Switzerland, Greece, China, Hong Kong, India, Nepal, Kenya, Tanzania, and Egypt—and she plans to travel as much as she can in the future. During her time in graduate school Stacey had the opportunity to do some travel writing, contributing chapters to The Ecotravellers' Wildlife Guides to Brazil and Australia. She has also written numerous stories for *Northwest Science and Technology*, one of which, "An unsticky situation: How geckos climb up walls and why we should care" won her a Distinguished Award from the International Society for Technical Communication.

Stacey's story would not be complete without her introduction to Doug, the Zoology Department's now-infamous computer boy, while at Berkeley in 1992. Together the two have forged many new paths, not the least of which is their somewhat obsessive approach to home ownership: becoming the first couple ever to build a giant retaining wall, one 60-pound brick at a time, during a torrential and muddy Seattle downpour.

Despite the uninspiring weather, Stacey completed her Ph.D. in Zoology at the University of Washington in 2002. Stacey's work on the role of flexible wings in insect flight has awakened her artistic abilities as well as her scientific skill. She plans to pursue a career that incorporates both of these interests, in an attempt to infect the general public with her fascination for the natural world.